UNIVERSITÀ
CAMPUS BIO-MEDICO DI ROMA

Ph.D. THESIS IN SUSTAINABLE
DEVELOPMENT: ENVIRONMENT, FOOD AND HEALTH
XXXVIII CYCLE a.y. 2022-2023

Design and Development of Electronic Sensor Interfaces for Point-of-Care Devices: Bridging Research and Industrial Innovation

Davide Ciarrocchi

Coordinator
Prof. Chiara Fanali

Supervisor
Alessandro Zompanti, Ph.D.
Lazzaro di Biase, M.D., Ph.D.

Abstract

This thesis presents the development of compact and optimized electronic systems for portable electrochemical characterization, biosensing, and electrical stimulation, aiming to advance continuous, non-invasive, and personalized healthcare monitoring. The primary objective is to design and implement low-noise, high-performance electronic interfaces that enable reliable electrochemical sensing, impedance spectroscopy, and electrical stimulation in portable or point-of-care environments. Leveraging advances in mixed-signal circuit design, the research explores energy-efficient architectures for real-time electrochemical signal acquisition and controlled electrical actuation.

The work addresses critical challenges in device-level biosensing technologies, emphasizing long-term operational stability, high measurement accuracy, and robust wireless communication to ensure dependable performance in connected healthcare scenarios. To overcome these challenges, the thesis introduces innovative circuit- and system-level solutions: a miniaturized potentiostat for electrochemical sensing, configurable bio-impedance spectroscopy interfaces, and a programmable electrical stimulator designed for therapeutic and reverse-iontophoretic applications. Special attention is devoted to safety mechanisms, fault protection strategies, portability, and sustained reliability under physiological conditions and resource-constrained environments.

A major contribution of this work lies in the design of compact and modular mixed-signal platforms tailored for diverse bioelectronic modalities, providing the building blocks for future closed-loop healthcare systems. Experimental validation demonstrates accurate signal acquisition, efficient power management, and reliable operation under physiological conditions, establishing a technological foundation for next-generation wearable and point-of-care diagnostic platforms.

Keywords: *wearable device, electrochemical sensing, impedance spectroscopy, electrical stimulation, closed-loop bioelectronics, low-noise circuits, potentiostat analog front-end, reverse iontophoresis, personalized healthcare.*

Contents

List of Figures

List of Tables

List of Publications

Appended Papers

I. **A. Zompanti**, *et al.*, "Design, Realization and Test of a Low-Cost Electrical Impedance Spectroscopy Analyzer for Biological Samples," *2023 9th International Workshop on Advances in Sensors and Interfaces (IWASI)*, IEEE, 2023.

II. **A. Zompanti**, *et al.*, "Improving Electrical Stimulation Effectiveness and Versatility for Non-Invasive Transdermal Monitoring Applications via an Innovative Mixed-Signal Electronic Interface," *Sensors (Basel, Switzerland)*, vol. 24, no. 23, p. 7626, 2024.

III. **D. Ciarrocchi**, *et al.*, "Biochemical Sensors for Personalized Therapy in Parkinson's Disease: Where We Stand," *Journal of Clinical Medicine*, vol. 13, no. 23, p. 7458, 2024.

IV. **S. Grasso**, *et al.*, "Intelligent Electrochemical Sensing: A New Frontier in On-the-Fly Coffee Quality Assessment," *Chemosensors*, vol. 13, no. 1, p. 24, 2025.

V. **D. Ciarrocchi**, *et al.*, "Improving the Performance of Bio-Impedance Spectroscopy via Dynamic Direct Sampling: Design and Test of a Low-Cost Microcontroller-Based Device," *2025 10th International Workshop on Advances in Sensors and Interfaces (IWASI)*, IEEE, 2025.

VI. **R. Olivieri**, *et al.*, "A Novel Current-Mode EMG Interface," *2025 10th International Workshop on Advances in Sensors and Interfaces (IWASI)*, IEEE, 2025.

VII. **D. Ciarrocchi**, *et al.*, "A Novel Polar-Demodulator-Based Electronic Interface for Bioimpedance Spectroscopy with Enhanced Phase Detection and Reduced Dead Zone," *IEEE Transactions on Instrumentation and Measurement*, 2025.

VIII. **D. Ciarrocchi**, *et al.*, "Breaking Through Lag: Enhancing Intradermal Electro-Osmotic Flow and the Future of Delay-Free Continuous Glucose Monitoring," *Frontiers in Bioengineering and Biotechnology*, 2026.

IX. **D. Ciarrocchi**, *et al.*, "AD8302-based polar demodulator interface for impedance spectroscopy oriented to biomedical applications" *Measurement, Elsevier*, 2026.

Summary of Appended Papers

[Paper I] A. Zompanti, *et al.*, "Design, Realization and Test of a Low-Cost Electrical Impedance Spectroscopy Analyzer for Biological Samples," *2023 9th International Workshop on Advances in Sensors and Interfaces (IWASI)*, IEEE, 2023.
Summary: This work presents the design, implementation, and experimental validation of a low-cost electrical impedance spectroscopy analyzer tailored for biological samples. The system demonstrates accurate frequency response characterization across a wide range of biological impedances, offering a compact and affordable solution for biomedical laboratory and field measurements.
Author's Contribution: Contributing to the design and implementation of the low-cost bio-impedance spectroscopy system, developing the firmware and signal acquisition routines.

[Paper II] A. Zompanti, *et al.*, "Improving Electrical Stimulation Effectiveness and Versatility for Non-Invasive Transdermal Monitoring Applications via an Innovative Mixed-Signal Electronic Interface," *Sensors (Basel, Switzerland)*, vol. 24, no. 23, p. 7626, 2024.
Summary: This paper introduces a mixed-signal electronic interface aimed at enhancing the versatility and efficiency of electrical stimulation for non-invasive transdermal monitoring. The system integrates adaptive control and stimulation modules to optimize signal delivery and monitoring performance, enabling improved biomedical sensing and therapeutic applications.
Author's Contribution: Design and implementation of the mixed-signal electronic interface, developing the control and stimulation firmware, supporting the system integration and experimental validation, and participating in data analysis and manuscript preparation.

[Paper III] D. Ciarrocchi, *et al.*, "Biochemical Sensors for Personalized Therapy in Parkinson's Disease: Where We Stand," *Journal of Clinical Medicine*, vol. 13, no. 23, p. 7458, 2024.
Summary: This review discusses the current state of biochemical sensing technologies for personalized Parkinson's disease therapy. It surveys advances in biomarker detection, wearable biosensors, and closed-loop therapeutic systems, outlining the challenges and opportunities for clinical translation.
Author's Contribution: Contributing to the literature review and analysis of biochemi-

cal sensing technologies, supporting the discussion on wearable biosensors and closed-loop therapeutic systems, writing the manuscript and revision.

[Paper IV] S. Grasso, *et al.*, "Intelligent Electrochemical Sensing: A New Frontier in On-the-Fly Coffee Quality Assessment," *Chemosensors*, vol. 13, no. 1, p. 24, 2025.
Summary: This paper presents an intelligent electrochemical sensing platform for real-time coffee quality assessment. Leveraging data-driven algorithms and adaptive signal analysis, the system provides an efficient, on-the-fly evaluation method for food and beverage quality monitoring.
Author's Contribution: Developing the electronic potentiostat device, contributing to the system integration and testing, supporting the experimental validation and manuscript revision.

[Paper V] D. Ciarrocchi, *et al.*, "Improving the Performance of Bio-Impedance Spectroscopy via Dynamic Direct Sampling: Design and Test of a Low-Cost Microcontroller-Based Device," *2025 10th International Workshop on Advances in Sensors and Interfaces (IWASI)*, IEEE, 2025.
Summary: This paper proposes a dynamic direct sampling approach implemented on a low-cost microcontroller platform to enhance the performance of bio-impedance spectroscopy. Experimental validation confirms improved phase accuracy and reduced signal distortion compared to conventional low-cost architectures.
Author's Contribution: Proposing the dynamic direct sampling architecture, designing and implementing the analog/mixed-signal and digital circuits, developing the microcontroller-based acquisition system and signal processing algorithms, performing the experimental validation and data analysis, and contributing to the manuscript preparation.

[Paper VI] R. Olivieri, *et al.*, "A Novel Current-Mode EMG Interface," *2025 10th International Workshop on Advances in Sensors and Interfaces (IWASI)*, IEEE, 2025.
Summary: The paper introduces a current-mode front-end for surface electromyography (sEMG) acquisition, enabling compact and power-efficient biopotential measurement. The proposed architecture demonstrates enhanced noise immunity and scalability for wearable biomedical systems.
Author's Contribution: Design requirements of the current-mode interface, supporting the selection of the circuit architecture and the evaluation of preliminary design solutions; contribution to the discussion of results and to the revision of the manuscript.

[Paper VII] D. Ciarrocchi, *et al.*, "A Novel Polar-Demodulator-Based Electronic Inter-

face for Bioimpedance Spectroscopy with Enhanced Phase Detection and Reduced Dead Zone," *IEEE Transactions on Instrumentation and Measurement*, 2025.
Summary: This article presents an advanced polar demodulator interface for bioimpedance spectroscopy, achieving improved phase resolution and minimizing dead-zone artifacts. The system architecture is validated through simulations and experimental measurements, confirming its potential for precise biomedical impedance monitoring.
Author's Contribution: Proposing, designing and implementing the polar-demodulator-based electronic interface, developing the signal processing and measurement algorithms, performing simulations and experimental validation, and manuscript preparation.

[Paper VIII] D. Ciarrocchi, *et al.*, "Breaking Through Lag: Enhancing Intradermal Electro-Osmotic Flow and the Future of Delay-Free Continuous Glucose Monitoring," *Frontiers in Bioengineering and Biotechnology*, 2026.
Summary: This work investigates methods to overcome response lag in intradermal electro-osmotic flow systems for glucose monitoring. The proposed electronic and electrochemical design improvements pave the way for real-time, delay-free continuous glucose sensing.
Author's Contribution: Leading the conceptualization of the study, designing the electronic and electrochemical subsystems, developing the experimental setup and measurement protocols, performing data analysis and interpretation, and contributing to the manuscript preparation.

[Paper IX] D. Ciarrocchi, *et al.*, "AD8302-based polar demodulator interface for impedance spectroscopy oriented to biomedical applications," *Measurement, Elsevier*, 2026.
Summary: This paper describes the design and testing of a polar demodulator interface based on the AD8302 for bio-impedance spectroscopy. The proposed system offers improved accuracy in phase detection and amplitude measurement, suitable for compact biomedical impedance analyzers.
Author's Contribution: Proposing, designing, and implementing the AD8302-based polar demodulator interface, developing the hardware and firmware, performing all experimental characterizations and data analysis, and writing the manuscript.

Thesis organization

The thesis is organized into five chapters with the following structure:

- Chapter 1 contextualizes this research within the field of portable devices for ther-

apy closed-loop, focusing on the development of compact devices and optimized electronic interfaces for electrochemical sensing and reverse iontophoresis applications. It reviews the background on wearable biomedical systems, highlighting needs and current challenges in circuit efficiency, signal integrity, and device integration. The chapter also outlines the motivation, objectives, and specific contributions of this thesis toward advancing low-power, high-performance electronic platforms for next-generation portable and wearable devices.

- Chapter 2 provides an overview of the fundamental principles of electrochemistry and summarizing the main circuit configurations used for potentiostat-based sensor readout. Building on this, a compact, general-purpose device for electrochemical sensor readout was designed, implemented, and experimentally validated. The system features low-noise, low-power operation, is battery-powered, and integrates wireless communication, making it suitable for portable and wearable biomedical applications.

- Chapter 3 provides an overview of bioimpedance (bio-Z) spectroscopy as a valuable technique in clinical practice. Specifically, it introduces the fundamental principles and electrophysiological mechanisms underlying the method, describes the electrodes and measurement setups required for its implementation, and reviews a range of potential solutions for designing bio-Z interface circuits. The chapter also discusses key aspects of circuit architecture in demodulation approaches, highlighting their main limitations and detailing how each approach was optimized in order to expand the range and precision.

- Chapter 4 introduces the principles of electrical stimulation, detailing the stimulation methods, summarizing the key design requirements, and providing an overview of the proposed fully integrated system for portable and wearable applications. Within this system, a $\pm$120 V single-channel configurable stimulator and an overcurrent detection circuit for ensuring safe stimulation are presented.

- Chapter 5 concludes the thesis and suggests future research directions on several topics covered in this work.

Chapter 1

Introduction

The development of wearable biosensors has emerged as a transformative approach for personalized, continuous, and non-invasive healthcare monitoring. These platforms integrate advanced electronic systems with biochemical interfaces to enable real-time acquisition, processing, and wireless transmission of physiological signals, offering a convenient alternative to conventional, often painful, blood analyses by enabling continuous monitoring of biomarkers in biofluids such as sweat, saliva, tears, urine, and interstitial fluid (ISF) [1]. Wearable platforms have been engineered in diverse forms depending on the target biofluid and application. Epidermal sensors, such as skin patches, gloves, and conformal skin-worn devices, provide comfortable and continuous monitoring of sweat and ISF biomarkers [2, 3]. Microneedles and reverse iontophoresis systems allow minimally invasive access to ISF, facilitating continuous analyte sampling for metabolites, electrolytes, and glucose [4]. Wearable electrochemical devices integrated into smartwatches or wristbands enable real-time monitoring of metabolites and nutrients in sweat and ISF [5, 6]. Ocular platforms, including smart contact lenses, eyeglasses, and spring-like sensors, enable detection of biomarkers in tears, while saliva-based wearables such as mouthguards or pacifiers allow non-invasive continuous monitoring [7, 8]. At the core of these systems lies the electronic architecture, which is responsible for accurate signal transduction, amplification, processing, and wireless communication. The architecture of these devices generally includes: (i) a flexible or conformal substrate that maintains intimate contact with the body; (ii) electrochemical electrodes; (iii) immobilized bio-receptors or recognition elements for selective analyte detection; (iv) amplification and signal processing circuits; (v) electrochemical analyzers; (vi) wireless communication modules; and (vii) data acquisition and display software [6]. These electronic subsystems are not merely supportive components—they define the device's performance in terms of sensitivity, stability, and energy efficiency, ultimately determining its viability for long-term, portable operation. Through this integration, electrochemical signals generated by analyte–receptor interactions are converted into electrical signals that can be measured, processed, and transmitted in real-time. To achieve reliable sensing, wearable devices rely on advanced

materials and structural engineering. Hydrogels, for instance, serve as stretchable substrates that conform to the skin while enabling analyte collection and immobilization of sensing elements [9, 10]. The incorporation of nanomaterials enhances sensor sensitivity, detection limits, and mechanical robustness, enabling ultra-sensitive monitoring of metabolites, glucose, and other biomarkers [11, 12]. Furthermore, microfluidic channels are often integrated into wearable platforms to facilitate controlled collection and transport of biofluids for continuous analysis [13]. The convergence of electrochemical sensing with electrical stimulation technologies, such as reverse iontophoresis and drug delivery modules, has enabled the development of closed-loop wearable systems. These platforms can extract analytes from ISF or sweat for real-time monitoring while simultaneously delivering therapeutic agents in a feedback-regulated manner. Such devices are particularly relevant for chronic disease management—for example, closed-loop insulin delivery in diabetes or real-time levodopa administration in Parkinson's disease—where continuous biochemical feedback guides therapeutic dosing and lifestyle interventions. Despite these advances, challenges remain in sensor stability, selectivity, energy efficiency, and mechanical integration. Flexible, miniaturized, and energy-efficient electronics, combined with robust and biocompatible materials, are critical to achieving reliable, long-term performance in real-world settings. Addressing these challenges is essential to advance wearable electrochemical biosensors from research prototypes to practical, medical-grade platforms, ultimately enabling continuous, real-time, and personalized healthcare monitoring.

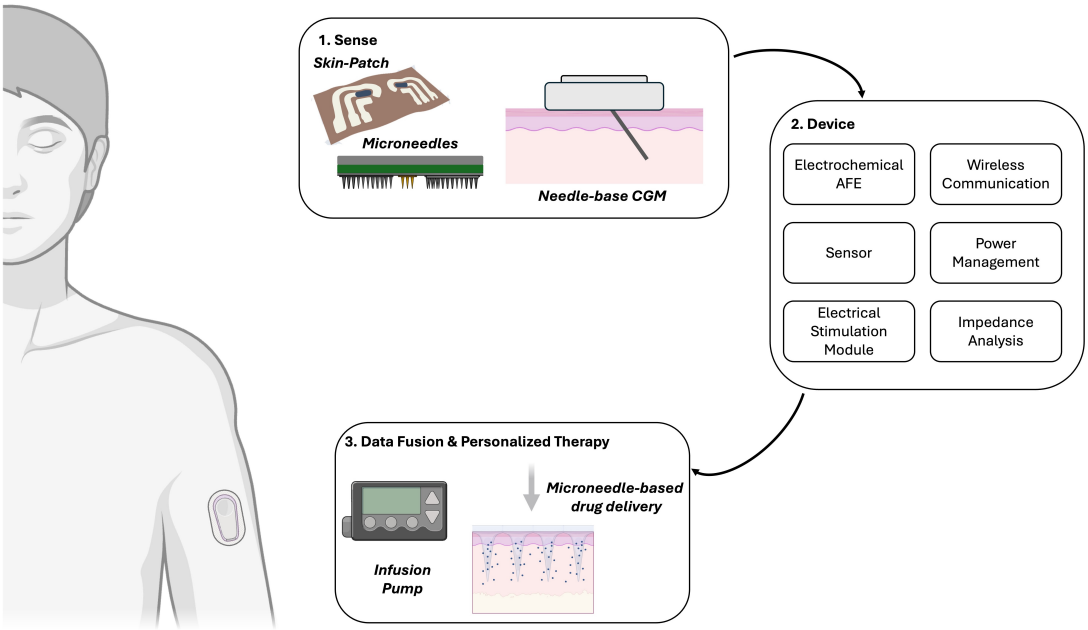

Figure 1.1: Block scheme of a tailored system.

1.1 Motivation

The growing demand for personalized, continuous, and non-invasive healthcare monitoring has driven significant interest in electrochemical sensing technologies. These systems enable the detection of biochemical markers from biofluids such as sweat, saliva, or interstitial fluid, providing real-time insight into metabolic activity, electrolyte balance, and physiological stress. Digitalizing chemical information into electrical signals, electrochemical analysis offers a powerful route toward continuous metabolic monitoring in wearable and portable devices, as well as in point-of-care (POC) platforms that allow rapid, on-site diagnostic assessment. The ability to acquire real-time biochemical signals is particularly critical for the management of chronic diseases, where timely feedback can guide therapeutic interventions and prevent adverse events. Notably, this approach is particularly relevant for diabetes management, where continuous glucose monitoring can enable closed-loop insulin delivery, and for Parkinson's disease, where real-time monitoring of levodopa levels in the bloodstream can guide closed-loop, personalized levodopa administration. However, despite extensive progress, several challenges still hinder the reliable and long-term implementation of electrochemical sensors in real-world applications. The stability and reproducibility of electrochemical interfaces are often limited by factors such as biofouling, drift, and environmental variability, which affect sensor calibration and long-term accuracy. Moreover, achieving high sensitivity and selectivity in complex biofluids requires careful electrode surface engineering, optimized transduction mechanisms, and—critically—the integration of high resolution, low-noise, and energy-efficient electronic front-ends. These electronic subsystems are the backbone of wearable and POC platforms, as they govern signal fidelity, power consumption, and wireless connectivity, ultimately determining the feasibility of continuous monitoring in resource-constrained environments. These considerations are equally critical for Point-of-Care (POC) devices, which demand rapid, robust, and user-friendly operation in diverse clinical or home settings. Within the realm of electrochemical analysis, impedance spectroscopy has emerged as a complementary technique for characterizing electrode–analyte interfaces and monitoring physiological states. By applying a small alternating current (AC) signal across a range of frequencies and measuring the resulting voltage response, impedance spectroscopy provides insight into interfacial properties, charge transfer dynamics, and the composition of biofluids or tissues. It is also widely employed as the primary measurement method for impedimetric sensors, which detect changes in impedance caused by biomolecular interactions at the electrode surface. This approach is particularly useful for detecting subtle variations that may not be captured by conventional electrochemical measurements alone. However, practical implementation in wearable and POC devices is challenged by the requirement for high-frequency measurements, which increase energy consumption and necessitate precise instrumentation to maintain accuracy across wide fre-

quency ranges. Addressing these challenges is essential to move electrochemical sensing beyond laboratory settings toward practical, medical-grade wearable and POC platforms. The continued development of robust, miniaturized, and energy-efficient electronic interfaces will enable real-time monitoring of disease-relevant biomarkers, opening the door to closed-loop bioelectronic systems. In such systems, continuous biochemical feedback can directly inform therapeutic dosing, lifestyle adjustments, or other personalized interventions, providing a proactive and dynamic approach to disease management, as shown in Fig. 1.1. To date, several devices for electrochemical sensing, electrical stimulation, and impedance spectroscopy are commercially available and reported in the literature. However, these solutions are often black boxes, bulky, and expensive, which limits their accessibility and practical use in continuous, wearable healthcare applications. Therefore, there is a critical need for design exploration across these three areas, aimed at developing efficient yet simple architectures with built-in fault protection and safety features. Such an approach would enable the integration of these subsystems, simplifying communication and synchronization while mitigating the challenges associated with combining separate, bulky systems for each technique. The potential advantages of integrating electrochemical sensing, electrical stimulation, and impedance spectroscopy in a compact, portable platform are substantial, offering new opportunities for both academic research and industrial applications. In particular, the development of bi-directional interfaces that combine sensing with drug delivery is highly promising, as it forms the foundation for closed-loop systems. These systems have the potential to overcome the limitations of current electrochemical devices for disease monitoring by dynamically controlling therapeutic delivery in response to real-time biomarker feedback, enabling truly personalized and automated healthcare interventions.

1.2 Research Objectives

The primary aim of this thesis is to advance the development of integrated systems for electrochemical sensing and electrical stimulation that combine clinical relevance with industrial applicability. The research focuses on designing mixed-signal system architectures, circuit techniques, and interface solutions for bio-impedance spectroscopy (bio-Z), electrochemical sensing, and electrical stimulation, capable of operating efficiently and reliably in portable and wearable applications. A central goal is to increase the technology readiness level (TRL) of these systems, moving them from laboratory prototypes toward robust, industrially deployable platforms. To accomplish this, the following specific objectives were defined:

- **Objective 1**: Examine the challenges and potential solutions in designing low-noise potentiostat circuits for wearable and portable electrochemical sensors. The focus

is on developing compact, low-power, and low-noise architectures capable of providing high resolution and reliable measurements for continuous real-time monitoring applications.

- **Objective 2**: Explore the challenges and opportunities of implementing the bio-Z spectroscopy electronic interfaces for wearable and portable devices. In particular, the objective is to explore, propose, and implement highly accurate, high resolution, and power-efficient architectures and required circuits.

- **Objective 3**: Investigate the design challenges and opportunities in developing electrical stimulation systems for wearable and portable biomedical applications. The goal is to propose and implement stimulation architectures and control circuits that ensure safe, accurate, and energy-efficient operation, while supporting advanced functionalities such as current-controlled delivery for applications like reverse iontophoresis.

1.3 Research Contribution

The contributions addressing the research objectives are listed as follows:

- **Contribution 1 [Paper IV]:** This work presents the design and implementation of a compact, low-noise, and low-power potentiostat for portable electrochemical sensing applications. The proposed mixed-signal interface enables accurate current and voltage measurements over a wide dynamic range, while minimizing power consumption and circuit complexity. The architecture integrates programmable gain control and optimized transimpedance amplification to achieve high sensitivity and stability in the presence of electrode and biofluid variability. Emphasis is placed on noise optimization, leakage reduction, and fault protection to ensure reliable operation in wearable and point-of-care environments. Experimental validation demonstrates excellent agreement with commercial benchtop instruments, confirming the potentiostat's capability for accurate and energy-efficient electrochemical characterization in resource-constrained and continuous monitoring scenarios.

- **Contribution 2 [Paper V, VII, IX]:** This work presents three optimized approaches to enhance the performance, accuracy, and usability of bioimpedance spectroscopy (BIS) systems. First, a dynamic direct sampling method was developed and implemented on a low-cost microcontroller platform, improving phase accuracy and reducing signal distortion compared to conventional architectures. Second, a polar demodulator interface based on the AD8302 was designed, providing higher precision in both phase detection and amplitude measurement, while maintaining a compact form factor suitable for portable biomedical analyzers. Third, an advanced

polar-demodulator-based electronic interface was proposed to enhance phase resolution and minimize dead-zone artifacts, which are common limitations in traditional polar architectures. All approaches were validated through simulations and experimental measurements, demonstrating consistent improvements in accuracy, stability, and scalability, and providing a solid foundation for low-cost, high-precision BIS platforms suitable for wearable and point-of-care biomedical applications.

- **Contribution 3 [Paper II, VIII]:** This work presents a mixed-signal electronic interface designed to enhance the versatility and efficiency of electrical stimulation for non-invasive transdermal monitoring. The proposed system integrates adaptive control and stimulation modules to optimize signal delivery and improve measurement accuracy. A particular focus is placed on overcoming response lag in intradermal electro-osmotic flow systems used for glucose monitoring. Through innovative electronic and electrochemical design strategies, the system enables real-time, delay-free continuous glucose sensing. The proposed architecture supports current-controlled stimulation, ensuring safe operation and high resolution delivery of iontophoretic currents. This contribution demonstrates the potential of the developed interface to enable future wearable and continuous health-monitoring platforms.

The presented research advances the design and validation of electrochemical, bioimpedance-based measurement and stimulation systems through integrated modeling, simulation, and experimental approaches. The developed methodologies and electronic interfaces enhance measurement accuracy, system efficiency, and applicability to portable and point-of-care devices. Experimental validations confirm the feasibility of the proposed solutions, reaching an estimated Technology Readiness Level (TRL) of 4, and establishing a solid foundation for future translation into real-world biomedical applications.

Chapter 2

Empowering Electrochemistry: The Design of a Portable Potentiostat

2.1 Electrochemistry Fundamentals

Electrochemical cells are defined most generally as two electrodes separated by at least one electrolyte phase. In the electrochemical experiments, many factors affect the transport of the charge across the interface between the chemical phases, like an electric conductor (electrode) and an ionic conductor solution (electrolyte). At the electrode/electrolyte interface, the applied potential will generate a current flow: the movement of both electrons and holes transports the charge. Since the reference electrode has a fixed potential, any changes in the cell are ascribable to the working electrode. So the potential of the working electrode is controlled with respect to the potential of the reference electrode, and through its potential is possible to control the energy of the electrons. Driving the potential of the electrode to a more negative value, the energy of the electrons is raised: if the energy level is high enough the electrons can transfer into vacant electronic states on species in the electrolyte. In that case, a flow of electrons from electrode to solution (a reduction current) occurs (Figure 2.1(a)). Similarly, imposing a more positive potential the energy of the electrons can be lowered: at some point electrons on solutes in the electrolyte will find a lower energy state on the electrode and will transfer there. Their flow, from solution to electrode, is an oxidation current (Figure 2.1(b)). The critical potentials at which these processes occur are related to the standard potentials, E^o, for the specific chemical substances in the system.

In a typical electrochemical experiment, the working and the reference electrodes are immersed in the solution and the potential difference between the two electrodes is varied by an external power supply. The variation of the potential, E, can produce redox reactions and thus a current, because electrons cross the electrode/solution interface.

The number of electrons that cross the interface is related to the extent of the chem-

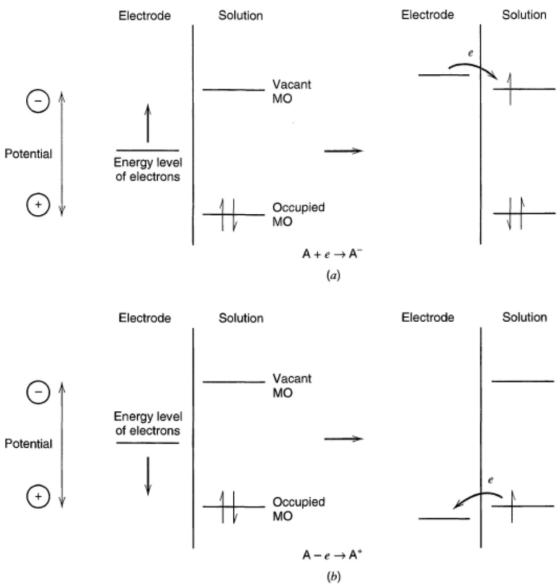

Figure 2.1: Representation of reduction (a) and oxidation (b) process of a species.

ical reaction: the current is related to the amounts of reactants consumed and products generated.

Faraday's law gives the relationship between the charge passed and the amount of product generated:

$$m = \frac{Q\,M}{F\,z} \tag{2.1}$$

where:

- m is the mass of generated substance at an electrode [g],
- Q is the total electric charge passed through the solution [C],
- $F = 96485$ C mol^{-1} is the Faraday constant,
- M is the molar mass of the substance [g/mol],
- z is the valency number of the ions of the substance (number of electrons transferred per ion).

Thus, 96 485.4 C causes 1 equivalent of reaction (e.g., consumption of 1 mole of reactant or production of 1 mole of product in a one-electron reaction).

The current I is the rate of flow of charge (coulombs or electrons), where:

$$I = \frac{dQ}{dt} \tag{2.2}$$

and a current of 1 A corresponds to 1 C/s.

Usually, it is useful to plot the current (I) as a function of the potential (E): these curves can be quite informative about the solution, the electrodes, and the reactions taking place at the solution/electrode interface.

Two types of phenomena can occur at the electrodes:

- Faradaic processes : Charge is transferred across the electrode-solution interface. Charge transfer causes oxidation or reduction processes governed by Faraday's law: the amount of chemical reaction caused by the flow of current is proportional to the amount of electricity passed.

- Non-faradaic processes : Under some conditions, applying a range of potentials to a specific electrode-solution interface, no charge-transfer reactions may occur because they are thermodynamically or kinetically unfavourable. However, other processes such as adsorption and desorption can occur, changing the structure of the electrode-solution interface, and thus the potential or the solution composition. Although charges do not cross the interface, currents can flow when the potential, electrode area, or solution composition change.

Both faradaic and non-faradaic processes occur when electrode reactions take place. The faradaic processes are usually of primary interest, but the effects of the non-faradaic processes must be taken into account when using electrochemical data to obtain information about the charge transfer and associated reactions.

2.1.1 Non-faradaic Processes and the Ideal Polarized Electrode

The ideal polarized electrode (IPE) is an electrode at which no charge transfer across the electrode-solution interface can take place, regardless of the potential applied by an external voltage source (in real cases, only within a limited potential range).

Since charge cannot cross the IPE interface when the potential across it is changed, the behaviour of the electrode-solution interface is analogous to that of a capacitor and is governed by the equation:

$$\frac{q}{E} = C \tag{2.3}$$

Where q is the charge stored in the capacitor [C, coulombs], E is the potential applied on the two metal plates of the capacitor [V, volts] and C is the capacitance [F, farads]. When a potential is applied across the capacitor, a charging current will flow and charges will accumulate on its metal plates until:

$$q = C \cdot E \tag{2.4}$$

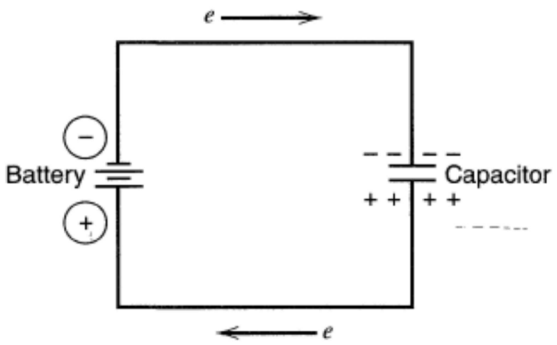

Figure 2.2: Charging a capacitor with a battery.

For example, if a potential difference of 2 V is applied across a 10 μF capacitor, current will flow until 20 μC has accumulated on the capacitor plates. The magnitude of the current depends on the resistance of the circuit.

The electrode-solution interface can be modeled as a capacitor, where one metal plate is the electrode and the other plate is the solution near the electrode: at a given potential, the metal electrode will accumulate a charge q_M and the solution will show a charge q_s, with:

$$q_M = -q_s \tag{2.5}$$

The charge on the metal, q_M, represents an excess or deficiency of electrons and resides in a very thin layer (< 0.1 Å) on the metal surface. The charge in solution, q_s, is made up of an excess of either cations or anions in the vicinity of the electrode surface.

All the charged species and oriented dipoles existing at the electrode-solution interface are called the electrical double layer. At a given potential, the electrode-solution interface is characterized by a double-layer capacitance, C_d, typically in the range of 10 to 40 μF/cm^2.

However, unlike real capacitors, whose capacitances are independent of the voltage across them, C_d is often a function of potential.

The solution-side plate of the capacitor is made up of several layers. The layer closest to the electrode contains solvent molecules and other species (ions or molecules) that are specifically adsorbed on the electrode surface. This inner layer is also called the compact, Helmholtz, or Stern layer.

The electrical center of the Helmholtz layer ions is located on the inner Helmholtz plane (IHP), at a distance x_1 from the electrode-solution interface plane. The total charge density from specifically adsorbed ions in this inner layer is:

$$\sigma_i \quad (\mu\text{C/cm}^2) \tag{2.6}$$

The solvated ions can approach the electrode surface only to a distance x_2. The

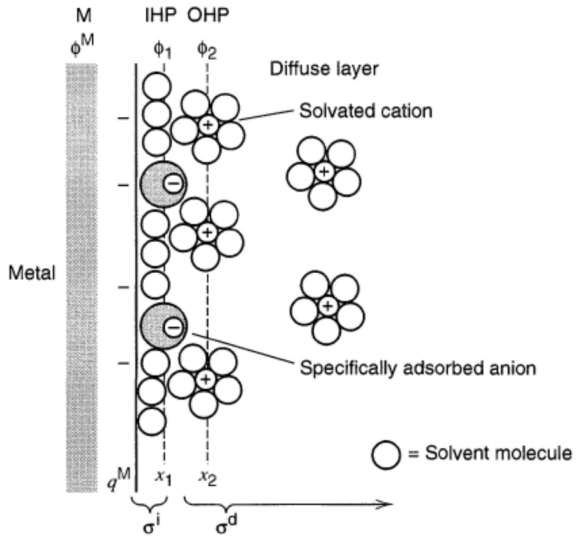

Figure 2.3: Electrical double layer.

electrical center of these ions is called the outer Helmholtz plane (OHP).

So interactions between solvated ions and the charged electrode involve only long-range electrostatic forces and are independent of the chemical properties of the ions that are non-specifically adsorbed.

The non-specifically adsorbed ions are distributed in a large region called the diffuse layer, which extends from the OHP to the bulk of the solution. The charge density in the diffuse layer is σ_d, and the total charge density of the solution side of the electrical double-layer is:

$$\sigma^s = \sigma^i + \sigma^d = -\sigma^M \tag{2.7}$$

The thickness of the diffuse layer depends on the total ionic concentration in the solution.

The profile of the potential across the double-layer region is shown in the following figure (not included here).

The double-layer phenomenon can affect the rates of the reactions that take place on the electrode: if an electro-active species, not specifically adsorbed, is present, it will be able to approach the electrode only to the OHP and it will interact with a potential that is lower than the potential at the electrode-solution interface, because of the potential drop across the diffuse layer.

Under some conditions, when very low concentrations of electro-active species are present in the solution, the charging non-faradaic current can be much larger than the faradaic current produced by the redox reactions. So it is important to understand the behaviour of the charging current for some electrochemical experiments.

Consider a cell consisting of an IPE and an ideal reversible electrode. We can approximate such a system with an electrical circuit with:

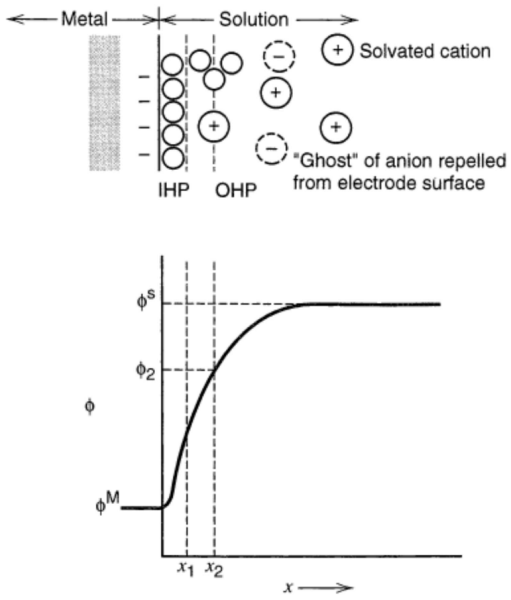

Figure 2.4: Potential profile across the double-layer region.

- a resistor R_s, representing the solution resistance,
- a capacitor C_d, representing the double layer at the electrode-solution interface.

Figure 2.5: Electrical equivalent of an IPE electrode

The capacitance C_d is usually a function of the applied potential, so the model is accurate only if the potential does not change too much. It is possible to obtain useful information about the system by applying a perturbation and observing the system behaviour.

2.1.2 Potential Step Experiment

If we apply a potential step to the IPE, the system will show the typical behaviour of a RC circuit.

The total applied potential E can be expressed as the sum of two contributions:

$$E = E_R + E_C = iR_S + \frac{q}{C_d} \tag{2.8}$$

where:

- E_R is the potential drop across the resistor R_S,

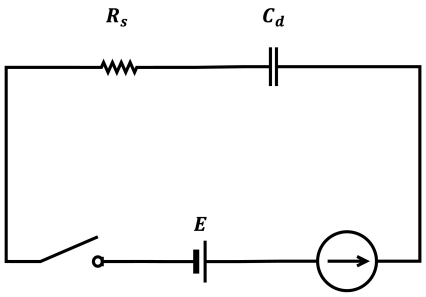

Figure 2.6: Potential step experiment.

- E_C is the potential drop across the capacitor C_d.

$$i = \frac{dq}{dt} = \frac{-q}{R_S C_D} + \frac{E}{R_S} \tag{2.9}$$

assuming that initially the capacitor is fully uncharged ($q = 0$ at $t = 0$), the charge accumulated on the capacitor as a function of time is given by:

$$q(t) = E\, C_d \left[1 - e^{-\frac{t}{R_S C_d}}\right] \tag{2.10}$$

$$i(t) = \frac{E}{R_S}\, e^{-\frac{t}{R_S C_d}} \tag{2.11}$$

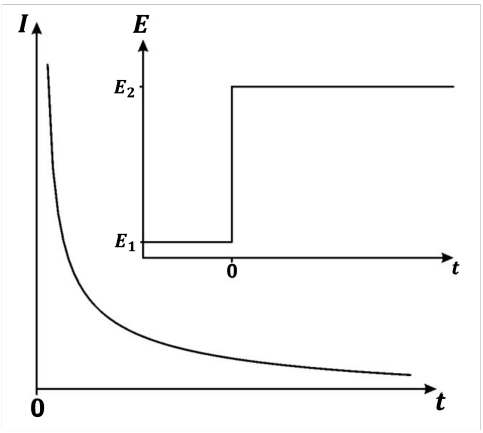

Figure 2.7: Current response for a potential step.

2.1.3 Potential Ramp

A voltage ramp or linear potential sweep is a potential that increases linearly with time starting from an initial value (here assumed to be zero) at a sweep rate v (in $\mathrm{V}s^{-1}$):

$$E = vt \tag{2.12}$$

If such a ramp voltage is applied to the RC circuit, the following equation still applies:

$$E = E_R + E_C = iR_S + \frac{q}{C_d} \tag{2.13}$$

$$vt = R_S \frac{dq}{dt} + \frac{q}{C_d} \tag{2.14}$$

Assuming $q = 0$ at $t = 0$, the current $i(t)$ can be expressed as:

$$i(t) = vC_d \left[1 - e^{-\frac{t}{R_S C_d}}\right] \tag{2.15}$$

If a triangular wave is applied, the following results is obtained as shown in Fig. 2.8 b).

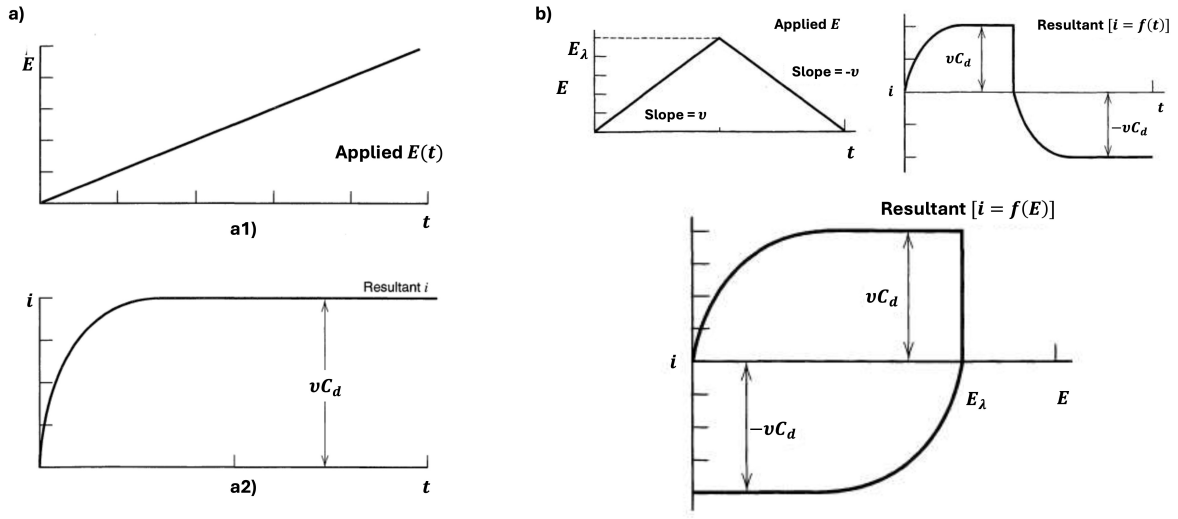

Figure 2.8: a) Current response for a potential step. b) Current response for a cyclic linear potential sweep input.

2.1.4 Faraidic Processes

Electrochemical cells producing faradaic currents are classified as galvanic (Fig. 2.9 a)) or electrolytic cells (Fig. 2.9 b)):

- **Galvanic cell:** reactions occur spontaneously at the electrodes when a conductor connects them. This kind of cell is used to convert chemical energy into electrical energy.
- **Electrolytic cell:** reactions occur because of the application of an external voltage greater than the open-circuit potential of the cell. These cells are used to carry out specific chemical reactions by supplying external electrical energy.

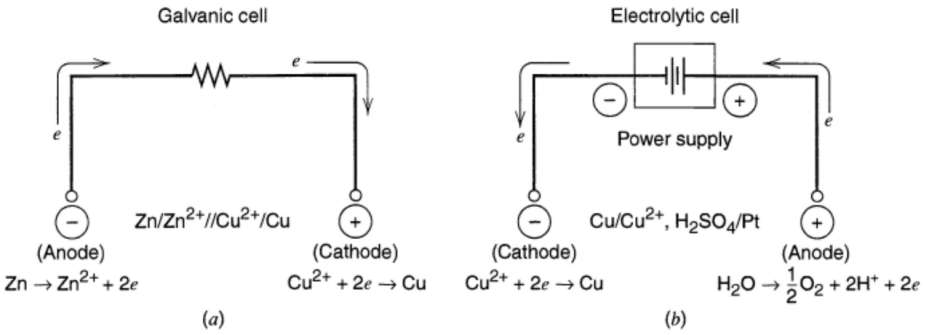

Figure 2.9: a) Galvanic cell b) Electrolytic cell

In discussing cells, the electrode at which reductions occur is called *cathode*, and the electrode at which oxidations occur is called *anode*. A current in which electrons cross the interface from the electrode to a species in solution is a cathodic current, while electron flow from a solution species into the electrode is an anodic current. In an electrolytic cell, the cathode is negative with respect to the anode; but in galvanic cell, the cathode is positive with respect to the anode. The important parameters in an electrochemical cell are shown in the following figure:

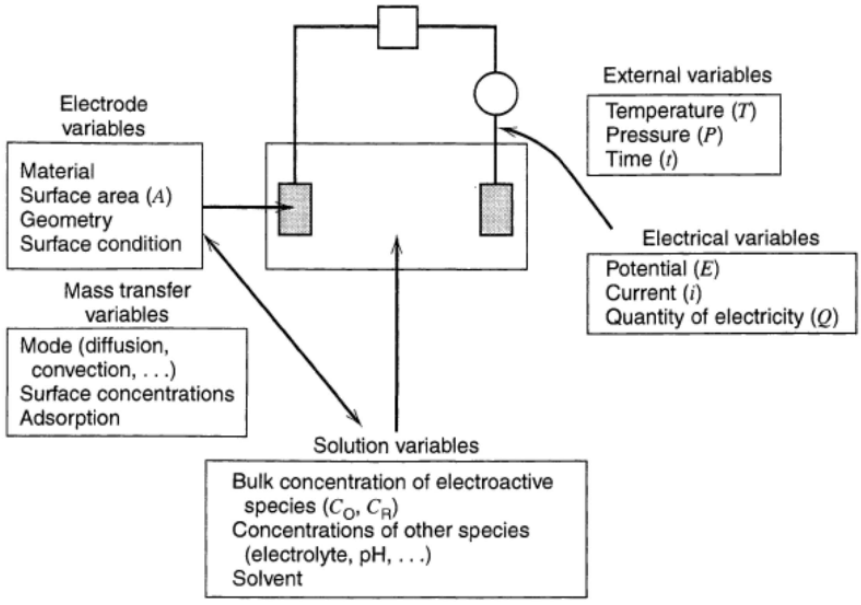

Figure 2.10: Important parameters in an electrochemical cell.

To investigate the electrochemical behaviour of a specific solution is possible to consider the electrochemical cell as a black box and observe its response to a certain applied perturbation (e.g potential step). It is necessary to hold certain variables of the electrochemical cell constant and observe how other variables vary (usually current, potential or concentration) with changes in the input stimuli.

It will useful to consider more closely the nature of the current and the potential in an electrochemical cell. What is the current generated by a redox? The faraidic current has a direct proportional relation with the electrolysis rate of the specie involved into the reaction:

$$i(amperes) = \frac{dQ}{dt}(coulombs/s) \tag{2.16}$$

$$\frac{Q}{nF}\frac{coulombs}{coulombs/mol} = N(molelectrolyzed) \tag{2.17}$$

where n is the stoichiometric number of electrons consumed in the reaction:

$$Rate\frac{mol}{s} = \frac{dN}{dt} = \frac{i}{nF} \tag{2.18}$$

This is the rate for a type of reactions called *homogenous* reaction because it occurs everywhere in the electrochemical system at a uniform rate. But understand the reaction rate on the electrode surface is more complex: the reactions that takes place on the electrodes are called *heterogeneous* reactions because they occur only on the electrode surface. Since the electrode reactions are heterogeneous their reaction rates are usually expressed in units of *mol/s* per unit of area:

$$\text{Rate } \left(\frac{\text{mol}}{\text{s} \cdot \text{cm}^2}\right) = \frac{I}{nFA} = \frac{j}{nF} \tag{2.19}$$

where $j = I/A$ is the current density (A/cm^2) and $F \approx 96485$ C mol^{-1}.

Information about an electrode reaction is often gained by determining current as a function of potential (by obtaining i-E curves). If a cell has a defined equilibrium potential that potential is an important reference point of the system. The departure of the electrode potential (or cell potential) from the equilibrium value upon passage of faradaic current is called *polarization*. The extent of polarization is measured by the *over* potential, η:

$$\eta = E - E_{eq} \tag{2.20}$$

Current-potential curves, particularly those obtained under steady-state conditions, are sometimes called polarization curves.

Consider an overall electrode reaction:

$$O + ne^- \rightarrow R \tag{2.21}$$

composed of a series of steps that cause the conversion of the dissolved oxidized species, O, to a reduced form, R, also in solution.

In general, the current (or electrode reaction rate) is governed by the rates of processes

such as:

1. Mass transfer (e.g., of O from the bulk solution to the electrode surface).
2. Electron transfer at the electrode surface.
3. Chemical reactions preceding or following the electron transfer. These might be homogeneous processes or heterogeneous ones on the electrode surface.
4. Other surface reactions, such as adsorption, desorption, or crystallization (electrodeposition).

The simplest reactions involve only mass transfer of a reactant to the electrode, heterogeneous electron transfer involving non-adsorbed species, and mass transfer of the product to the bulk solution.

When a steady-state current is obtained, the rates of all reaction steps in a series are the same. The magnitude of this current is often limited by the inherent sluggishness of one or more reactions called rate-determining steps.

The more facile reactions are held back from their maximum rates by the slowness with which a rate-determining step disposes of their products or creates their reactants.

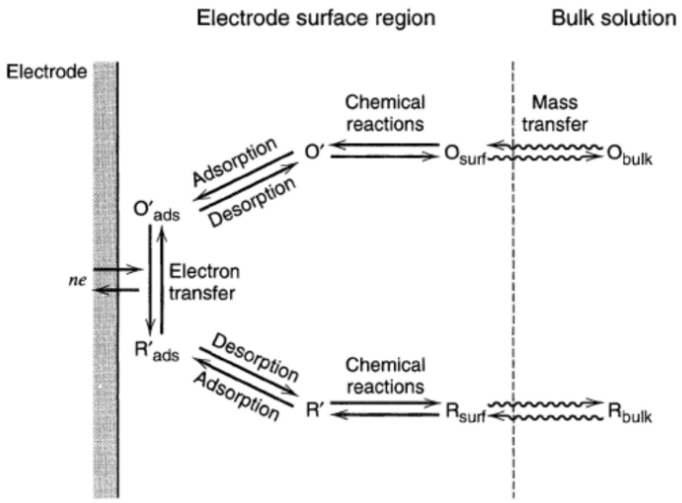

Figure 2.11: Current vs potential curve for a nernstian reaction involving two soluble species with only oxidant present initially.

So if we understand i, we must be able to describe the rate of the reaction,v, at the electrode surface.

$$\text{Rate } \left(\frac{\text{mol}}{\text{s} \cdot \text{cm}^2}\right) = \frac{i}{nFA} = \frac{j}{nF} \tag{2.22}$$

The simplest electrode reactions are those in which the rates of all associated chemical reactions are very fast compared to those of the mass-transfer processes. The surface

concentrations on the electrode of the species involved in the charge-transfer process will be related to the electrode potential by an equation on Nerst form.

$$E = E^{0'} + \frac{RT}{nF} ln \frac{C_O}{C_R} \tag{2.23}$$

where :

- E is the half-cell reduction potential at the temperature of interest.
- E^0 is the standard half-cell reduction potential.
- R is the universal gas constant $= 8.314472\ \mathrm{J\,K^{-1}\,mol^{-1}}$.
- T is the temperature in Kelvin.
- n is the number of moles of electrons transferred in the cell reaction or half-reaction.
- F is the Faraday constant, the number of coulombs per mole of electrons $= 9.64853399 \times 10^4\ \mathrm{C\ mol^{-1}}$.
- C_O is the concentration of the species O.
- C_R is the concentration of the species R.

The meaning of the Nerst's equation is that with an increased potential the ratio $\frac{C_O^0}{C_R^0}$ will increase and on the contrary with a reduced potential the ration will decrease.

The net rate of the electrode reaction, v_r, is governed only by the rate at which the electroactive species reach the surface by mass transfer, v_{mt}.

$$v_r = v_{mt} = \frac{i}{nFA} \tag{2.24}$$

Such electrode reactions are often called reversible or nernstian, because the principal species obey thermodynamic relationships at the electrode surface.

The modes of mass transfer are:

1. Migration: movement of a charged body under the influence of an electric field (a gradient of electrical potential).
2. Diffusion: movement of a species under the influence of a gradient of chemical potential (a concentration gradient).
3. Convection: stirring or hydrodynamic transport. Generally fluid flow occurs because of natural convection (caused by density gradients) and forced convection, and may be characterized by stagnant regions, laminar flow, and turbulent flow.

Usually, voltammetry techniques are applied to reversible processes that present only diffusive phenomena, and therefore it is possible to study the reaction through Fick's law.

Consider the reduction of a species O at a cathode:

$$O + ne^- \longrightarrow R \tag{2.25}$$

Once electrolysis of species O begins, its concentration at the electrode surface, $C_O(x = 0)$, becomes smaller than the bulk concentration C_O* (far from the electrode).

We assume here that stirring is ineffective at the electrode surface, so the solution velocity term need not be considered at $x = 0$. This simplified treatment is based on the idea that a stagnant layer of thickness δ_O exists at the electrode surface (the Nernst diffusion layer), with stirring maintaining the concentration of O at C_O* beyond $x = \delta_O$.

Since we also assume that there is an excess of supporting electrolyte, migration is not important, and the rate of mass transfer is proportional only to the concentration gradient at the electrode surface.

$$v_{mt}(\frac{dC_O}{dx})_{x=0} = D_O(\frac{dC_O}{dx})_{x=0} \tag{2.26}$$

Assuming a linear concentration gradient withing the diffusion layer close to the electrode surface:

$$v_{mt} = D_O(\frac{[C_O^* - C_O]_{(x=0)}}{\delta_O}) \tag{2.27}$$

or:

$$v_{mt} = m_O[C_O^* - C_O]_{(x=0)} \tag{2.28}$$

where m_O is the *mass-transfer coefficient* (cm/s).

$$\frac{i}{nFA} = m_O[C_O^* - C_O]_{(x=0)} \tag{2.29}$$

$$\frac{i}{nFA} = m_R[C_R - C_R^*] \tag{2.30}$$

The values of $C_O(x = 0)$ and $C_R(x = 0)$ are functions of the electrode potential, E. The largest rate of mass transfer of O occurs when $C_O(x = 0) \ll C_O^*$. The value of the current under these conditions is called *limiting current*.

$$i_l = nFAm_OC_O^* \tag{2.31}$$

and

$$C_O(x = 0) = \frac{i_l - i}{nFAm_O} \tag{2.32}$$

When the limiting current flows, the electrode process is occurring at the maximum rate possible because O is being reduced as fast as it reaches the electrode surface. If R is initially absent, $C_R^* = 0$ and $C_R = 0$ is:

$$C_R(x = 0) = \frac{i}{nFAm_R} \tag{2.33}$$

$$E = E^{0'} - \frac{RT}{nF} ln \frac{m_O}{m_R} + \frac{RT}{nF} ln \frac{i_l - i}{i} \tag{2.34}$$

when $i = \frac{i_l}{2}$:

$$E = E_{1/2} = E^{O'} - \frac{RT}{nF} ln \frac{m_O}{m_R} \rightarrow E = E_{1/2} + \frac{RT}{nF} ln \frac{i_l - i}{i} \tag{2.35}$$

where $E_{1/2}$ is indipendent of the reactant concentrations and is characteristic of the O/R system.

2.1.5 Electrodes

All electrochemical cells require at least two electrode, since the potential of a given electrode can only be measured relatively to another reference electrode, which should have a constant potential. Otherwise in voltammetric analysis, it is necessary to apply a potential E to an electrode and simultaneously monitor the resulting current flowing in the cell. Using a two electrodes system it would not be possibile due both the potential drop caused by the resistance of the solution and the polarization of the counter electrode, necessary for the measurement of the current [14]. A better control of the potential is achieved using a three-electrode system using a potentiostat to monitor the potential of the working electrode (WE) than the reference electrode (RE) while the current flows across the WE and counter electrode (CE).

Working Electrode - WE

The working electrode works as a source or a drain of electrons to allow an optimal electrons transfer with the surrounding solution. It has to be made of a conductive material that is electrochemically inert in the potential range of the electrochemical experiment. The most used materials for the WE are platinum, gold, glassy-carbon, mercury, pyrolytic graphite and other metal and semiconductor materials [15]. A regular and well-defined shape of the WE allows a good control of the surface area exposed to the analyte: this is very important for the quantitative interpretation of the results of the CV experiments.

Reference Electrode - RE

The reference electrode should primarily be able to mantain a known constant potential during the measurement. If an electrode doesn't vary its potential [16], because of a current, is called non-polarizable ideal electrode: the impedance of an ideal electrode should be null. Usually the passage of a current through an electrode can degrade the potential [16] and so a real non-polarizable electrode is used: this kind of reference electrode has high input impedance so that a negligible current flows through it. The reference electrode is mostly realized [17] with a Saturated Calomel Electrode (SCE), Hg/Hg_2Cl_2, or with silver/silver chloride electrode, Ag/AgCl. The SCE electrode is a reference electrode based on the reaction between elemental mercury and mercury chloride (calomel). The aqueous phase in contact with the mercury and Hg_2Cl_2 is a saturated solution of potassium chloride in water. For years this has been the most widely used reference electrode. The silver/silver-chloride electrode is made of a silver wire, coated with silver chloride immersed in a solution containing chloride ions, such as KCl. The two reference electrodes have a similar behaviour, since they involve a redox reaction between a poorly soluble chloride and the metal element in a chloride aqueous solution. Another type of traditionally used reference electrode [18] for cyclic voltammetry applications is the Hg/Hg_2SO_4, made of mercury, mercury sulphate and a saturated solution of potassium sulphate: this electrode is designed for certain applications where it is preferable not to use chloride ions.

Counter Electrode - CE

The counter electrode, or auxiliary electrode, can be made of any material with high conductivity and with an inert behaviour in the experiment conditions: the counter electrode is usually a platinum wire or a graphite rod with an adequate surface area. During the voltammetric measurement, on the surface of the CE occurs a redox reaction to balance the reaction that occurs on the WE: the products of this reaction can diffuse towards the working electrode and interfere with it. However in cyclic voltammetry experiments the time-scale is short enough to not allow significant interference.

2.2 Integrated electronics for electrochemical sensing

The implemented system is based on an electrochemical analytical technique called cyclic voltammetry. Voltammetry is an electrochemical technique used to study a compound, a biological material, or an electrode surface properties. In voltammetry we apply a time-dependent potential to an electrochemical cell and measure the resulting current as a function of that potential. The electrochemical cell used in voltammetry, in most cases, made of three electrodes, respectively called working, reference and counter electrode. A time-dependent potential excitation signal is applied between the working electrode and the reference electrode and the current that flows between the working and counter electrode is measured. Current peaks, observed at specific applied voltages, are due to specific redox reactions running on the working electrode surface. Cyclic voltammetry (CV) consists of cycling the potential of the working electrode: the excitation signal for CV is a linear potential scan with a triangular waveform with bipolar range.

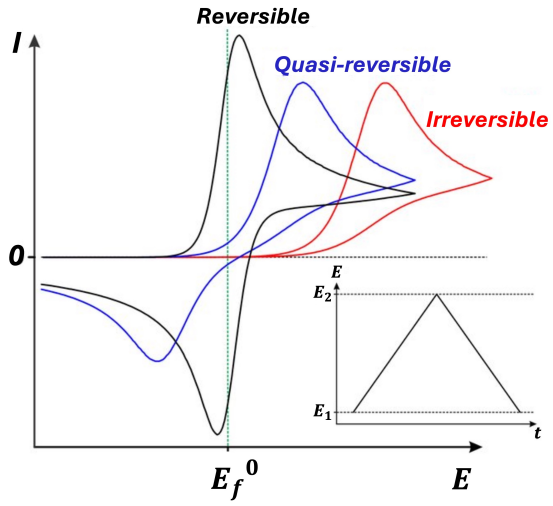

Figure 2.12: Typical voltammogram curve for a reversible redox reaction.

The voltammogram is a display of the current (vertical axis) versus potential (horizontal axis) because the potential varies linearly with time, the horizontal axis can also be thought as a time axis, as shown in Fig 2.12. This is helpful in understanding the fundamentals of the technique. Cyclic voltammetry is perhaps the most versatile electro-analytical technique for the study of electro-active species. This technique is often the first experiment performed in an electrochemical study to assess the redox behaviour, reversibility of electron transfer, and the kinetics of electrochemical reactions of the species under investigation. By analyzing the shape, position, and peak currents of the voltammogram, important information can be obtained regarding oxidation and reduction potentials, diffusion coefficients, and reaction mechanisms. Moreover, cyclic voltammetry allows for the identification of intermediate species, evaluation of electrode surface processes, and

comparison of experimental data with theoretical models, making it a fundamental tool in both analytical and mechanistic electrochemistry.

2.2.1 Potentiostat Circuit Design

As discussed before, a potentiostat requires three electrodes: the Working Electrode (WE), where the electrochemical process of interest takes place; the Reference Electrode (RE), which sets and controls the potential of the system; and the Counter Electrode (CE), which completes the circuit and carries the current from the WE. Different configurations can be obtained depending on which electrode is connected to ground.

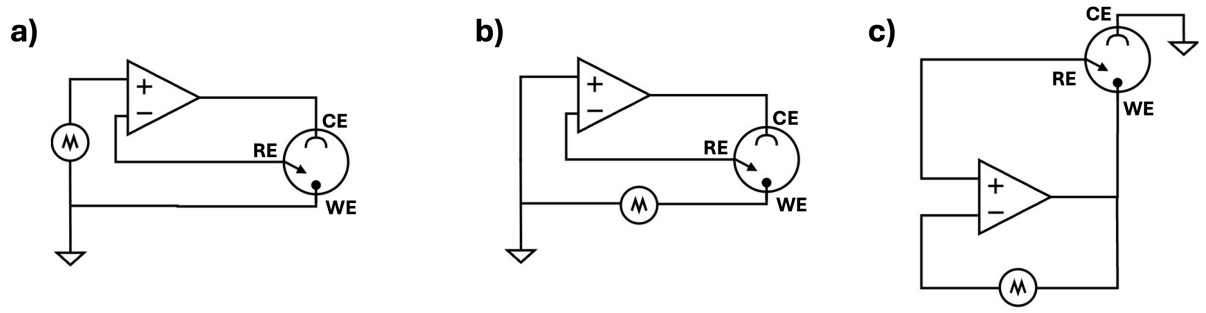

Figure 2.13: The three basic configurations for potentiostatic electrode polarization: a) Grounded WE; b) Grounded RE; c) Grounded CE

Grounded Counter Electrode

The interface is correctly described in Fig. 2.14, where the desired potential is applied between WE and RE, and the current flows between WE and CE. The RE must be biased in a way that prevents current flow to ensure accurate knowledge of the interface potential. This is achieved by using a voltage follower, as shown in Fig. 2.14. A current amplifier ensures sufficient gain to reliably measure the redox current. Both the voltage follower and current amplifier are implemented with operational amplifiers.

The configuration in Fig. 2.14 has two main advantages: the high input impedance of the voltage follower prevents any current through the RE, and the transimpedance amplifier measures the current of the WE. The redox current is converted to voltage as:

$$V_{\text{out}} = R_1 I_W \tag{2.36}$$

This setup uses two amplifiers and leaves the CE grounded. While it benefits from typical OpAmp advantages (very low input current, high input impedance, high gain, low offset voltage), the drawback is the large number of components, which can introduce mismatch and temperature-dependent variations.

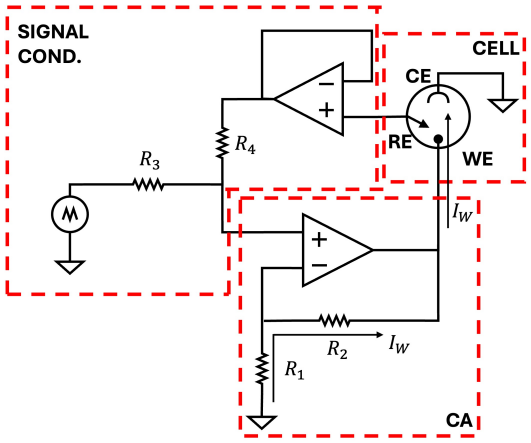

Figure 2.14: Grounded CE configurations with operational amplifiers

Grounded Working Electrode

To reduce component count, the ground can be shifted from the CE to the WE, creating the *grounded WE* configuration (Fig. 2.15). A control amplifier with very high input resistance and zero input current drives the RE, while a transimpedance amplifier converts the current through the WE:

$$V_{\text{out}} = -R_f I_W \tag{2.37}$$

Although the WE is not physically grounded, it operates at *virtual ground* due to the negative feedback of the amplifier. This reduces the number of components but introduces a potential risk of saturation in the feedback loop.

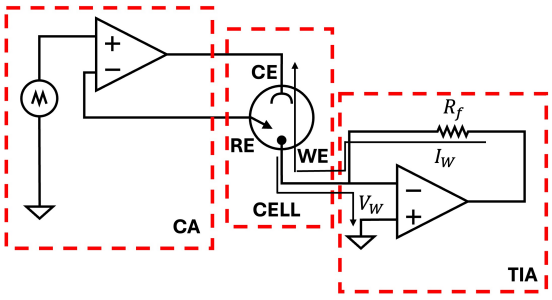

Figure 2.15: Grounded WE configurations with operational amplifiers

The voltage drops across the CE and RE can be written as:

$$V_{RC} = (R_{CE} + R_{SC})I_W, \quad V_R = V^+ = V^- = V_R \tag{2.38}$$

Applying Kirchhoff's Voltage Law to the loop of the control amplifier:

$$V_{\text{out,CA}} = V_{\text{in}} + (R_{CE} + R_{SC})I_W \tag{2.39}$$

The amplifier may saturate if the output voltage exceeds the supply:

$$V_{\text{in}} + (R_{CE} + R_{SC})I_W > V \tag{2.40}$$

Grounded Reference Electrode

Finally, a grounded RE configuration can be attempted (Fig. 2.16), but it is not effective. To ground the RE, the current in the CE must be zero. Consequently, the current from the WE flows through the RE to ground. The CE then behaves like the RE, and the RE behaves like the CE, so the system collapses back into the grounded CE configuration. Thus, a grounded RE configuration does not provide correct operation.

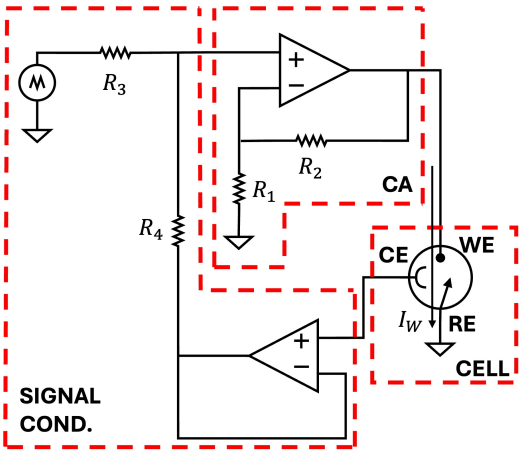

Figure 2.16: Grounded RE configurations with operational amplifiers

2.2.2 System design and realization

The developed device, as reported in [**Paper IV**] is a potentiostat configured with a grounded working electrode, specifically designed for performing electrochemical analyses based on the cyclic voltammetry (CV) technique. Cyclic voltammetry is a potentiodynamic electrochemical method that applies a time-varying potential to the working electrode while measuring the resulting current response. This technique provides detailed insight into the redox behaviour, kinetics, and electrochemical properties of analytes at the electrode–electrolyte interface [19]. A standard CV experiment employs an electrochemical cell three electrodes:

- Working electrode (WE)
- Reference electrode (RE)
- Counter electrode (CE)

All the voltammetric techniques implies the application of an electrical potential on one couple of electrodes (WE/RE) and the measurement of the produced current flowing between another couple of electrode (WE/CE). Current peaks, measured in respect of specific potential values of the input signal, are caused by oxidation or reduction phenomena occurring on the surface of the working electrode. Usually current at the working electrode is plotted versus applied voltage to obtain the cyclic voltammogram trace. Oxidation and reduction reactions are complementary chemical processes in which the oxidation states of atoms change. Redox reactions cause both reduction process, in which one reactant acquire electrons, and a complementary oxidation process, in which one reactant lose electrons:

- Oxidation is the loss of electrons or an increase in oxidation state by a molecule, atom, or ion.
- Reduction is the gain of electrons or a decrease in oxidation state by a molecule, atom, or ion.

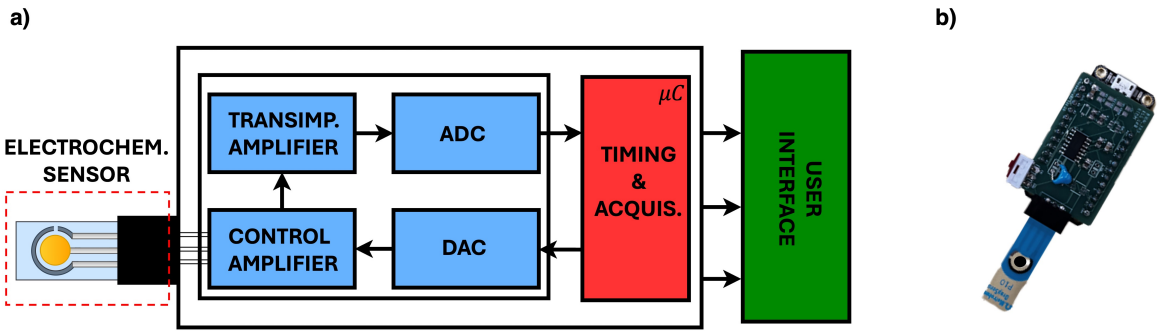

Figure 2.17: a) Functional block representation of the implemented circuit. b) Picture of physical device.

The device includes a microcontroller ATSAMD21G18 ARM Cortex M0 Processor (Adafruit Industries, New York City, NY, USA), clocked at 48 MHz and operating at 3.3 V logic. This kind of interface provides Bluetooth low-energy connectivity for real-time wireless communication. The presence of a 3.7 V 500 mAh battery pack and a 100 mA LiPo battery charger makes the device fully portable and ready to be used in the field. The developed electronic interface is based on a low-noise circuit topology, ensuring high stability and measurement repeatability for the analyzed samples. The device operates with a 3.3 V supply voltage, stabilized by an internal regulator. A dedicated 1.6 V voltage regulator provides the reference potential, allowing the system to handle signals within the ± 1.6 V range. The signal generation stage is implemented with the Microchip MCP4725, a 12-bit resolution digital-to-analog converter (DAC). The DAC offers a minimum output step of 805 μV, communicates via the I^2C protocol, and features a slew rate of 0.55 V/μs, making it well-suited for precise waveform generation in electrochemical applications. The

Analog-Front End interface generates an input signal for the electrochemical cell. The input signal for the electrochemical cell is applied through a control amplifier (CA) to the reference electrode (RE). This configuration limits the current supplied by the signal generator and automatically controls the current supplied by the operational amplifier through the counter electrode (CE). This electronic control ensures stability of the signal, thus enhancing the reproducibility of the sensor response.

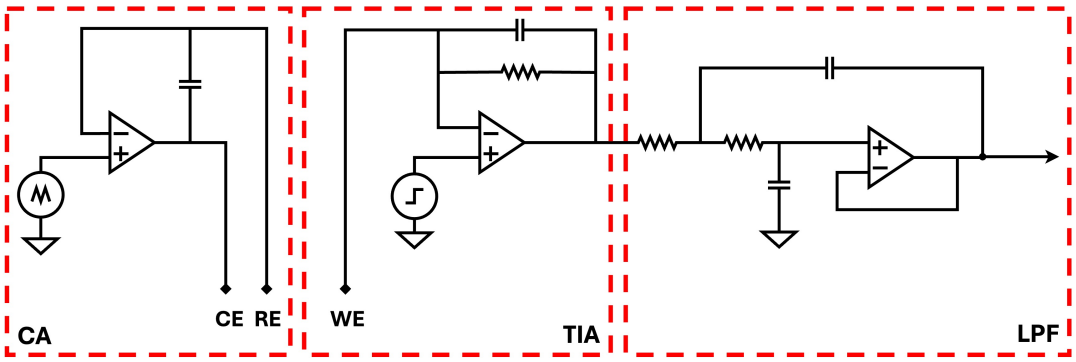

Figure 2.18: Schematic representation of the implemented circuit : a) Signal generator and Control Amplifier (CA); b) Transimpedance amplifier (TIA); c) Sallen-Key Low Pass Filter.

The electrochemical signal generated by oxidation/reduction processes at the working electrode is converted into a measurable voltage through a transimpedance amplifier (TIA). This stage performs the current-to-voltage (I–V) conversion, ensuring that the low-level currents produced by the electrochemical cell can be accurately processed. The TIA is equipped with a digitally programmable feedback resistor (AD5243), which allows dynamic adjustment of the transimpedance gain. This design increases the detectable current range and optimizes the measurement sensitivity depending on the experimental conditions. With this approach, the system achieves a theoretical minimum detectable current of 500 nA, significantly enhancing resolution and adaptability.

Following the I–V conversion, the signal is conditioned by an active Sallen–Key low-pass filter configured as a voltage-controlled voltage source (VCVS). The filter exhibits a flat 0 dB gain in the passband and a two-pole roll-off of $-40\,\mathrm{dB/decade}$ beyond the cutoff frequency. The topology consists of two cascaded RC networks (R4–C2 and R5–C3), with capacitor C2 providing feedback to shape the cutoff response. This configuration ensures both noise suppression and stability of the acquisition chain.

After filtering, the signals—both filtered and unfiltered, together with the buffered input—are routed to a 16-bit analog-to-digital converter (ADC). The acquisition stage is implemented using the Texas Instruments ADS1115, which offers programmable gain, low-noise performance, and high input impedance. With a resolution of 16 bits and a voltage acquisition step of 50 µV, the ADS1115 enables accurate digitization of the electrochemical signal, ensuring high fidelity for subsequent data processing and analysis.

Noise Considerations

It is important to consider the noise generated by the implemented electronic interface. To this regard, it is advisable to evaluate the signal-to-noise ratio (SNR), which represents the ratio between the power of the desired signal and the power of the noise present in the circuit. The noise evaluation was performed using LTSpice (Analog Devices, Inc., Wilmington, MA, USA). The maximum and minimum noise obtained by varying the feedback resistance of the TIA has been calculated. In both configurations, where R3 is equal to 100 Ω or in the configuration with maximum gain where R3 is 100 kΩ, the noise current is 91 pA. The reason is that the main contribution is attributed to the operational amplifier (OP484). The use of high-performance components designed for noise reduction, along with an optimized configuration of the electronic interface, results in a noise current of 91 pA, which is considerably lower than the minimum detectable current of 500 nA by the ADC. The magnitude of the VRMS noise generated by the device is 1.51 μV.

Firmware and Software

The control code developed for the device is designed to apply various electrochemical analysis techniques, such as Cyclic Voltammetry (CV), Square Wave Voltammetry (SWV), and Chronoamperometry (CA). The acquired data can be sent via USB or BLE to the paired device and displayed through a cloud-based user interface. The interface not only includes the measurement history but also allows for analysis and local saving of the data. The whole device is compact (53 × 21 mm), allowing its implementation in the field.

Device validation

To verify the accuracy and reliability of the developed portable potentiostat, cyclic voltammetry (CV) measurements were performed using potassium ferricyanide ($K_3[Fe(CN)_6]$) [19] as a model analyte. This redox couple is widely used in electrochemical characterization due to its well-defined, reversible behavior, high solubility in aqueous solutions, and stable electrochemical response, making it an ideal benchmark for evaluating both sensitivity and linearity of newly developed instrumentation. Three concentrations (1, 2, and 3 mM in dH_2O) were tested in a standard three-electrode setup consisting of a Metrohm 250BT gold working electrode (4 mm diameter), a platinum counter electrode, and a Ag/AgCl reference electrode. CV measurements were conducted in the potential window of [-1,+1] at a scan rate of 50 mV/s, and each experiment was repeated three times to assess reproducibility as shown in Fig. 2.19 a).

The voltammograms obtained with the developed potentiostat showed the expected

reversible ferricyanide/ferrocyanide peaks:

$$[Fe(CN)_6]^{3-} + e^- \leftrightharpoons [Fe(CN)_6]^{4-} \tag{2.41}$$

with anodic peak currents increasing proportionally with concentration. The measured peak currents were $i_{pa}^{\text{dev}} = \{12.22, 24.37, 36.52\}$ μA, in good agreement with the PalmSens 4 potentiostat ($i_{pa}^{\text{PS}} = \{12.02, 24.07, 36.98\}$ μA, relative error $< 1.8\%$), as reported in the table in Fig. 2.19 b). This confirms that the portable device accurately captures concentration-dependent changes in redox current, demonstrating both sensitivity and reproducibility comparable to a laboratory-grade instrument.

The electro-active area of the working electrode was estimated using the Randles–Ševčík equation [20]:

$$i_p = 2.69 \times 10^5 \, n^{3/2} \, A \, D^{1/2} \, C \, v^{1/2} \tag{2.42}$$

with $n = 1$, $D = 7.6 \times 10^{-6}$ cm^2/s, $v = 50m$ V/s, and C in mol/cm^3. Inverting this equation with the experimental peak currents yielded an effective electro-active area of $A_{\text{eff}} \approx 0.0735$ cm^2. The proportion of the electrode surface that is electro-active can be expressed as $A_{\text{real}} = A_{\text{eff}}/A_{\text{geom}} \approx 0.584$, where $A_{\text{geom}} = 0.126$ cm^2 is the nominal geometric area. This value is consistent with expectations for standard commercial electrodes and reflects realistic factors such as partial wetting, surface roughness, and finite diffusion layers.

Overall, the validation demonstrates that the developed portable potentiostat provides reliable, reproducible, and quantitative measurements of a reversible redox system, with performance closely matching that of a commercial benchtop instrument, while maintaining the advantages of portability and field-deployability. Moreover, the device exhibits a high Technology Readiness Level (TRL), highlighting its robustness and maturity, and its characteristics make it highly suitable for integration into industrial processes and on-site analytical applications.

2.3 Summary and Future Perspectives

This chapter provides an overview of the principles and applications of electrochemistry and circuit architecture for electrochemical sensing readout. The importance of optimizing parameters for electrochemical analysis, reducing system complexity and cost, and enhanced scalability and flexibility in portable electrochemical systems is emphasized. For this reason, circuit architecture with advantages and disadvantages are discussed and thoroughly evaluated for implementing a miniaturized system to achieve a compact and stable electrochemical device for real-time analysis. The future outlook for portable electrochemical sensing systems appears highly promising. Advances in electrochemistry, circuit design, and miniaturization are expected to further enhance the capabilities of

a)

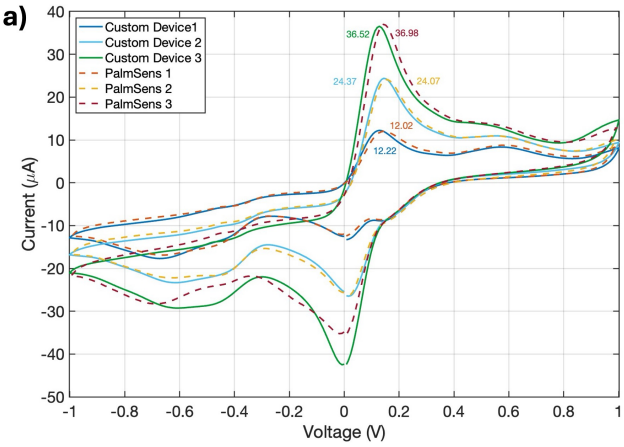

b)

Conc. [mM]	Developed Device (μA)	Palmsens 4 (μA)	Rel. Error (%)
1	12.22	12.02	1.7
2	24.37	24.07	1.2
3	36.52	36.98	1.3

Figure 2.19: a) Overlay of cyclic voltammograms measured with the developed potentiostat and the PalmSens 4 potentiostat for 1, 2, and 3 mM potassium ferricyanide. b) Comparison of anodic peak currents (i_{pa}) measured with the developed device and the PalmSens 4 potentiostat.

these devices. Next-generation electrochemical readout systems will feature optimized circuit architectures that balance performance, stability, and scalability while maintaining a compact size. Such systems will enable real-time monitoring and long-term analysis, expanding their application to fields such as healthcare, environmental monitoring, and biochemical research. Additionally, ongoing efforts to reduce system complexity, lower cost, and improve flexibility in design and parameter optimization will continue to drive innovation in portable electrochemical devices, opening new opportunities for accurate and reliable real-time sensing across diverse applications.

Chapter 3

Bio-impedance Spectroscopy: An Overview

Over the past century, the study of bioimpedance spectroscopy (bio-Z) has provided fundamental insights into the electrical properties and physiological behavior of biological tissues. In essence, bio-Z relies on the application of Ohm's law to living systems: a known current or voltage stimulus is applied to the tissue at a specific frequency, and the corresponding voltage or current response is measured. To ensure that the measurement remains non-invasive and does not compromise cellular integrity, the amplitude of the excitation signal must be sufficiently low to avoid membrane disruption, thereby allowing the study of the intrinsic ability of cells to store and dissipate electrical energy. The frequency range employed in bio-Z measurements depends on the specific electrical phenomena of interest within the biological system under investigation.

Early investigations, dating back to the mid-twentieth century, explored bio-Z at single and multiple frequencies (bio-Z spectroscopy) to characterize the frequency-dependent response of different tissues, to relate the measured impedance to body water and electrolyte content, and to examine various physiological variables such as thyroid activity, basal metabolic rate, estrogenic function, and blood perfusion in human and animal models [21, 22]. In the early 1990s, exploratory studies focused on estimating body composition from bio-Z measurements using commercially available instruments. These pioneering works laid the foundation for modern bio-Z-based diagnostic and monitoring techniques currently employed in clinical practice. Notable examples include impedance cardiography (ICG)—also referred to as impedance plethysmography (IPG) or transthoracic electrical bioimpedance (TEB)—, transcranial bioimpedance (TCB), bioimpedance analysis (BIA), electrical impedance tomography (EIT), and, more recently, electrical impedance myography (EIM) [21].

These techniques have been successfully applied in the assessment of cardiac and pulmonary function [23, 24], the monitoring of intracranial pressure following brain injury [25, 26], whole-body and segmental composition analysis [27], the imaging of internal

structures [28, 29], and the evaluation of muscle health [30]. Moreover, bio-Z spectroscopy has found additional applications in the assessment of skin hydration [31, 32], cancer diagnosis [33], detection of tissue ischemia [34, 35, 36], monitoring of wound healing and edema [37, 38], and catheter-based intraoperative monitoring [39, 40, 41, 42].

Beyond the clinical domain, bio-Z spectroscopy has been extensively utilized in life sciences and laboratory diagnostics for the measurement, analysis, and imaging of individual cells, cell cultures, and suspensions [43]. Furthermore, it has been adopted in the food industry for the evaluation of product quality [44]. The aforementioned examples represent only a subset of the numerous applications currently reported in the scientific literature.

In recent years, there has been a marked increase in the availability of commercial instruments and systems integrating bio-Z spectroscopy, driven by the versatility, simplicity, and broad applicability of the technique. From an instrumentation perspective, bio-Z measurement requires specialized electronic circuitry capable of delivering the excitation signal and accurately capturing the tissue response through electrodes. These systems must ensure that the applied and acquired signals are free from external disturbances and maintain reliable performance across a wide range of bioimpedance values. Additionally, factors such as electrode configuration, inter-electrode distance, and electrode material significantly influence the measured bioimpedance and must therefore be carefully optimized for each specific application. The following sections discuss these aspects in greater detail.

3.0.1 Electrical Properties of Biological Tissue

In its most simple interpretation, the measured bioimpedance Z_{bio} is the ratio between the voltage and current across the tissues under test. Assuming a sinusoidal current signal for interrogation I_s, and thus a voltage response from tissues V_{in}, the complex Z_{bio} in phasor representation is given by:

$$Z_{\text{bio}} = \frac{V_{\text{in}}}{I_s} = \frac{V_{\text{pk}} e^{j(\omega_s t + \theta)}}{I_{\text{pk}} e^{j\omega_s t}} = \frac{V_{\text{pk}}}{I_{\text{pk}}} e^{j\theta} \tag{3.1}$$

where V_{pk} and I_{pk} are the peak voltage response and interrogation current, respectively, ω_s is the angular frequency of the interrogation signal, and θ is the phase delay caused by the impedance of the tissues under test, as it can be seen in Fig. 3.1(a). Since Z_{bio} is a complex quantity, it can be generally represented in polar form as follows:

$$Z_{\text{bio}} = |Z_{\text{bio}}| e^{j \arg(Z_{\text{bio}})} = \sqrt{R_{\text{bio}}^2 + X_{\text{bio}}^2}\, e^{j \tan^{-1}(X_{\text{bio}}/R_{\text{bio}})} \tag{3.2}$$

where R_{bio} and X_{bio} are the bioimpedance resistance and reactance, respectively, and represent the real and imaginary parts of Z_{bio}. Therefore, the bioimpedance modulus and

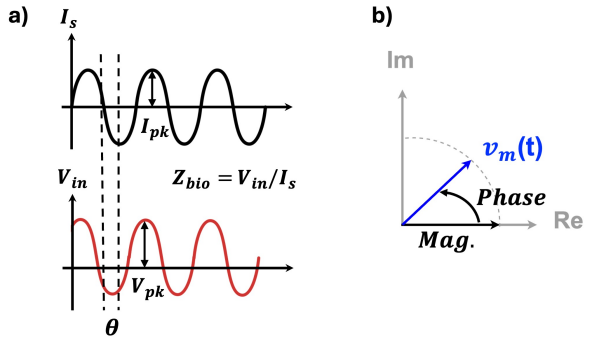

Figure 3.1: (a) Illustration of the interrogation current (I_s) and the voltage response from tissues V_{in}. (b) Phasor diagram representation of Z_{bio}.

argument are given by:

$$|Z_{\text{bio}}| = \sqrt{R_{\text{bio}}^2 + X_{\text{bio}}^2}, \qquad \arg(Z_{\text{bio}}) = \tan^{-1}\left(\frac{X_{\text{bio}}}{R_{\text{bio}}}\right) \tag{3.3}$$

It follows that the bioimpedance is fully characterized either by its magnitude and phase or, equivalently, by its real and imaginary parts. In particular, one can write :

$$\begin{aligned} |Z_{\text{bio}}| &= \frac{V_{\text{pk}}}{I_{\text{pk}}} = \sqrt{R_{\text{bio}}^2 + X_{\text{bio}}^2}, \\ \arg(Z_{\text{bio}}) &= \theta = \tan^{-1}\left(\frac{X_{\text{bio}}}{R_{\text{bio}}}\right) \end{aligned} \tag{2.3}$$

as illustrated in Fig. 3.1(b).

Since living tissues are wet biomaterials, they behave as electrolytic conductors that allow ionic migration [45]. Consequently, hydration level, electrical double-layer formation, and electrode polarization all contribute to their measured electrical behaviour. This behaviour, including impedance, is governed by the dielectric properties of the medium, namely relative permittivity ε_r and conductivity σ. These may be defined as complex quantities to account for capacitive and conductive loss components:

$$\sigma \equiv \sigma' + j\,\sigma'', \qquad \varepsilon \equiv \varepsilon' - j\,\varepsilon'' \equiv \left(\varepsilon_r' - j\,\varepsilon_r''\right)\varepsilon_0 \tag{2.4}$$

where ε_0 is the permittivity of free space.

For intuition, Z_{bio} can be modeled as a non-ideal capacitor with electrode area A and spacing d (cf. Fig. 3.2), i.e., a lossy dielectric. If the DC conductance in the equivalent circuit is negligible, the tissue admittance $Y_{\text{bio}} = 1/Z_{\text{bio}}$ can be expressed as

$$Y_{\text{bio}} = \frac{A}{d}\left(\sigma' + j\,\omega_s\varepsilon'\right) = j\,\omega_s\,C_{\text{bio}} = j\,\omega_s\,\frac{A}{d}\,\varepsilon = j\,\omega_s\,\frac{A}{d}\left(\varepsilon' - j\,\varepsilon''\right) \tag{2.5}$$

which highlights the equivalence between a conductance term and the loss component of

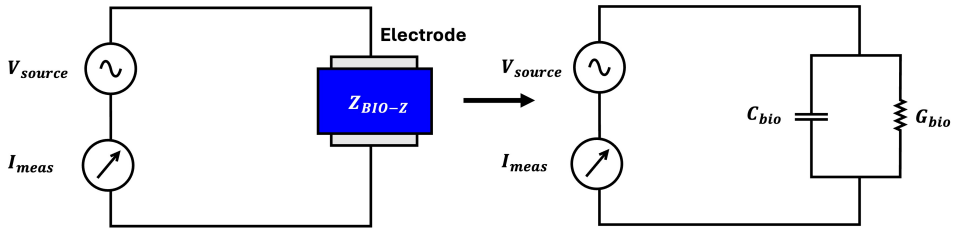

Figure 3.2: Simple parallel RC model for Z_{bio}, driven by an interrogation AC voltage source with measured current response; C_{bio} denotes the equivalent capacitance of the bioimpedance.

the complex permittivity (with the common identification $\varepsilon'' = \sigma'/\omega_s$ when conductivity is absorbed into ε).

In the dielectric viewpoint where conductivity is absorbed into the complex permittivity, the loss term is captured by the imaginary part of ε. Consistency between the forms $Y_{\text{bio}} = \frac{A}{d}(\sigma' + j\,\omega_s\varepsilon')$ and $Y_{\text{bio}} = j\,\omega_s \frac{A}{d}\,\varepsilon$ implies the identification

$$\varepsilon'' \;=\; \frac{\sigma'}{\omega_s} \tag{2.6}$$

Conversely, in the conductive viewpoint where the medium is treated primarily as a conductor endowed with capacitive properties, one adopts a complex conductivity. If the AC losses in the simple RC representation of Fig. 3.2 are negligible, the tissue admittance can be written as

$$Y_{\text{bio}} = \frac{A}{d}\left(\sigma' + j\,\omega_s\varepsilon'\right) = G_{\text{bio}} = \frac{A}{d}\,\sigma = \frac{A}{d}\left(\sigma' + j\,\sigma''\right) \tag{2.7}$$

from which it follows that the imaginary part of the complex conductivity relates to the stored-field term through

$$\sigma'' \;=\; \omega_s\,\varepsilon' \tag{2.8}$$

In practice, permittivity and conductivity data for biological tissues are often reported as ε and σ or as ε' and σ' because the complementary loss terms ε'' and σ'' formally diverge at very low and very high frequencies, respectively [46]. Although the simple capacitor model does not reproduce the full spectral behavior of real tissues, it provides a useful baseline for analyzing dielectric properties and for interpreting single-frequency measurements, which reduce to extracting R_{bio} and X_{bio} from Z_{bio}.

Over the years, numerous models have been introduced to account for these effects and to describe the characteristic response within each dispersion region, including Debye-type networks (such as 2R–1C and 1R–2C forms), constant-phase elements (CPEs) to represent fractional capacitive behavior, the Cole model, and several non-Cole variants [46]. A key refinement by the Cole brothers shifted the frequency dependence from impedance to permittivity, yielding the Cole–Cole formulation, which has become ubiquitous in

bioimpedance research due to its balance of simplicity and fidelity across a wide range of tissues and conditions. In its single-dispersion form, the relative permittivity is written as

$$\varepsilon_r \;=\; \varepsilon_\infty \;+\; \frac{\Delta\varepsilon_m}{1 + \left(j\,\omega_s\tau_m\right)^{\,1-\alpha_m}}, \qquad \Delta\varepsilon_m \;=\; \varepsilon_s - \varepsilon_\infty \tag{2.9}$$

where ε_∞ is the relative permittivity at infinite frequency, ε_s is the static permittivity, and $\Delta\varepsilon_m$, τ_m, and α_m denote the strength, characteristic time constant, and broadening parameter of the dispersion, respectively.

Because biological tissues typically exhibit the four dispersion regions described earlier together with a nonzero static ionic conductivity, a multi-term extension of the Cole–Cole model is often used [47]:

$$\varepsilon_r \;=\; \varepsilon_\infty \;+\; \sum_{m=1}^{4} \frac{\Delta\varepsilon_m}{1 + \left(j\,\omega_s\tau_m\right)^{\,1-\alpha_m}} \;+\; \frac{\sigma_i}{j\,\omega_s\,\varepsilon_0}, \qquad \sigma \;=\; -\,\mathrm{Im}(\varepsilon_r)\;\omega_s\,\varepsilon_0 \tag{2.10}$$

where σ_i is the static ionic conductivity. With appropriate parameter choices, this model has been shown to predict the dielectric behavior of many biological tissues over frequency spans extending from the hertz to the multi-gigahertz range [47].

Accurate modeling of bioimpedance spectra is therefore essential to reproduce their frequency-dependent behavior and to establish reference impedances for the design and evaluation of application-specific biomedical devices. The application and evaluation of these models will be presented in Section 3.1.

3.0.2 Electrodes and Bio-Z Measurement Setups

Electrodes are essential components in bioimpedance measurements, acting as transducers between biological tissues and the electronic interface circuits. They enable the conversion of charge carriers from ionic to electronic form and vice versa at the metal–electrolyte interface. Conventional surface wet-contact electrodes, widely used in bioimpedance applications, typically consist of a metallic element, often Ag/AgCl, coated with an electrolytic gel to improve contact with the skin's outer and inner layers. These electrodes exhibit a half-cell potential V_{hc}, a double-layer capacitance, and both series and parallel resistances.

Although wet electrodes remain the clinical gold standard due to their excellent signal quality, they are unsuitable for long-term wearable monitoring because they can cause skin irritation and discomfort. Dry electrodes have been proposed as an alternative for wearable applications, offering improved comfort and usability [48]. However, the electrical interface of dry electrodes is more complex, as additional processes influence the skin–electrode impedance [49]. The skin–electrode interface can generally be modeled as a layered conductive and dielectric structure, often represented by multiple RC sections connected in series. Depending on electrode type and coupling conditions,

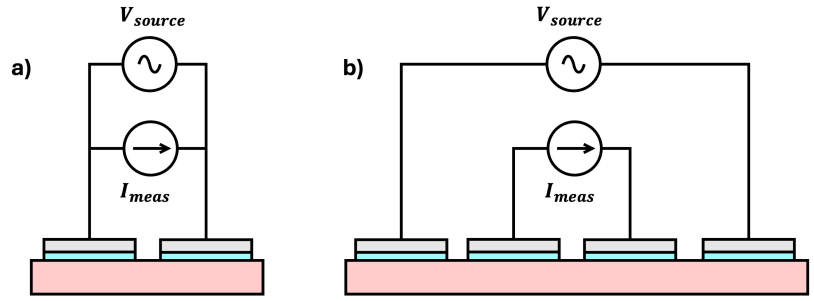

Figure 3.3: Simplified equivalent model for a) bipolar and b) tetrapolar bio-Z measurement setup.

these lumped RC models can approximate the interface behaviour. In many cases, one RC section dominates, allowing the interface to be simplified as a coupling admittance $Y_c = 1/Z_c = G_c + j\omega_s C_c$.

Because electrode interfaces introduce additional impedance in series with the tissue, their effect on bioimpedance measurements must be considered. Two main electrode configurations are commonly used: bipolar and tetrapolar.

Bipolar setups are the simplest, employing a single electrode pair to inject current and measure voltage simultaneously. In this configuration, one electrode sources current while the other sinks it, and the voltage response is measured across the same pair. Fig. 3.3(a) illustrates a simplified equivalent circuit for a bipolar setup, where $Z_{o,\mathrm{cs}} = R_{o,\mathrm{cs}} \parallel 1/(j\omega_s C_{o,\mathrm{cs}})$ and $Z_{i,\mathrm{IA}} = R_{i,\mathrm{IA}} \parallel 1/(j\omega_s C_{i,\mathrm{IA}})$ represent the output impedance of the current source and the input impedance of the instrumentation amplifier (IA), respectively. Ideally, these impedances would be infinite, but practical implementations impose limits. Under ideal assumptions, the interrogation current I_s flows through the series combination of the electrode coupling impedances and the tissue impedance, $Z_c + Z_{\mathrm{bio}}$. Consequently, the measured voltage includes contributions from both the tissue and the electrode interfaces. At low frequencies, Z_c can be very large—hundreds of kilohms to several megohms for commercial electrodes—while Z_{bio} typically ranges from ohms to kilohms depending on electrode spacing. This disparity makes detecting small changes in Z_{bio} challenging in wearable bipolar systems. Nevertheless, bipolar measurements remain useful for estimating Z_c for lead-off detection, assessing electrode contact quality, and mitigating motion artifacts.

Tetrapolar configurations are widely adopted to overcome these limitations. In a tetrapolar setup, two electrodes inject current while a separate pair senses voltage, effectively isolating the measurement from electrode interface impedance. Fig. 3.3(b) shows a simplified equivalent circuit for this configuration. Assuming ideal conditions similar to those in the bipolar analysis, the interrogation current flows through the series combination of the current-injection electrode impedances and the tissue, while the voltage-sensing electrodes draw negligible current. As a result, the measured voltage reflects only Z_{bio}, making tetrapolar setups the preferred choice in clinical bioimpedance spectroscopy and

in multifrequency sEIM applications, where sensitivity and accuracy are critical.

Although electrode coupling impedances are not directly measured in tetrapolar configurations, they still influence the performance of the current source (CS) and the IA. On the injection side, the electrode coupling impedances contribute to the CS load, so the interrogation current I_s flows through an equivalent series resistance of $(2Z_c + Z_{\text{bio}})$. The resulting voltage drop across the CS terminals is dominated by $2Z_c$, which defines the voltage compliance of the CS and limits the linear range of current injection. Furthermore, if Z_c is comparable to the CS output impedance $Z_{o,\text{CS}}$, the accuracy of the injected current is compromised due to the current divider formed by $2Z_{o,\text{CS}}$ and $(2Z_c + Z_{\text{bio}})$. Similarly, on the sensing side, the electrode coupling impedances form a voltage divider with the IA input impedance $Z_{i,\text{IA}}$. If Z_c is comparable to $Z_{i,\text{IA}}$, the voltage signal from Z_{bio} is attenuated at the IA input, which may require higher amplification and effectively reduce the achievable signal-to-noise ratio (SNR) of the bioimpedance readout.

These effects are also present in bipolar measurements and must be considered in such setups. The challenges associated with large electrode coupling impedances are particularly critical in bioimpedance measurements using dry electrodes. Several studies have proposed solutions to mitigate these issues, such as increasing the CS output impedance through closed-loop current drivers to enable accurate current injection, and boosting the IA input impedance to minimize loading effects in voltage readouts. Due to the resistive component of Z_c, the electrode interface also introduces thermal noise, which degrades the SNR of the measured bioimpedance. This noise is shaped by Z_c and is minimized when the contact resistance approaches either zero or infinity, conditions that are practically unattainable. Consequently, electrode type and interface characteristics strongly influence noise performance and often represent the limiting factor in system design.

In addition to loading effects and noise, other non-idealities such as DC offset and motion artifacts must be addressed. DC offset originates from mismatches in the electrodes' half-cell potentials V_{hc} and can saturate the IA. This offset often drifts at low frequencies, exhibiting a $1/f$-like behavior. Motion artifacts arise from lateral or vertical displacement of electrodes during patient movement, which alters both Z_c and V_{hc}. These variations differ across electrodes, producing differential artifacts that corrupt the IA input and reduce SNR. In severe cases, motion artifacts can also saturate the IA. Fortunately, since both DC offset and motion artifacts occur at frequencies below 20 Hz, while most clinical bioimpedance measurements operate above 1 kHz, these components can be effectively removed through high-pass filtering, making them less problematic in practice.

Two common strategies are employed to mitigate noise and artifacts from the electrode interface. The first is skin preparation prior to electrode placement, which involves cleaning and lightly abrading the skin and applying saline solution to reduce contact resistance, typically achieving values between 5 kΩ and 10 kΩ. The second strategy is to maximize the IA input impedance so that the noise contribution from Z_c becomes negligible. This is

straightforward with standard IA topologies when wet electrodes are used, but it becomes challenging with dry or non-contact electrodes, requiring specialized techniques to boost IA input impedance.

3.0.3 Bio-Z Spectroscopy Interface Circuits

As briefly mentioned earlier, bioimpedance measurements can be performed either by applying a voltage stimulus and recording the resulting current (voltage mode) or by applying a current stimulus and recording the resulting voltage (current mode). In practice, current-mode bioimpedance measurements dominate both the scientific literature and commercial clinical equipment. The primary reason is that current-mode operation allows precise control of the amount of current delivered to the patient, which is essential for compliance with IEC 60601-1 safety standards governing patient auxiliary currents—defined as a type of leakage current—under specified human body models. Although similar limits exist for maximum applied voltages, both modes can satisfy these requirements; however, ensuring compliance with current limits is prioritized in bioimpedance systems.

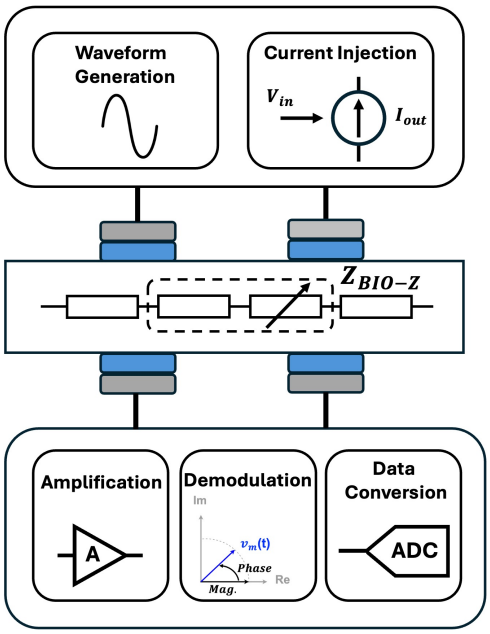

Figure 3.4: Simplified block diagram of a current-mode bio-Z spectroscopy interface.

An additional advantage of current-mode operation is the reduced charging time of stray capacitances, which shortens propagation delays and improves accuracy at higher frequencies, provided that the output impedance of the current source remains sufficiently large. For these reasons, the remainder of this work focuses on current-mode bioimpedance spectroscopy.

A current-mode bioimpedance interface consists of two main functional blocks, as illustrated in Fig. 3.4. The first block is the current signal generator (CSG), which produces and injects an AC current into the tissue under test. The second block is the voltage

readout, which senses and processes the resulting voltage response to compute Z_{bio} and comprises an amplification stage, an analog-to-digital converter (ADC), and a demodulation stage, which may be implemented in either the analog or digital domain. The following sections will review state-of-the-art implementations of these building blocks.

3.0.4 Current Signal Generators

Fig. 3.5 summarizes the most common methods and implementations of the three main stages of current signal generators (CSGs) for bioimpedance spectroscopy. The waveform generation stage can be categorized according to the type of signal produced: single-tone (narrowband) or multi-tone (broadband). The linearity enhancement stage typically employs low-pass filters, which can be implemented in continuous-time or discrete-time domains. Finally, the current injection stage can adopt either an open-loop or a closed-loop topology. Each of these stages and their implementation options is discussed in the following paragraphs.

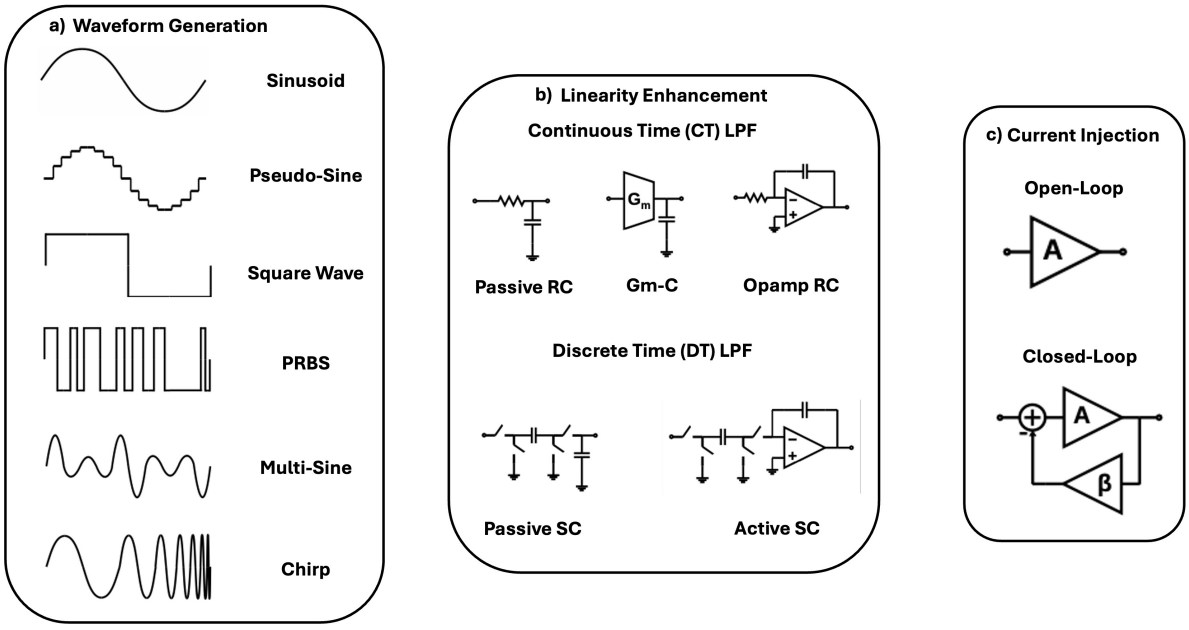

Figure 3.5: Three main stages of bio-Z spectroscopy CSGs and their most common methods and implementations: (a) waveform generation, (b) linearity enhancement, and (c) current injection.

Waveform Generation

The purpose of the waveform generation stage is to produce the excitation signal that will be periodically injected into the tissue. Single-tone signals are the most common choice because of their simplicity and compatibility with narrowband readout architectures. They are relatively easy to generate using oscillators or mixed-signal circuits and simplify demodulation due to their narrowband nature. However, spectroscopy requires

sweeping the frequency of the single-tone signal across multiple points within the α- and β-dispersion ranges, which increases acquisition time proportionally to the number of tones. Multi-tone signals, in contrast, allow simultaneous measurement at multiple frequencies, reducing acquisition time but imposing stricter requirements on readout bandwidth, linearity, and power consumption, as well as more complex demodulation schemes.

Single-tone waveforms are generally implemented as sinusoids, pseudo-sines, or square waves. Sinusoids, typically generated by analog oscillators, offer the best linearity but suffer from poor frequency agility and high area and power costs when covering a wide frequency range, as large capacitors are required for low-frequency tones and power scales with frequency. Square waves, on the other hand, can be generated with high frequency accuracy using PLL-based clocks and simple current-switching circuits, making them significantly more power-efficient. However, their harmonic content introduces distortion in the demodulation process, even though most harmonics lie outside the fundamental band. Pseudo-sine signals represent a compromise between sinusoids and square waves, combining good frequency accuracy and moderate linearity with reasonable implementation complexity. They are generated using a PLL-based clock, digital logic, and a DAC, and their linearity can be improved by increasing DAC resolution and applying oversampling.

Multi-tone waveforms include chirp signals, multi-sine signals, and pseudo-random binary sequences (PRBS). Chirp signals are produced by sweeping the frequency of a single-tone generator and can be processed as narrowband or broadband signals depending on the demodulation strategy. Multi-sine signals provide discrete tones in the frequency domain and offer better SNR than chirps but require crest factor optimization to achieve acceptable linearity. PRBS signals are easier to generate and share implementation similarities with square waves, but their strong harmonic content limits measurement accuracy.

The choice between single-tone and multi-tone excitation ultimately depends on application requirements such as acquisition time, power budget, and system complexity. Nevertheless, single-tone generation remains the dominant approach in state-of-the-art bioimpedance interface ICs, particularly for wearable and ultra-low-power applications, where simplicity and energy efficiency are critical.

3.0.5 Voltage Readout

Fig. 3.6 summarizes the most common methods and implementations of the three main stages of voltage readouts in bioimpedance spectroscopy interfaces: amplification, demodulation, and analog-to-digital conversion. Three instrumentation amplifier (IA) topologies dominate state-of-the-art designs: the three-opamp IA, the current-balancing IA (CBIA), and the capacitively-coupled IA (CCIA). Demodulation can be implemented using either

quadrature (I/Q) techniques or magnitude/phase extraction, while analog-to-digital conversion relies on Nyquist-rate or oversampling ADCs depending on the required dynamic range, bandwidth, and power constraints.

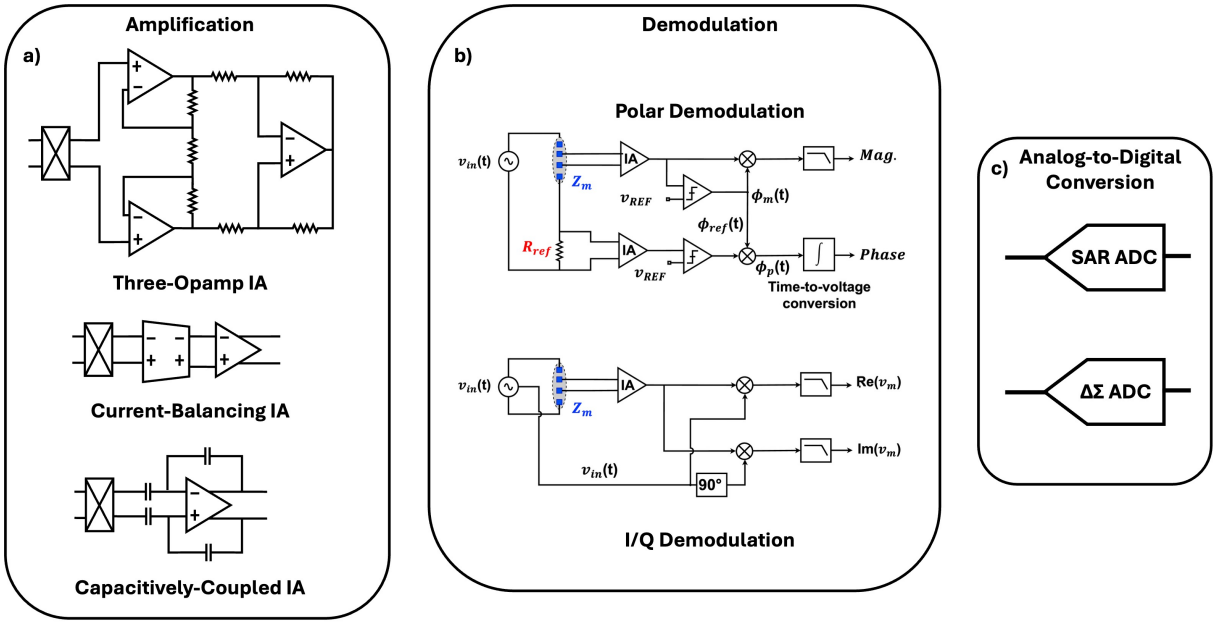

Figure 3.6: Three main stages of bio-Z spectroscopy voltage readouts and their most common methods and implementations: (a) amplification, (b) demodulation, and (c) analog-to-digital conversion.

The amplification stage must extract the small differential voltage response from Z_{bio} while rejecting large common-mode voltages caused by electrode non-idealities and power-line interference. Therefore, high common-mode rejection ratio (CMRR), low input-referred noise, and high input impedance relative to the electrode impedance are essential. Many state-of-the-art interfaces also include a pre-demodulation stage before amplification to down-convert the signal from the generator frequency f_{SG} to an intermediate frequency f_{IF}, reducing the IA bandwidth requirement and improving power efficiency. This approach is only compatible with single-tone excitation architectures, which explains their prevalence in low-power designs.

Among IA topologies, the three-opamp IA offers high input impedance and excellent linearity across a wide input range but suffers from limited CMRR due to resistor and opamp mismatch, as well as relatively high power consumption because it requires three precision opamps. The CCIA provides a more power-efficient alternative by using a single opamp, but its input impedance is constrained by the switched-capacitor input network, which also introduces glitches and noise. Its CMRR depends on capacitor matching, which can be improved with additional feedback loops at the cost of complexity. The CBIA achieves higher CMRR than both three-opamp and CCIA designs while maintaining high input impedance without additional complexity. Its gain is determined by the ratio of feedback resistors in the transimpedance and transconductance amplifiers. Although

the linear input range of CBIAs is limited by the bias current of the transconductance stage, this can be managed by adjusting the injected current amplitude. Depending on the requirements of subsequent stages, the TIA can use a simple resistive load or a closed-loop configuration. These characteristics make CBIAs a flexible and power-efficient solution for modern bioimpedance interfaces.

Demodulation

As mentioned in Section 3.0.1, Z_{bio} can be represented in cartesian form through its real and imaginary components (R_{bio} and X_{bio}), or in polar form through its magnitude and phase ($|Z_{\text{bio}}|$ and θ_{bio}). Two main demodulation strategies, as shown in Fig. 3.7, are found in the literature: quadrature (I/Q) demodulation, which recovers the real and imaginary parts, and polar demodulation, which estimates amplitude and phase directly. Both approaches can be implemented in either the analog or digital domain. Analog techniques typically offer superior power efficiency, while digital implementations achieve higher signal-to-noise ratio (SNR) and throughput, leading to a trade-off between energy consumption and performance.

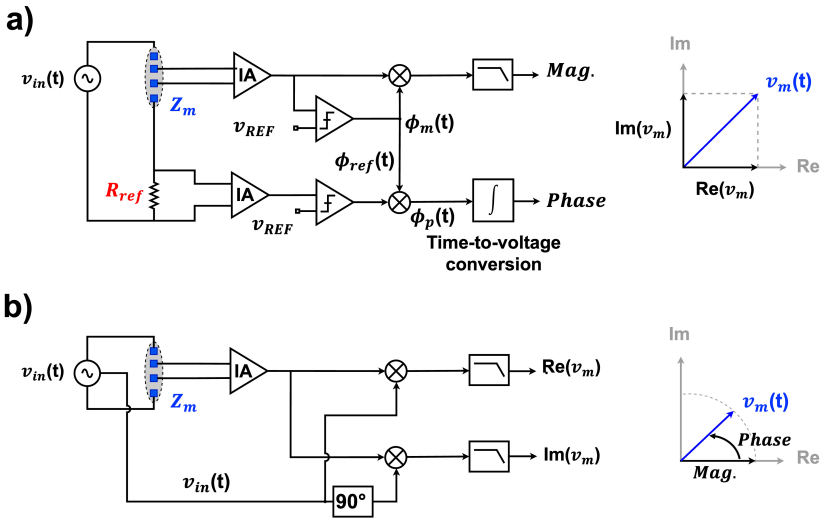

Figure 3.7: Conceptual comparison between I/Q and polar demodulation methods for impedance extraction.

The injected current signal can be expressed as

$$i_{\text{in}}(t) = I_0 \cos(2\pi f_{\text{IN}} t) \tag{3.4}$$

where I_0 and f_{IN} are the amplitude and frequency of the stimulus, respectively. The resulting voltage across the bio-impedance is

$$v_{\text{bioZ}}(t) = I_0 |Z_{\text{bio}}| \cos(2\pi f_{\text{IN}} t + \theta_{\text{bio}}) \tag{3.5}$$

where $|Z_{\text{bio}}|$ and θ_{bio} denote the impedance magnitude and phase.

I/Q Demodulation

In I/Q (quadrature) demodulation, the amplified voltage response from an instrumentation amplifier with gain A_v is

$$V_{\text{out,IA}}(t) = A_v I_0 |Z_{\text{bio}}| \cos(2\pi f_{\text{IN}} t + \theta_{\text{bio}}) \tag{3.6}$$

The signal is then multiplied by in-phase and quadrature reference signals, either sinusoidal or square-wave, to obtain the Cartesian components:

$$v_{\text{Re}}(t) = V_{\text{out,IA}}(t)\cos(2\pi f_{\text{IN}} t) = \frac{1}{2} A_v I_0 |Z_{\text{bio}}| \left[\cos(\theta_{\text{bio}}) + \cos(4\pi f_{\text{IN}} t + \theta_{\text{bio}})\right] \tag{3.7}$$

$$v_{\text{Im}}(t) = V_{\text{out,IA}}(t)\sin(2\pi f_{\text{IN}} t) = \frac{1}{2} A_v I_0 |Z_{\text{bio}}| \left[\sin(\theta_{\text{bio}}) + \sin(4\pi f_{\text{IN}} t + \theta_{\text{bio}})\right] \tag{3.8}$$

Low-pass filtering removes the high-frequency terms, leaving the DC components proportional to the real and imaginary parts:

$$V_{\text{Re,DC}} = \frac{1}{2} A_v I_0 |Z_{\text{bio}}| \cos(\theta_{\text{bio}}) \propto R_{\text{bio}} \tag{3.9}$$

$$V_{\text{Im,DC}} = \frac{1}{2} A_v I_0 |Z_{\text{bio}}| \sin(\theta_{\text{bio}}) \propto X_{\text{bio}} \tag{3.10}$$

From these, the impedance can be reconstructed as:

$$|Z_{\text{bio}}| = \frac{2}{A_v I_0} \sqrt{V_{\text{Re,DC}}^2 + V_{\text{Im,DC}}^2} \tag{3.11}$$

$$\theta_{\text{bio}} = \arctan 2(V_{\text{Im,DC}}, V_{\text{Re,DC}}), \quad Z_{\text{bio}} = R_{\text{bio}} + jX_{\text{bio}} \tag{3.12}$$

Digital I/Q demodulation requires high-resolution DDS and multipliers, which increase power consumption. Analog implementations often use passive mixers with square-wave references for reduced power, though harmonic content can introduce intermodulation errors. Calibration and waveform optimization can mitigate these effects. Despite higher circuit complexity, I/Q demodulation remains the preferred approach in high-accuracy and noise-sensitive systems due to its robustness and precision.

Polar Demodulation

Polar demodulation directly estimates the magnitude and phase of the bio-impedance signal, involving the extraction of the voltage amplitude V_{pk} and the phase delay of the sensed voltage V_{in} with respect to the stimulation current I_s.

In the digital domain, V_{pk} can be obtained through spectral analysis using Fast Fourier Transform (FFT) or matched filtering techniques, which, however, tend to become power-

intensive as the excitation frequency f_{SG} increases. In the analog domain, the same task can be accomplished more efficiently using low-power implementations of peak detectors, which capture the envelope of the bio-impedance response. The phase delay is then determined by comparing V_{in} with a reference voltage signal derived from a sensing resistor in the current-source path. Dedicated phase detectors—typically based on comparators and digital logic circuits such as XOR or D flip-flop configurations—convert this phase difference into a measurable duty cycle or voltage level proportional to the impedance phase.

Usually, a peak detector measures the response amplitude as

$$V_{pk} \approx I_0 |Z_{bio}| \tag{3.13}$$

and, considering that the peak of the current is $I_{pk} \approx I_0$, the impedance magnitude can be computed as

$$|Z_{bio}| = \frac{V_{pk}}{I_{pk}} \tag{3.14}$$

Similarly, a phase detector measures the phase difference between the voltage and current:

$$\theta_{bio} = \phi_v - \phi_i \tag{3.15}$$

allowing the complex impedance to be reconstructed as

$$Z_{bio} = |Z_{bio}| e^{j\theta_{bio}} \tag{3.16}$$

Despite its architectural simplicity and low power consumption, magnitude/phase demodulation relying solely on peak and phase detectors suffers from limited precision, mainly due to sensitivity to DC offsets, harmonic distortion, and noise. To address these limitations, several improved analog demodulation schemes have been proposed, including pulse-width demodulation, time-stamp demodulation, adaptive-sampling methods, and self-mixing rectifier topologies. These techniques aim to enhance accuracy and robustness while preserving the low-power advantage of analog magnitude/phase extraction, making them particularly suitable for wearable and implantable bio-impedance measurement systems.

Analog implementations typically employ comparators, rectifiers, XOR gates, and low-pass filters for phase extraction, while digital approaches rely on FFT-based analysis or matched filters. Although FFT-based demodulation provides high resolution, it becomes increasingly power-hungry at high operating frequencies. In contrast, analog polar demodulation offers simplicity and low energy consumption, making it an attractive solution for portable or implantable bio-impedance sensors, where power and area constraints are critical. However, its accuracy can still be affected by offsets, noise, and harmonic distortion,

requiring careful calibration and circuit optimization to ensure reliable operation.

3.0.6 Analog-to-Digital Conversion

The final stage of the readout chain is analog-to-digital conversion. Two ADC architectures dominate: successive-approximation register (SAR) and delta-sigma ($\Delta\Sigma$). SAR ADCs offer excellent power efficiency for low-bandwidth signals but are typically limited to about 12 ENOB, whereas $\Delta\Sigma$ ADCs achieve higher resolution at the cost of increased power consumption. The choice of ADC influences the required IA gain: SAR-based readouts need higher gain to fully utilize the ADC input range, making them more susceptible to DC offsets and motion artifacts, while $\Delta\Sigma$-based readouts require lower gain, reducing offset sensitivity but increasing noise vulnerability. Throughput and latency also play a role: SAR ADCs provide low latency and can be oversampled for higher data rates, whereas $\Delta\Sigma$ ADCs trade off power and latency through oversampling ratio and digital filtering. Ultimately, the selection depends on the application's dynamic range, SNR, and power constraints.

3.0.7 Discussion

I/Q and polar demodulation are mathematically equivalent since Cartesian and polar forms are related through nonlinear transformations. However, their hardware realizations differ significantly. I/Q demodulation enables fine-grained digital post-processing and high accuracy, at the cost of power and circuit complexity. Polar demodulation, relying on envelope and phase detection, provides a simpler, more energy-efficient implementation, especially suited for ultra-low-power and area-constrained designs. When properly calibrated, polar demodulation can achieve excellent accuracy while minimizing energy consumption and silicon area.

Table 3.1: Comparison of Impedance Demodulation Techniques

Method	Circuit-Level Implementation	Advantages	Disadvantages
I/Q Demodulation	Mixers + LPFs; Real/Imag. computation	High precision; Robust to noise; Flexible digital post-processing	Higher power; Calibration required; Harmonic sensitivity
Polar Demodulation	Peak and phase detectors; comparators; rectifiers; LPFs	Low power; Compact; Direct amplitude/phase extraction	Offset and noise sensitivity; Harmonic distortion; Lower linearity
Digital Demodulation	FFT, matched filters, or timestamping	High SNR; Accurate phase estimation; Digital flexibility	Power-hungry; Limited by ADC speed; Increased complexity

3.1 A Novel Polar-Demodulator-Based Electronic Interface for Bioimpedance Spectroscopy with Enhanced Phase Detection and Reduced Dead Zone

As discussed in Section 3.0.5, polar demodulation techniques—particularly high-frequency XOR-based phase detection circuits—are prone to false commutations, which can introduce significant phase estimation errors. These errors arise from rapid state transitions and metastability phenomena, and can propagate through the circuit, producing spurious phase measurements. Furthermore, such circuits are subject to critical dead-zone and blind-zone effects, where narrow input signal ranges result in nonlinear response regions. These regions are characterized by signal ambiguity, reduced sensitivity, and potential phase-tracking discontinuities, all of which degrade the overall accuracy of phase estimation algorithms.

To address these challenges, we developed an architecture enabling precise impedance measurement up to 1 MHz. The design introduces a frequency-down technique to the polar demodulator with a reference path, halving the input frequency and applying a 90° phase shift. This reduces the demodulator's operating frequency and minimizes the XOR dead-zone. A feedback gain control ensures optimal gain for accurate magnitude comparison with the reference path. Additionally, an improved peak detector using Schottky diodes—with lower forward voltage, series resistance, and faster settling time—enhances measurement precision. This architecture notably improves accuracy at high frequencies where the dead-zone effect is significant. The combined use of frequency down-shifting and delay to reduce dead-zone in polar demodulation is demonstrated here for the first time [**Paper VII**].

3.1.1 System Architecture

Fig. 3.8 shows an overall block diagram of the proposed impedance-measurement mixed-signal electronic interface. The architecture is based on an operational amplifier (THS4631) in inverting configuration with an input resistance, R_{in}, that can be selected from a bank of resistors controlled by a multiplexer. This selection mechanism helps keep the amplifier gain within specified limits. Symmetrically, a reference path has been implemented to provide a reference signal essential for calculating both magnitude and phase. After the inverting stage, an instrumentation amplifier (INA849) stage has been implemented, characterized by a bandwidth of 10 MHz with a fixed gain of 14 dB. Subsequently, the signal processing splits into two distinct yet complementary paths. The magnitude value of the impedance (Z_m) is obtained through a peak detector circuit by comparing the output with the reference signal, while the phase shift of Z_m is extracted using two zero-crossing comparators (LT1715), an XOR gate (SN74LVC1G86), and a low-pass filter (LPF). The

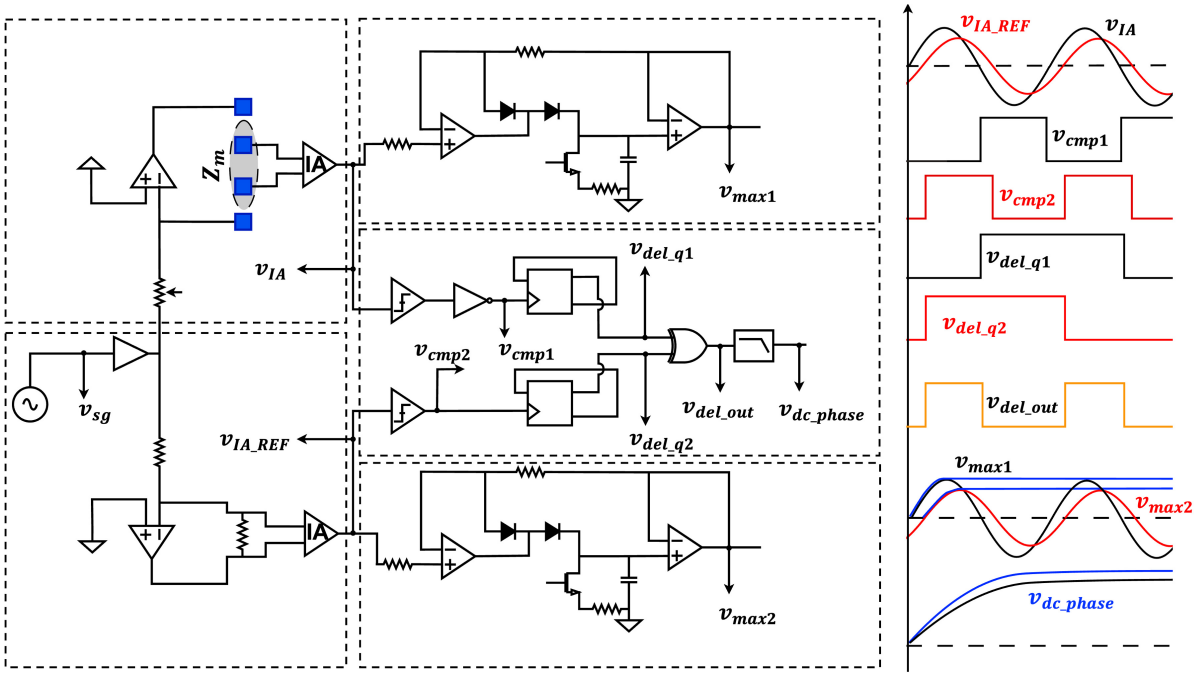

Figure 3.8: Schematic diagram of the proposed impedance-measurement circuit topology.

output signals are quasi-DC voltages that represent both the magnitude and phase of Z_m, enabling comprehensive impedance characterization.

Magnitude-Measurement Path

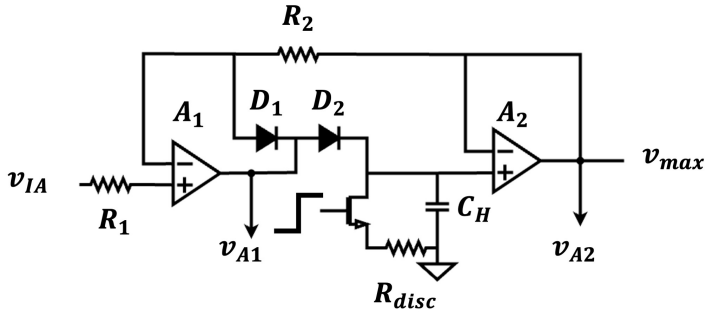

Figure 3.9: Proposed peak detector circuit.

In order to extract the IA output amplitude, a Peak Detector Circuit (PDC) locks to the maximum value of v_{IA}, Fig. 3.9. The dual op-amp configuration offers significant technical improvements in peak detection performance. The voltage follower configuration of A_2 presents an extremely high input impedance and near-zero output impedance, effectively isolating the holding capacitor, C_H, of 0.1 μF from load variations. This isolation prevents capacitor discharge through load currents, maintaining peak voltage accuracy. The fast recovery diode D_2 clamps A_1's output, preventing negative saturation and reducing recovery time when transitioning to a new peak value. The matched input resistors R_1 and R_2, both with a value of 10 kΩ, create a balanced input bias current path, minimizing

input offset voltage effects and improving DC accuracy. Furthermore, A_1's high open-loop gain ensures precise voltage following during peak detection, while its high slew rate capability, combined with the diode's fast switching characteristics, enables accurate tracking of rapid input voltage changes. The charging and discharging of the hold capacitor can be controlled by driving the gate of an nmos transistor, which allows the voltage across the capacitor to be discharged through the discharge resistor R_{disc}. The magnitude of the impedance can be directly computed from the output values of the PDC, as expressed by the following mathematical relationship in (3.17):

$$mag = \frac{v_{max1}}{v_{max2}} G_2 R_{set} \tag{3.17}$$

where :

- v_{max1} and v_{max2} are the output of the implemented PDC
- G_2 indicates the gain of the reference path
- R_{set} corresponds to the resistor selected for the impedance-measurement path

Phase-Measurement Path

When the phase difference, between the two inspected sine waves is close to zero, the classic exclusive-OR phase detector generates a very narrow pulse proportional to the phase shift as shown in Fig. 3.10.

Typically, at high frequency above 100 kHz, where the delay each stadium is significant this pulse is warp leading to errors in phase estimation. This results in a loss of linearity in the detector's response, especially near zero phase difference, where the output fails to reflect small variations accurately.

For this reason, in the proposed circuit, Fig. 3.11, we aimed to reduce this error. In fact, after the comparator converts X e Y, respectively the output of the inverting amplifier and the reference path, into square-wave signals a frequency divider for two distinct signals is implemented using two D flip-flops (SN74HC74), which are CMOS-based edge-triggered devices.

For the first signal, the flip-flop is configured in toggle mode by connecting its $\overline{Q}$ output to its D input. For the second signal, an inverter is placed before the input to the second flip-flop, resulting in both frequency division by 2 and a quadrature (90°) phase shift between the two output signals. This quadrature arrangement is particularly valuable when the divided signals feed into an XOR phase detector in subsequent stages. The 90° phase relationship effectively eliminates the dead zone problem commonly encountered in XOR phase detectors. The dead zone occurs when the phase difference between input signals approaches 0 or 180°, causing the XOR output to remain static for small phase

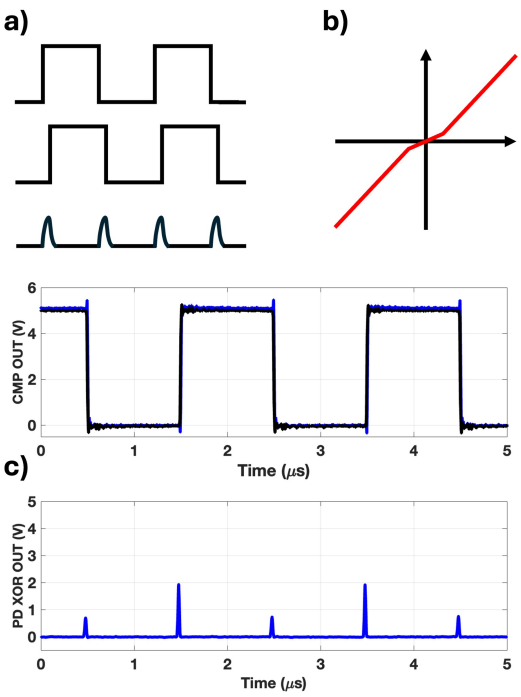

Figure 3.10: XOR gate analysis in the presence of dead zone: (a) Theoretical representation of square wave input signals highlighting false switching events caused by dead zone effect; (b) Theoretical XOR gate response characterization with emphasis on the dead zone region near zero; (c) Experimental measurement of the XOR output with a 1° phase shift between input signals at 500 kHz operating frequency.

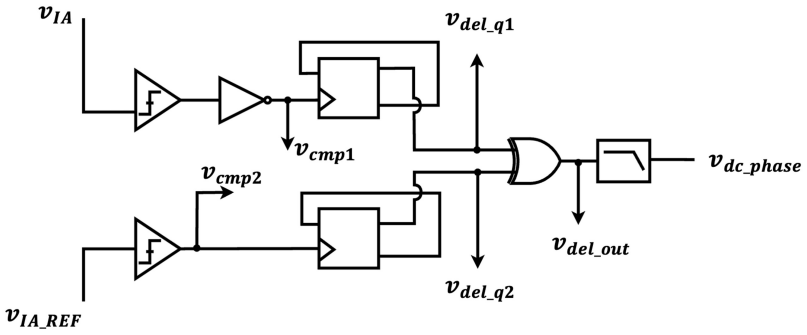

Figure 3.11: Proposed phase detection circuit.

variations and reducing detector sensitivity. By ensuring quadrature signals, the phase detector always operates in its linear region with maximum sensitivity.

These two signal are the input of a exclusive OR-phase detector and the output duty cycle ratio corresponds to a phase difference between Z_m and the reference path, as shown in the timing diagram in Fig. 3.12. When the Z_m and R_{ref} measurement path exhibit identical characteristics, the propagation delays in both pathways are equal, leading to cancellation of phase errors. Then, the following low-pass filter, LPF, with a cut-off frequency of 0.15 Hz act as a time-to-voltage converter and extract the averages of $v_{del\_out}(t)$

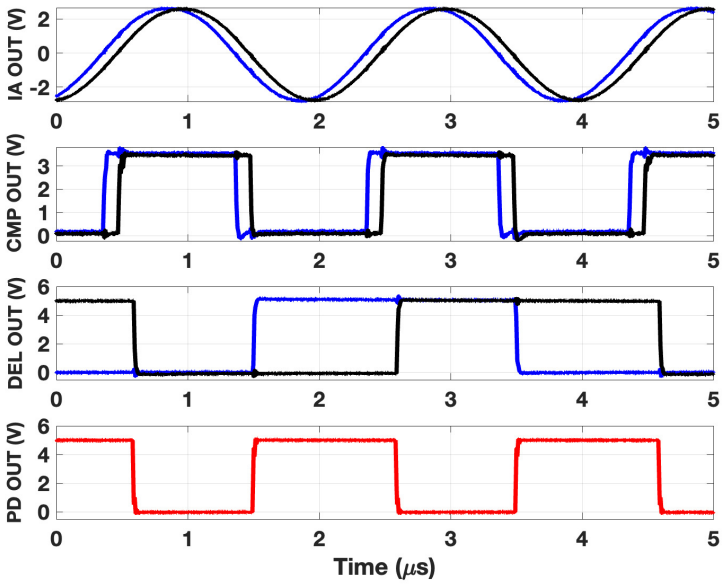

Figure 3.12: Timing diagram illustrating the stages of the modified XOR phase detector (PD): (a) Output signal from the IA with a 20° phase shift; (b) Comparator output converting IA output into square waves; (c) Frequency divider output with 90° phase shift; (d) XOR phase detector output signal before time-to-voltage conversion.

out to a DC value, v_{dc_phase}. The simulation made with LTSpice reports a sensitivity of 10 mV/deg, theoretically ensuring phase detection capability down to 0.1° of phase difference. This high-resolution phase detection capability significantly enhances the precision of phase measurement systems and control loops. This circuit addresses the well-known measurement ambiguity issue inherent in exclusive OR phase detectors where phase shifts of opposite signs produce identical output voltage values.

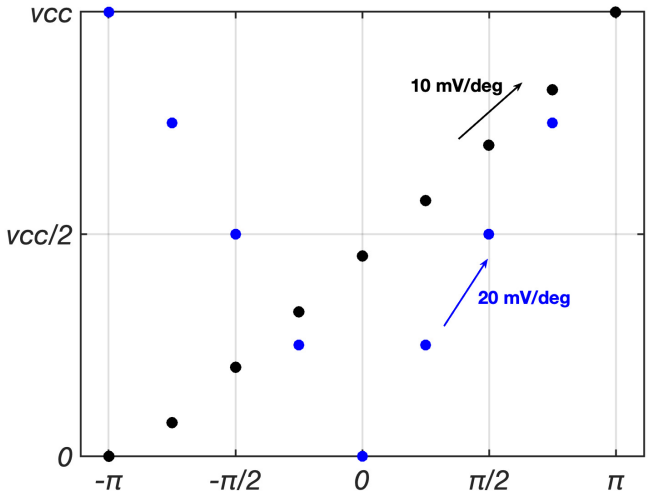

Figure 3.13: Simulated output slope comparison between conventional XOR phase detector (blue dots) and modified XOR phase detector (black dots), demonstrating the reduction of the dead zone and the elimination of phase detection ambiguity present in the conventional XOR design.

Through this implementation, the combination of phase shift and frequency divider mechanisms effectively repositions the zero-phase point ideally to the midpoint of the supply voltage, albeit with a consequent halving of the phase detector's sensitivity. Specifically, this approach enables the maintenance of a high sensitivity, 10 mV/degree, equivalent to half that of the standalone XOR detector, while simultaneously addressing the critical issue of measurement ambiguity, as shown in Fig. 3.13.

The design overcomes the inherent constraints of conventional XOR-based phase detection through an enhanced phase comparison methodology that delivers superior measurement precision and eliminates ambiguities present in standard XOR configurations, Fig. **??**(c). The phase shift of the impedance can be directly computed from the output value of the proposed phase detector architecture, as expressed by the following mathematical relationship in (3.18):

$$\phi = (v_{dc\_phase} - v_b)/v_{slope} \tag{3.18}$$

where :

- v_{slope} represents the angular coefficient of the calibration curve
- v_{dc_phase} indicates the output voltage of the phase detector
- v_b corresponds to the voltage value measured at 0°

Feedback Loop

The automatic gain control was implemented through a microcontroller (MCU), Atmel SAM3X8E, that enables precise control over the system through I2C communication with an external ADS1115 analog-to-digital converter(ADC). This 16-bit $\Sigma\Delta$ ADC offers a resolution (0.1875 mV per bit at ±6.144 V range) and sensitivity with a programmable gain amplifier providing up to 16x amplification for low-level signals. The MCU continuously monitors the DC signals produced at the output of the low-pass filter (LPF), which constitutes the final stage of the phase detection circuit, and dynamically adjusts the impedance ratio of the inverting amplifier in real time by controlling the multiplexers. This adaptive feedback mechanism ensures optimal performance across varying operating conditions, compensating for component drift and environmental variations while mantaining phase accuracy within the target specifications. Additionally, in the developed firmware are implemented the equations for the calculation of the real-time value of modulus and phase.

To further enhance the robustness of the feedback mechanism and correct residual nonlinearities or high-frequency phase jitter, future iterations of the system could integrate AI-based compensation schemes. In particular, adaptive neural network models such as LSTM (Long Short-Term Memory) and U-Net architectures could be trained to monitor electrical absorption dynamics across the sensor array and learn complex spatiotemporal

patterns enabling real-time prediction and correction of phase and magnitude distortions under varying physiological and environmental conditions [50].

Noise Analysis

Fig. 3.14 shows the input-referred noise spectral density (in $\mathrm{nV}/\sqrt{\mathrm{Hz}}$) for both the peak detector (PDC) and the phase detector. Integration over the 100 Hz–1 MHz range yields V_{rms} values of 1.01 mV (PDC) and 0.98 mV (phase detector), clearly indicating the dominant contributions from thermal noise, flicker noise ($1/f$), and shot noise.

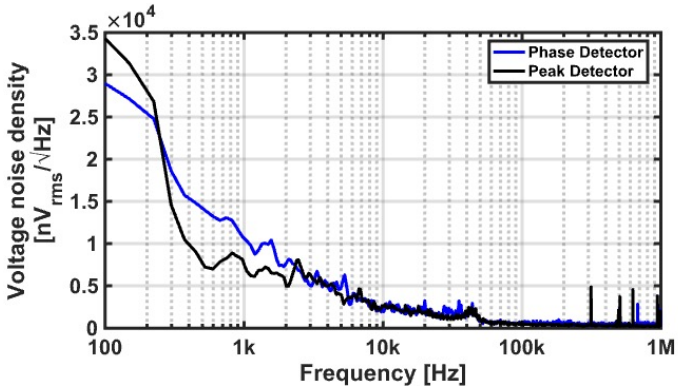

Figure 3.14: Measured input-referred noise voltage density of the peak and phase detectors under nominal operating conditions.

From this analysis, the system exhibits a signal-to-noise ratio (SNR) of 29.98 dB and a dynamic range (DR) of 59.9 dB. To relax the effective DR requirement, a dynamic gain adjustment is implemented in the inverting amplifier stage: by reconfiguring the feedback network, the gain can be varied by approximately 14 dB, keeping the output amplitude nearly constant across a wide range of input impedances. This adaptive strategy minimizes noise impact and prevents saturation, thereby ensuring robust measurement performance while simplifying the hardware design.

For comparison, previously reported systems relying on pseudo-sinusoidal [51, 52] or square excitation waveforms [53, 54] typically achieve SNR values in the range of 45–76 dB and dynamic ranges of 90–105 dB, depending on the acquisition chain architecture. Although the present implementation shows lower absolute SNR and DR, the adaptive gain strategy compensates for these limitations and provides a practical advantage in handling variable tissue impedance conditions. This trade-off highlights that circuit-level adaptability can be more impactful for robust bio-impedance measurement than maximizing absolute SNR or DR figures.

3.1.2 Results and Discussions

Measurement results

For the evaluation of the circuit performances, a 4-layer PCB was designed, as shown in Fig. 3.15, and powered with a $\pm 5\,\mathrm{V}$ dual supply.

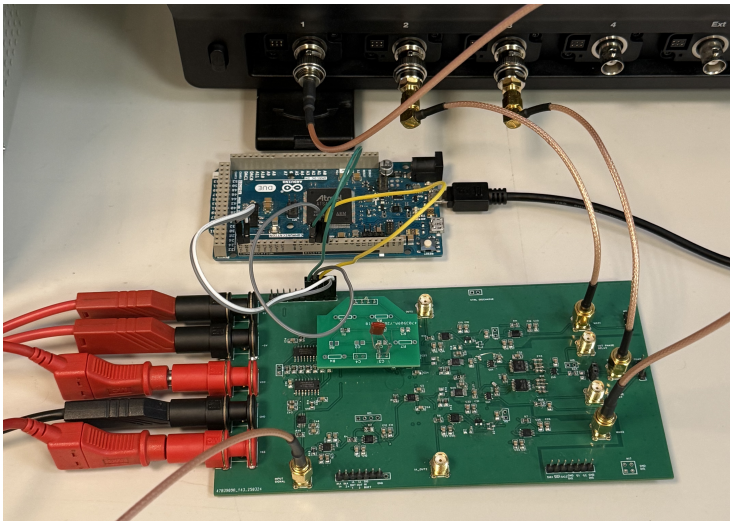

Figure 3.15: Picture of the experimental setup featuring the designed PCB implementing the proposed polar demodulation architecture. The setup includes analog front-end circuitry, a reference path for magnitude and phase extraction, and interfacing points for external signal sources and measurement equipment.

The circuit was tested using bench instruments from Teledyne LeCroy, including a T3PS33203P power supply, a T3AFG30 waveform generator, and an HDO6054 bench oscilloscope. The proposed PCB consumes 800 mW of power over the entire frequency range. Output values from the peak detectors and the phase detector were acquired by a microcontroller for further processing and analysis.

A phase calibration was performed for each frequency of interest to verify the theoretical sensitivity of the PDC and to determine the reference voltage at 0°, v_b, used in the phase calculation. The calibration consisted in measuring the output voltage corresponding to a zero phase difference between the two input sinusoids. Experimental tests were conducted using multiple discrete model cells, Z_m, illustrated in Fig. 3.16, Fig. 3.17 and Fig. 3.18 to evaluate the efficacy of the proposed architecture for impedance spectroscopy.

The first model cell, shown Fig. 3.16, consisted of a parallel combination of a 6.8 kΩ resistor and a 2 nF capacitor, connected in series with a 330 Ω resistor [55].

The measurement protocol employed a 100 mV_{pp} sinusoidal excitation signal, v_{sg}, was applied, sweeping frequencies from 10 Hz to 1 MHz. The results for magnitude and phase responses are shown in Fig. 3.16, along with the theoretical transfer function for comparison. Additionally, two other impedance models—a breast cancer cells model [56] and a biceps Cole-Cole impedance model [57]—were also evaluated, with their results presented in Fig. 3.17 and Fig. 3.18, respectively.

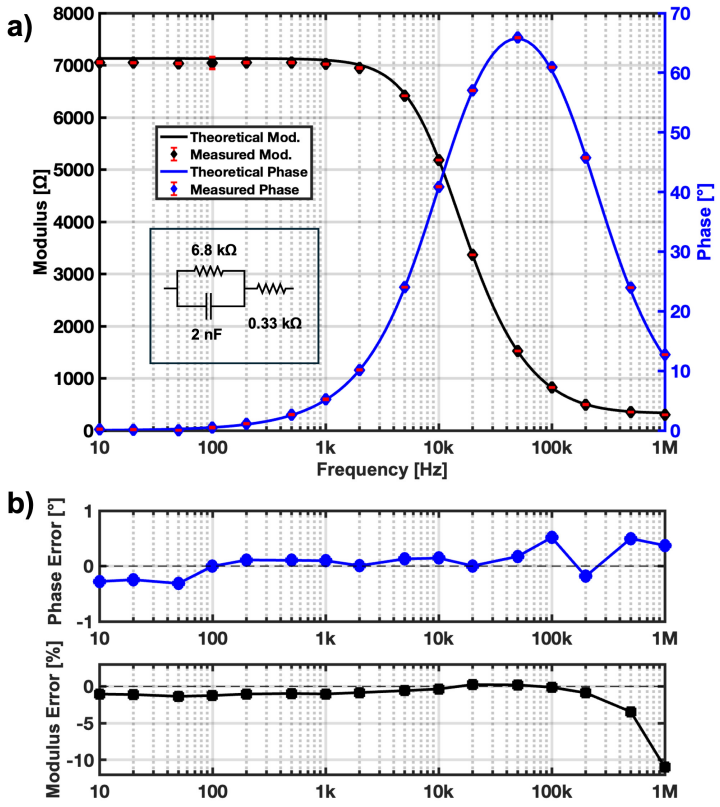

Figure 3.16: a) Comparative analysis of measured impedance modulus and phase for the first model cell: Experimental results (N=3 independent experiments) plotted against the theoretical transfer function across the 10 Hz - 1 MHz frequency range. Data presented as mean ± SD); b) Error characterization across the frequency spectrum: phase error in degrees and magnitude error in percentage for individual frequency points.

The experimental results obtained through the proposed circuit demonstrate remarkable concordance with the theoretical values derived from the Z_m transfer function.

Fig. 3.16 b), Fig. 3.17 b) and Fig. 3.18 b) also depicts the measurement error analysis of the results shown in Fig. 3.16 a), Fig. 3.17 a) and Fig. 3.18 a).

The maximum observed magnitude deviation of 11% occurs at the upper frequency boundary of 1 MHz, where the theoretical impedance approximates 338 Ω, resulting in an absolute estimation error of approximately 37 Ω. This error is primarily attributed to non-idealities in the peak detector, which can introduce inaccuracies in capturing the true amplitude of the high-frequency sinusoidal signals due to limited bandwidth and response time. To mitigate high-frequency amplitude errors, strategies such as extending the detector bandwidth, employing faster operational amplifiers with higher slew rates, and implementing frequency-dependent calibration routines are proposed.

To evaluate the safety of the proposed system, the specific absorption rate (SAR) and the associated thermal effects were estimated using a tissue-equivalent load model. This simplified approach considers the power delivered to the load and the thermal properties of the exposed tissue, without relying on a full 3D anatomical simulation. For SAR

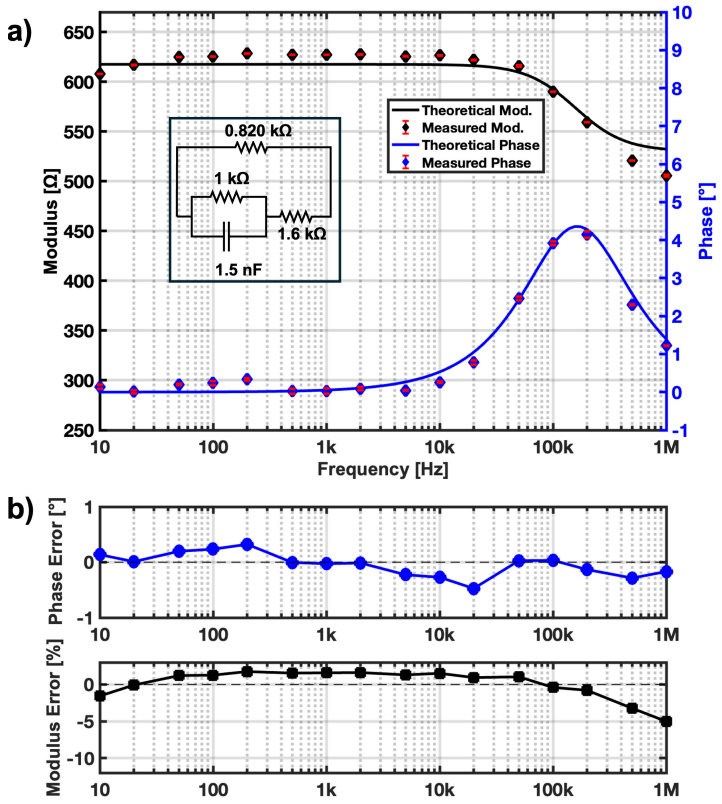

Figure 3.17: a) Comparative analysis of measured impedance modulus and phase for a breast cancer cells model: Experimental results (N=3 independent experiments) plotted against the theoretical transfer function across the 10 Hz – 1 MHz frequency range. Data presented as mean± SD. (b) Error characterization across the frequency spectrum: phase error in degrees and magnitude error in percentage for individual frequency points.

estimation, the relevant high-frequency impedance of muscle tissue is used, here assumed as $Z = 560\ \Omega$, which corresponds to the effective impedance of biceps muscle at the frequencies of interest [57]. In addition, the absorbed energy is normalized to a small representative tissue mass of $m = 1$ g, modeling a localized volume of muscle exposed to the applied field.

The key parameters are:

- Applied peak-to-peak voltage: $V_{\text{pp}} = 100$ mV
- Tissue-equivalent impedance: $Z = 560\ \Omega$
- Equivalent tissue mass: $m = 1\text{ g} = 0.001$ kg
- Tissue heat capacity: $C = 3000$ J/(kg·K) [58]

The RMS voltage is:

$$V_{\text{RMS}} = \frac{V_{\text{pp}}}{2\sqrt{2}} = \frac{0.1}{2\sqrt{2}} \approx 0.0354\text{ V} \tag{3.19}$$

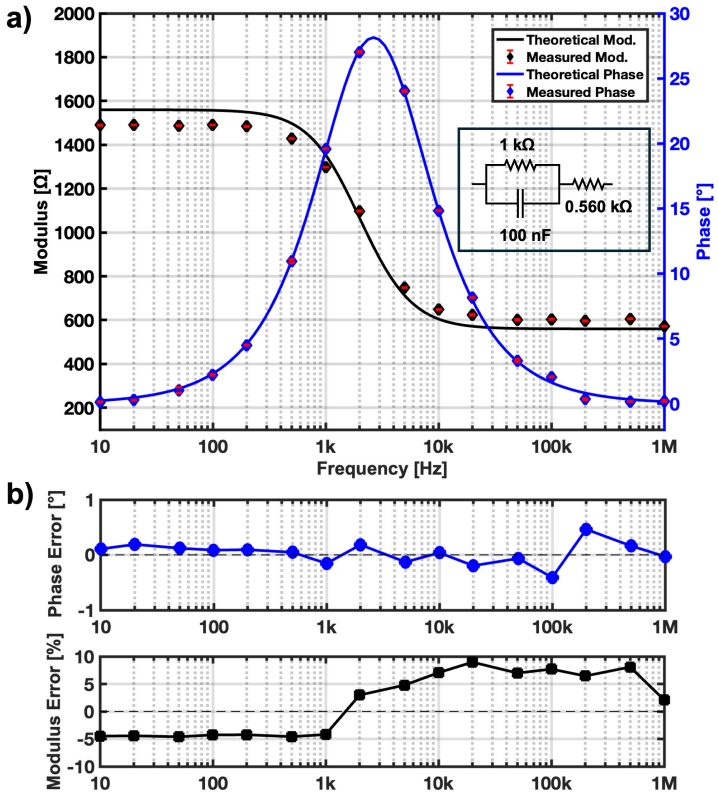

Figure 3.18: a) Comparative analysis of measured impedance modulus and phase for a Cole-Cole model of biceps tissue: Experimental results (N=3 independent experiments) plotted against the theoretical transfer function across the 10 Hz – 1 MHz frequency range. Data presented as mean ± SD. (b) Error characterization across the frequency spectrum: phase error in degrees and magnitude error in percentage for individual frequency points.

The RMS current through the tissue-equivalent load is:

$$I_{\text{RMS}} = \frac{V_{\text{RMS}}}{Z} = \frac{0.0354}{560} \approx 6.32 \times 10^{-5} \text{ A} \tag{3.20}$$

The power dissipated in the load is:

$$P = I_{\text{RMS}}^2 \cdot R = (6.32 \times 10^{-5})^2 \cdot 560 \approx 2.24 \times 10^{-6} \text{ W} \tag{3.21}$$

The SAR, normalized to the assumed tissue mass, is:

$$\text{SAR} = \frac{P}{m} = \frac{2.24 \times 10^{-6}}{0.001} \approx 2.24 \times 10^{-3} \text{ W/kg} \tag{3.22}$$

Finally, the rate of temperature increase is:

$$\frac{dT}{dt} = \frac{\text{SAR}}{C} = \frac{2.24 \times 10^{-3}}{3000} \approx 7.47 \times 10^{-7} \text{ K/s} \tag{3.23}$$

These results indicate that the absorbed power is several orders of magnitude below

the safety limits defined by ICNIRP [59] and IEEE C95.1-2019 [60], which prescribe a maximum localized SAR of 2 W/kg averaged over 10 g of tissue. Although this estimate does not rely on a full 3D anatomical model, it provides a conservative evaluation of exposure conditions and confirms that the device operates safely within accepted biomedical limits. Table 3.2 presents a comparative analysis with state-of-the-art implementations, highlighting the advantages of our novel phase detection topology based on XOR gates with sensitivity of 10 mV/deg. This approach enables an expanded input frequency range coupled with enhanced dynamic range for impedance-based measurement applications.

Table 3.2: Performance summary and comparison with state-of-the-art works

	Method	Frequency Range [Hz]	Magnitude Error [%]	Phase Error [°]
This work	Polar	10–1M	11	0.51
[52]	I/Q	10k–10M	*	<4.32
[61]	I/Q	50–1M	<4	*
[62]	Polar	100–100k	<3.5	<3.6
[55]	Polar	100–10M	<2.5	<2.2
[63]	Polar	100–10M	1.1	1.9
[64]	Polar	1–2M	1[1]	1.3[1]
[65]	T-D	10k–500k	<2.94	<1
[66]	Polar	10–1M	0.3	2.1[1]

[1] Simulation results
* Not reported

3.2 AD8302-based Polar Demodulator Interface for Impedance Spectroscopy oriented to Biomedical Applications

Remaining within the context of polar architectures, recent research has focused on developing precise, broadband impedance measurement systems, both through custom-designed integrated circuits (ICs) and using commercial components such as the AD5933 [67, 68, 69], AD9850 [70, 71], and AD8302 [72, 73, 74] with specialized interfacing. However, impedance characterization with these ICs is typically limited to around 100 kHz due to the slew-rate and bandwidth limitations of the operational amplifiers. These constraints highlight the need for alternative polar architectures and measurement strategies capable of extending the frequency range, improving accuracy, and enabling faster, more flexible impedance measurements.

To overcome these limitations, we present an architecture based on the AD8302, enabling impedance measurements up to 10 MHz with excellent precision. The proposed design includes an analog front-end with high-slew-rate operational amplifiers, a high-bandwidth IA, and a feedback gain control to optimize performance across lower frequency ranges [**Paper IX**]. The AD8302 comprises a matched pair of demodulating logarithmic amplifiers, each with a 60 dB measurement range; the difference of their outputs provides a measurement of the modulus ratio. A multiplier-type phase detector ensures precise phase balance, driven by the fully limited signals from the logarithmic amplifiers' outputs.

3.2.1 System architecture

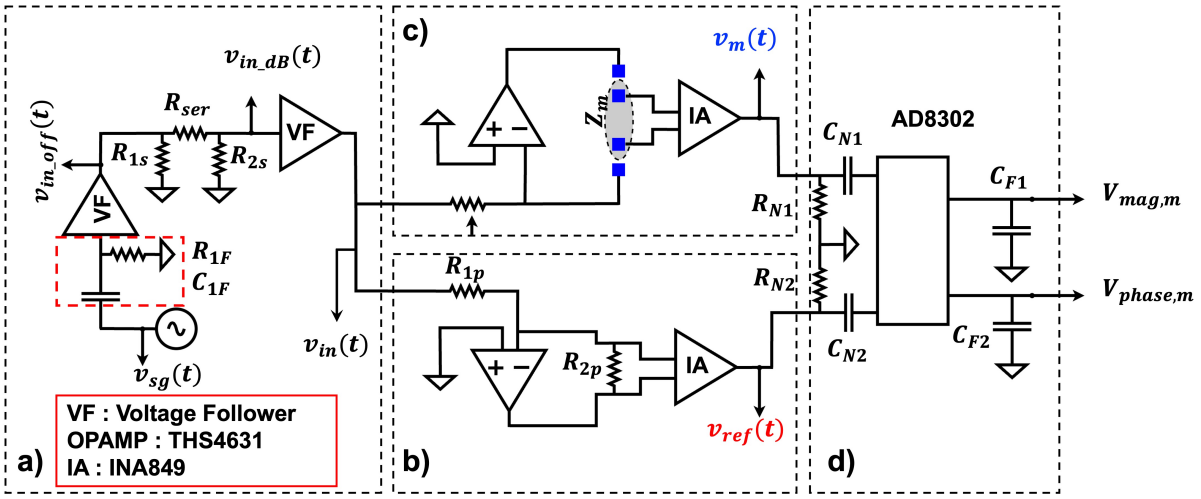

Figure 3.19: Simplified block diagram presenting the architecture of the proposed impedance-measurement circuit.

Fig. 3.19 shows a schematic diagram of the proposed polar demodulator. A signal gen-

erator is used to provide the input signal for the measurement of the unknown impedance, Z_m. As reported is Fig. 3.19(a), before being applied to the measurement circuit, the input signal, $v_{in}(t)$, is first conditioned through a first-order high-pass filter (HPF), implemented as a CR ($R_{1F} = 1$ MΩ and $C_{1F} = 1$ μF) network followed by a voltage follower (VF), with a cut-off frequency of 0.16 Hz in order to remove the DC offset from the input signal, $v_{in}(t)$. After this stage an attenuation network of -16 dB (R_{1s} and $R_{2s} = 68$ Ω; $R_{ser} = 150$ Ω) is implemented to the input signal before the inverting stage.

For the analysis of Z_m, a 100 mV peak-to-peak signal is applied to two paths: a reference stage with fixed gain $G_p \approx R_{2p}/R_{1p} \approx 4.7$ (where $R_{2p} = 4.7\,\mathrm{k\Omega}$ and $R_{1p} = 1\,\mathrm{k\Omega}$) and the measurement stage.

The reference stage is designed to compensate for the 90° phase shift introduced by the op-amp configuration and to synchronize the two signals.

The measurement stage employs an inverting configuration using a wideband FET-input op-amp (THS4631) in a dynamic gain configuration, implemented with a resistor bank controlled by two multiplexers. This ensures a gain ratio below +20 dB, thereby guaranteeing the maximum achievable bandwidth (GBW) of the amplifier for the selected configuration.

Two ultra-low-noise instrumentation amplifiers (INA849) with 0 dB gain amplify $v_{\mathrm{ref}}(t)$ along the reference path and $v_m(t)$ along the measurement path. This setup decouples the current path from the voltage measurement path, allowing both 2-electrode and 4-electrode configurations.

Once the signal has been extracted from the instrumentation amplifier (IA), is applied to the input of the AD8302. The AD8302 is a commercial IC, originally designed for RF/IF gain and phase detection up to 1 GHz. The IC exhibits a mean sensitivity of 30 mV/dB for the modulus and 10 mV/degree for the phase. Since the linearity range is approximately ±30 dB for the modulus and between 0 and 180° for the phase, the bank of resistor is dimensioned in order to mantain a ratio less than +20 dB for the impedance range from 100-1 MΩ. In order to use this IC at low frequency the input stage network is dimensioned to impedance matching (R_{N1} and $R_{N1} = 50$ Ω) and move the nominal high-pass corner frequency, fHP, of this loop that is set internally at 200 MHz but it's lowered by adding external capacitance to the input stage network. In this case, external capacitances C_{N1} and C_{N2}, each equal to 100 μF, are added to set the high-pass corner frequency, f_{HP}, at 31 Hz.

In the IC, each log amp consists of a cascade of six 10 dB gain stages with seven associated detectors. The individual gain stages have 3 dB bandwidths in excess of 5 GHz. The signal path is fully differential to minimize the effect of common-mode signals and noise. Since there is a total of 60 dB of cascaded gain, slight dc offsets can cause limiting of the latter stages, which may cause measurement errors for small signals. In order to test the architecture, the designed circuit is implemented in a 4-layer PCB with thermal dissipa-

tion with a dual-supply of ±5V. The analog front-end incorporates a signal conditioning architecture for DC offset elimination the input signal, followed by an attenuation stage of 16 dB. The low-impedance signal is then distributed across two critical signal paths: a fixed-gain inverting operational amplifier configuration generating a reference signal as reported in Fig. 3.19(b), while a dynamic operational amplifier configuration adapts to the unknown impedance under test, Fig. 3.19(c). The processed signals are subsequently applied to the input of INA849 high-bandwidth, ultra-low noise instrumentation amplifier, to ensures signal integrity and decouple the current path to the measured voltage path. In the final stage, the conditioned reference and test signals are simultaneously applied to the AD8302, Fig. 3.19(d), for comprehensive signal analysis.

The fundamental logic behind the dynamic gain control of the inverting amplifier focuses on precisely managing the ratio between the reference resistance R_{set} and Z_m across the entire frequency spectrum, an approach already used in one of our previous works [75]. This strategic approach aims to maintain the circuit's operation within the linear range while simultaneously expanding the measurable impedance spectrum. By dynamically adapting the gain, the circuit can mitigate significant performance limitations that arise from substantial impedance mismatches. Substantial differences between R_{set} and Z_m can lead to bandwidth reduction, resulting in signal attenuation and consequent estimation errors of the device's impedance characteristics. To address these challenges, a feedback gain control mechanism is implemented through a dynamically configurable resistance bank. This bank is selectively switched via a multiplexer, which is controlled by a microcontroller (μC). The μC's primary function is to optimize R_{set} selection for the unknown impedance, while maintaining a critical constraint of keeping the ratio between reference voltage $v_{ref}(t)$ and measurement voltage $v_z(t)$ below 20 dB while sampling the signal an analog-to-digital converter (ADS1115). By continuously monitoring the ratio variations between these two signals, the system can adaptively and opportunistically select the most appropriate R_{set} to ensure optimal measurement accuracy and linearity across varying impedance conditions.

The AD8302 takes the difference in the output of two identical log amps, each driven by signals of similar waveforms but at different levels. Since subtraction in the logarithmic domain corresponds to a ratio in the linear domain, the resulting output becomes:

$$V_{MAG} = V_{SLP}(V_{INA}/V_{INB}) \tag{3.24}$$

$$mag(\text{dB}) = \log_{10}\left(\frac{V_{\text{INPA}}}{V_{\text{INPB}}}\right) = \frac{V_{\text{MAG}} - V_{0\text{dB}}}{30\ \text{mV}} \tag{3.25}$$

where V_{INA} and V_{INB} are the input voltages, V_{MAG} is the output corresponding to the modulus of the signal level difference, and V_{SLP} is the slope of 30 mV/dB.

The log amplifier architecture comprises cascaded linear and limiting gain stages with

demodulating detectors. The output of the final stage in each log amp is a fully amplitude-limited sinusoidal signal over the majority of the input dynamic range, preserving phase information. These conditioned signals are subsequently applied to an analog vector (multiplicative) phase detector, which performs a continuous-time multiplication of the two inputs. After low-pass filtering (C_{F1},C_{F2} = 10 μF), the detector generates a DC voltage proportional to the cosine of the phase difference between the inputs, rendering the measured phase independent of input signal amplitudes and providing a linear response over a defined central phase range. The phase output has the general form:

$$V_{PHASE} = V_{\phi}(\phi V_{INA} - \phi V_{INB}) \tag{3.26}$$

$$\theta(\text{degree}) = [\theta_{INPA} - \theta_{INPB}] = \frac{V_{0^\circ} - V_{\text{PHASE}}}{10 \text{ mV}} \tag{3.27}$$

where V_{ϕ} is the phase slope of 10 mV/degree and ϕ is each signal's relative phase in degrees. To ensure accurate phase estimation across the entire frequency sweep, reference voltages corresponding to 0° phase (V_{0°) were experimentally acquired for each test frequency and used in the calculation.

3.2.2 Noise Analysis

Fig. 3.20 presents the input-referred noise spectral density, expressed in nV/$\sqrt{\text{Hz}}$, for the output of the logaritmic amplifier. Integrating the spectra over the 100 Hz–10 MHz band, the resulting $V_{mag,noise}$ and $V_{phase,noise}$ are respectively 1.08 mV and 1.11 mV. These results indicate that thermal noise, flicker noise ($1/f$), and shot noise represent the main limiting factors.

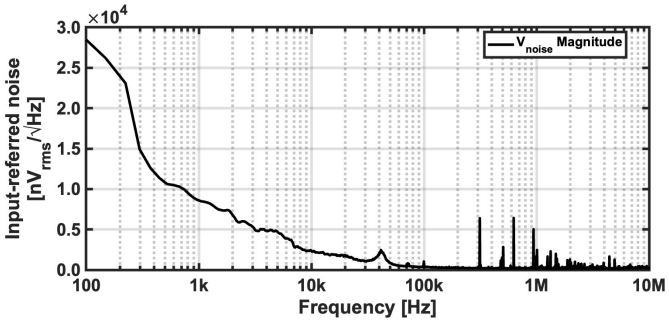

Figure 3.20: Input-referred voltage noise spectra for the output $V_{mag,m}$ under nominal operating conditions.

The SNR calculated at the analog front-end preceding the AD8302 reaches a maximum of 31.1 dB, in agreement with expectations for a wideband INA–op-amp stage. Measured SNR varies from 25 to 31 dB across the investigated frequency range, peaking around 1

kHz. The SNR reduction at low frequencies is consistent with flicker noise contributions, while degradation at higher frequencies is primarily due to broadband noise integration.

The following AD8302 phase and gain detector exhibits a dynamic range of 58 dB for magnitude and 46.3 dB for phase, enabling accurate measurement of amplitude and phase variations over a wide range. Overall, the observed SNR and dynamic range behavior aligns with the expected performance of a wideband INA–op-amp front-end.

3.2.3 Results and Discussion

To evaluate the IC performance, experimental bench tests were conducted to assess the estimation accuracy of modulus and phase. A 4-layer PCB was designed, as shown in Fig. 3.21, and powered with a $\pm 5\,\mathrm{V}$ dual supply. However, the board layout and components are also designed to support a $\pm 12\,\mathrm{V}$ supply, allowing higher output compliance when needed.

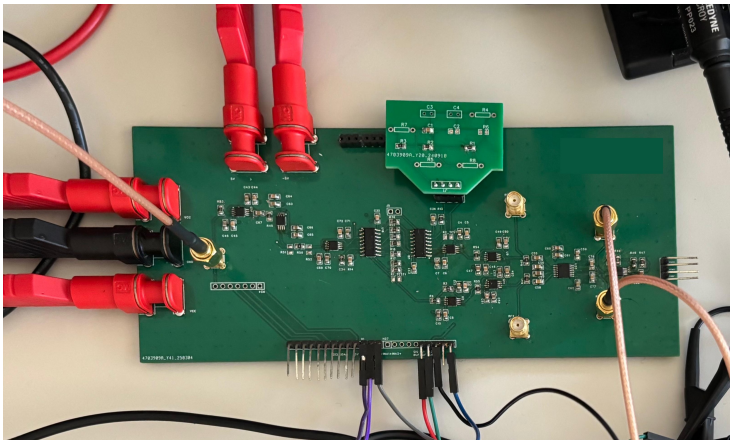

Figure 3.21: Picture of the experimental setup featuring the designed PCB implementing the proposed polar demodulation architecture. The setup includes analog front-end circuitry and interfacing points for external signal sources and measurement equipment.

The circuit was tested using bench instruments from Teledyne LeCroy, including a T3PS33203P power supply, a T3AFG30 waveform generator, and an HDO6054 bench oscilloscope. The proposed PCB consumes 500 mW of power over the entire frequency range, while output values from the peak detectors and the phase detector were acquired by a microcontroller for further processing and analysis.

The initial validation involved evaluating the electronic interface of the AD8302 through signals with known phase shifts and attenuations in dB, as shown in Fig. 3.22(a) and in Fig. 3.22(b). As depicted in Fig. 3.22(a), the output voltage V_{phase} characteristics were analyzed across a phase shift range of $\pm 180°$, including a detailed measurement error analysis. Complementarily, Fig. 3.22(b) presents the V_{mag} voltage variation in relation to the decibel attenuation between inspected signals, along with the corresponding error evaluation.

The experimental results corroborate the manufacturer's datasheet specifications, revealing a linear estimation range for modulus between ±20 dB and a phase measurement error confined within acceptable tolerances.

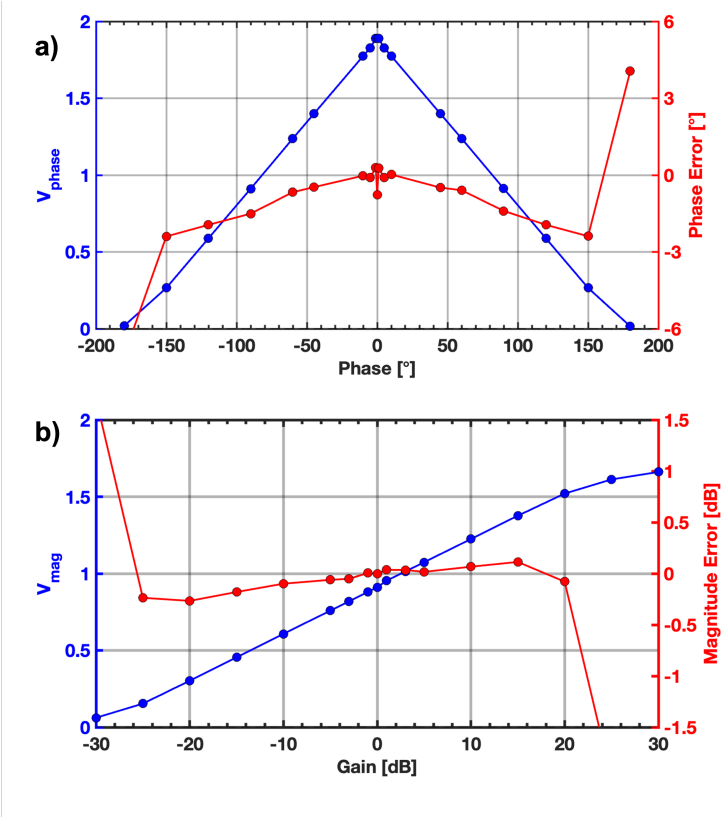

Figure 3.22: a) Phase voltage (V_{phase}) output at various phase shift values (blue dots), with corresponding phase estimation error reported in degrees (red dots); b) modulus voltage (V_{mag}) output across different decibel levels (blue dots), with corresponding modulus estimation error reported in dB (red dots)

The tests conducted involved using a signal generator for the input signal, while an ADC was incorporated into the circuit PCB for reading the output signal. The tests were carried out through three independent experiments, and the standard deviation is reported in Fig. 3.23. The test impedance, shown in Fig. 3.23(a), was used to evaluate the electronic interface through a load characterized by a high phase shift and a reduction of the impedance modulus.

A phase calibration was performed at each frequency point to verify the theoretical response of the phase detector and to establish the zero-phase reference voltage, V_{0°, used in subsequent phase calculations. For this calibration, both input channels were driven with sinusoids of identical amplitude and frequency, aligned in phase (i.e., 0° phase difference). The output voltage of the phase detector under these conditions was recorded as V_{0°. This reference value compensates for any offset in the detector and ensures that phase measurements remain accurate across the entire frequency sweep.

Since the electrode–tissue interface can significantly affect bioimpedance measurements–

especially when dry electrodes are used—its contribution was also evaluated by inserting an electrode contact model in series with each Z_m [76]. Measurements were therefore repeated both with and without the electrode impedance to quantify its effect on the reconstructed modulus and phase.

The electrode model was derived from the characterization reported in [77], where the electrode–skin interface is described as a series resistance followed by a parallel combination of a charge-transfer resistance and a double-layer capacitance. Accordingly, the electrode impedance used in this work was modeled as

$$Z_{\mathrm{el}}(\omega) = R_{\mathrm{s}} + \left(R_{\mathrm{ct}} \parallel \frac{1}{j\omega C_{\mathrm{dl}}} \right) \tag{3.28}$$

with

$$R_{\mathrm{s}} = 680\ \Omega, \qquad R_{\mathrm{ct}} = 34\ \mathrm{k}\Omega, \qquad C_{\mathrm{dl}} = 200\ \mathrm{nF}.$$

These parameters reproduce the typical dispersive behaviour and increased low-frequency impedance of non-gelled dry electrodes, and were included to assess their influence on the overall impedance measurement.

To evaluate the performance of the proposed circuit, experimental tests were conducted using multiple discrete model cells, Z_m, as illustrated in Fig. 3.23, Fig. 3.24 and Fig. 3.25. For each model cell, measurements were performed at three frequencies per decade and compared with the theoretical transfer function of the corresponding impedance considering also the contribution of the electrode impedance Z_{el}, with a signal source applied to the input. The measured responses show excellent agreement with the theoretical predictions, confirming the capability of the proposed circuit to perform high-accuracy impedance measurements, capturing both modulus and phase (up to 60°) over a wide frequency range from 100 Hz to 10 MHz.

The first model cell, shown in Fig. 3.23(a), consisted of a parallel combination of a 6.8 kΩ resistor and a 2 nF capacitor, connected in series with a 330 Ω resistor [55].

Additionally, two further impedance models were considered—a breast cancer cell model [56] and a biceps Cole-Cole impedance model [57]—with their respective results shown in Fig. 3.24 and Fig. 3.25. The experimental results obtained with the proposed circuit exhibit remarkable agreement with the theoretical values derived from the Z_m transfer function, both in terms of modulus and phase. Fig. 3.23(b-d), Fig. 3.24(b-d), and Fig. 3.25(b-d) present the corresponding error analysis of the results shown in Fig. 3.23(a-c), Fig. 3.24(a-c), and Fig. 3.25(a-c). The maximum modulus deviation observed is 14.46%, where the theoretical impedance is approximately 1690 Ω, corresponding to an absolute estimation error of roughly 266.92 Ω. The maximum measured phase error of 5.73° with the AD8302 is consistent with its specifications, mainly arising from intrinsic nonlinearity and input mismatches. Since the detector exhibits the largest inac-

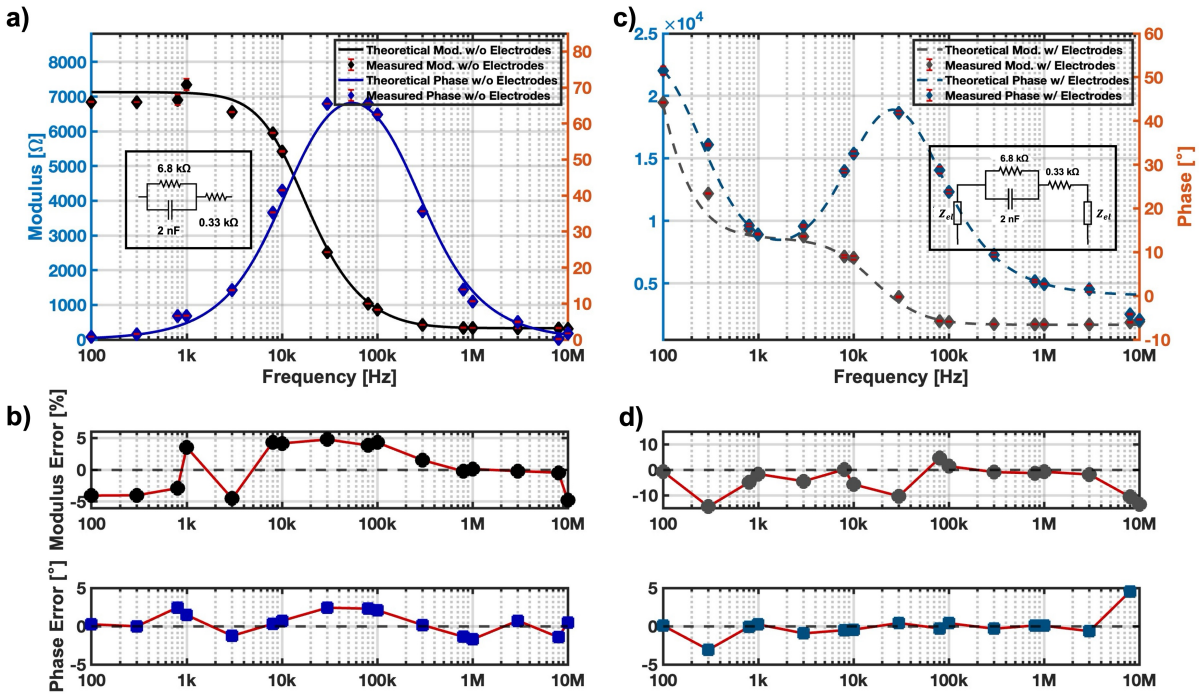

Figure 3.23: (a) Experimental and theoretical comparison of impedance modulus and phase for the first model cell over the 100 Hz–10 MHz frequency range. Data are presented as mean ± SD from three independent measurements. (b) Frequency-resolved error analysis displaying phase deviations (degrees) and modulus differences (percent) at each measured frequency. (c) Experimental and theoretical comparison of impedance modulus and phase for the first model cell including the contribution of the electrodes, Z_{el}, over the 100 Hz–10 MHz frequency range. Data are presented as mean ± SD from three independent measurements. (d) Frequency-resolved error analysis displaying phase deviations (degrees) and modulus differences (percent) for the electrode-included impedance at each measured frequency.

curacies near 0° and ±180° (up to 8°), operating outside these critical regions explains the limited error observed. The very low phase deviation further indicates that this error is deterministic, confirming the stability and repeatability of the system.

Performance Comparison with Literature

The use of commercial ICs, as reported in the literature, enables impedance spectrum analysis within a limited frequency range of less than 1 MHz. In contrast, this circuit solution employs high-performance components to achieve a broader frequency spectrum, making it suitable for applications from 100 Hz up to 10 MHz. This extended range allows the developed circuit to address both low-frequency and high-frequency bioimpedance measurements. As shown in Table 3.3, compared to commercial IC-based solutions, the achieved frequency span is one order of modulus higher (about 10× wider) while maintaining reduced estimation errors for both modulus and phase.

Previous works, such as the BIS device developed by [79], demonstrated gain–phase detection using the AD8302 IC but exhibited significant limitations at both low frequen-

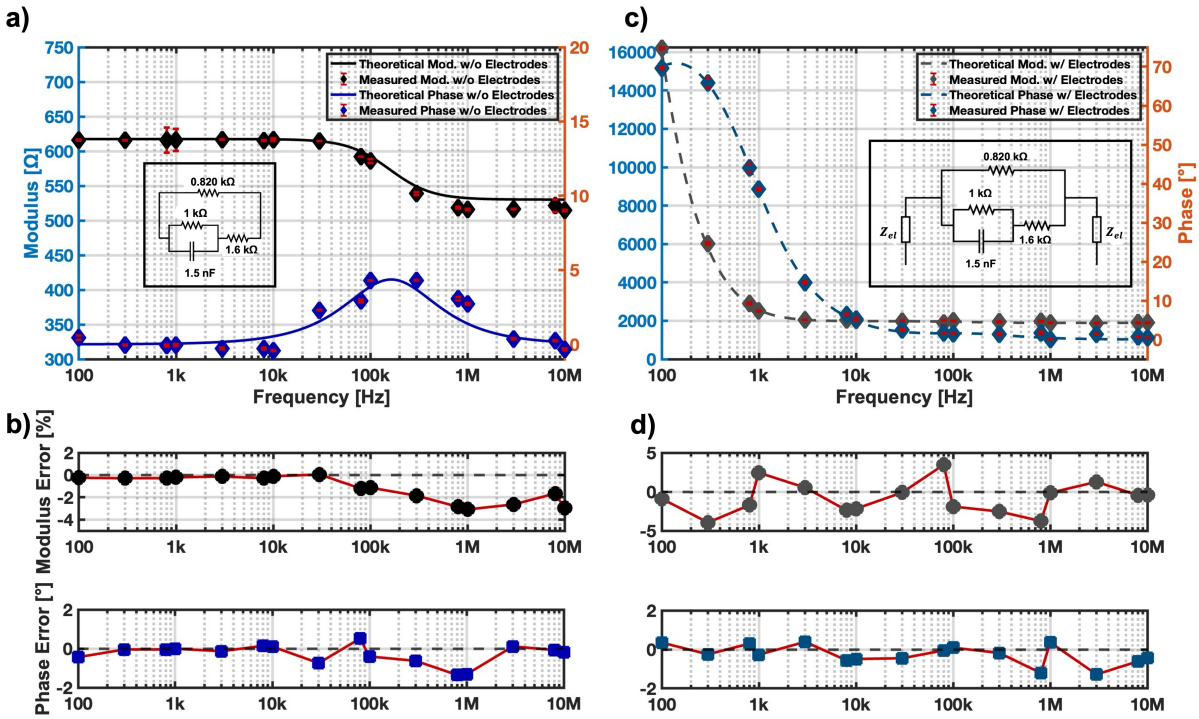

Figure 3.24: (a) Experimental and theoretical comparison of impedance modulus and phase for a breast cancer cell model over the 100 Hz–10 MHz frequency range. Data represent the mean ± SD from three independent experiments. (b) Frequency-resolved error analysis showing phase differences (degrees) and modulus deviations (percent) at each measured frequency. (c) Experimental and theoretical comparison of impedance modulus and phase for a breast cancer cell model including the contribution of the electrodes, Z_{el}, over the 100 Hz–10 MHz frequency range. Data represent the mean ± SD from three independent experiments. (d) Frequency-resolved error analysis showing phase differences (degrees) and modulus deviations (percent) for the electrode-included impedance at each measured frequency.

cies (below 20 kHz) and high frequencies (above 1 MHz), with validation on RC test circuits. Additional AD8302-based studies [72, 73, 74] have further highlighted challenges related to low-frequency accuracy, dynamic-range constraints, and bandwidth limitations. In particular, [72] applied the AD8302 to discriminate different types of meat but operated within a restricted spectral range limited to approximately 100 kHz; [73] characterized mixtures of mineral water and milk across 100 Hz–100 kHz, likewise constrained to the low-frequency regime; and [74] performed measurements on RC test impedances designed to emulate basic bioimpedance behaviours, covering a frequency span from 10 kHz to 125 kHz. In contrast, this work broadens the frequency range to 100 Hz–10 MHz, extending both the lower limit and the conventional upper limit near 1 MHz by one decade, while maintaining high accuracy. This is enabled by an adaptive dynamic-gain and a matched reference path that prevent over-range at the AD8302 inputs and actively compensate inter-path mismatches, preserving linear scaling and reducing systematic errors across the entire bandwidth.

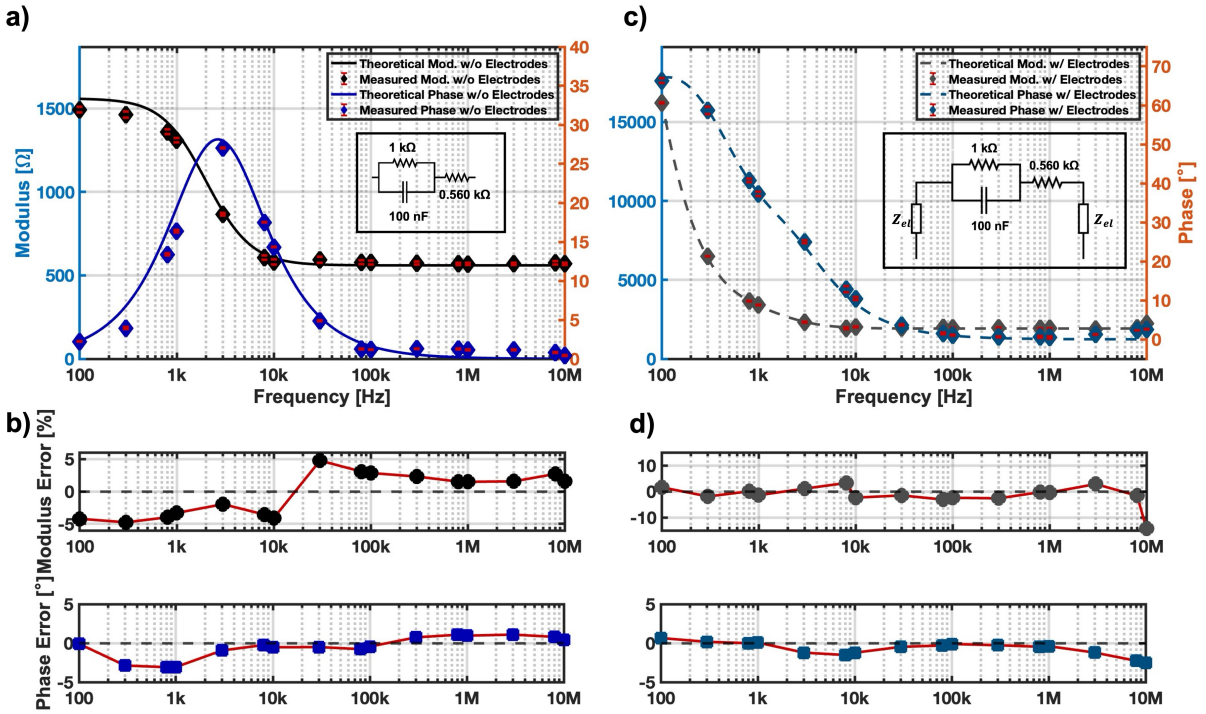

Figure 3.25: (a) Experimental and theoretical comparison of impedance modulus and phase for a Cole–Cole model of biceps tissue across the 100 Hz–10 MHz frequency range. Data are presented as mean ± SD from three independent measurements.(b) Frequency-dependent error analysis showing phase deviations (degrees) and modulus differences (percent) for each frequency point. (c) Experimental and theoretical comparison of impedance modulus and phase for a Cole–Cole model of biceps tissue including the contribution of the electrodes, Z_{el}, across the 100 Hz–10 MHz frequency range. Data are presented as mean ± SD from three independent measurements.(d) Frequency-dependent error analysis showing phase deviations (degrees) and modulus differences (percent) for the electrode-included impedance at each measured frequency.

Table 3.3: Performance summary and comparison with state-of-the-art works

	IC	Frequency Range [Hz]	Impedance Range [Ω]	Modulus Error [%]	Phase Error [°]
This work	AD8302	100–10M	100–1M	14.42	5.73
[67]	AD5933	1–100k	100–1M	1	1
[68]	AD5933	1–100k	*	*	*
[69]	AD5933	1k–100k	100–1M	*	*
[78]	AD5933	1k–100k	100–1M	3.5	2.8
[70]	AD9850	5–200k	*	10	*
[71]	AD9850	10–100k	*	10	*
[72]	AD8302	10k–100k	*	*	*
[73]	AD8302	100–100k	*	1.5	*
[74]	AD8302	10k–125k	*	10	2
[79]	AD8302	20k-1M	9–5.7k	5.13	0.4
[80]	MAX30009	1k–500k	10–100k	*	*
[81]	AD5941	10k–150k	10–100k	4.3	3
[82]	AD5941	10k–125k	10–100k	10	2
[83]	AFE4300	1k–511k	1-10k	*	*

* Not reported.

3.3 Improving the performance of Bio-Impedance Spectroscopy via Dynamic Direct Sampling : design and test of a low-Cost Microcontroller based device

Placed within the broader framework of digital demodulation techniques, the direct sampling approach represents a natural evolution toward fully digital impedance measurement systems. In this method, the signal is directly digitized without analog down-conversion, enabling the extraction of amplitude and phase information entirely in the digital domain. This significantly simplifies the analog front-end while improving flexibility, accuracy, and measurement speed.

Unlike traditional analog demodulation, direct sampling eliminates the need for phase-shifting networks and narrowband filters, allowing the use of higher-bandwidth low-pass filters (LPFs) that readily satisfy ADC anti-aliasing requirements. Moreover, by avoiding intermediate frequency conversion, the system achieves higher measurement throughput and reduced latency.

Building on this concept, the proposed work introduces a portable and low-cost impedance measurement device that integrates dynamic sampling through firmware optimization and a tunable circuit architecture. The system directly quantizes the impedance-modulated signal, while an adaptive acquisition algorithm dynamically adjusts sampling parameters to optimize performance [**Paper V**]. This strategy minimizes memory usage, accelerates frequency transitions, and shortens overall measurement time—ensuring fast, efficient, and safe bioimpedance data acquisition.

3.3.1 System Overview

The proposed portable system consists of a MCU and an analog electronic front-end which is responsible for the control and stimulation of the sample, realized through a modulated constant current signal. The designed PCB for the electronic interface measures 40×80 mm and functions as a shield for an MCU evaluation board, which has dimensions of 90×60×15 mm, as shown in Fig. 3.26(b). The proposed system aims to leverage the architecture of the MCU to generate and sample the signal using an automated algorithm for dynamic sampling and optimal parameter selection for each measurement, thus avoiding large buffer variables and unnecessary memory space occupation. By maximizing the performance of the used MCU through the management and configuration of peripherals, a maximum sampling frequency of 2.4 Msps can be achieved, allowing optimal sampling of signals to a maximum of 200 kHz. The optimized configuration of the peripherals through the developed algorithm enables dynamic sampling, which saves measurement and data transmission time. Specifically, to perform 30 frequency measurements between 10 Hz and 200 kHz, a total measurement time of 53.5 seconds is required. This includes ADC

sampling, DMA transfer, and data transmission. With dynamic sampling frequency, the time required to collect 1500 samples ranges from 625 μs at the highest sampling rate to 650 ms at the lowest. This frequency range is particularly relevant for impedance spectroscopy applications, which typically operate between 0.1 Hz and 100 kHz [84]. Additionally, another area of application could be bioelectrical impedance analysis, which includes two modes: SF-BIA, or single frequency bioelectrical impedance analysis, where the inspected frequency is typically 50 kHz [85, 86]; and MF-BIA, or multi-frequency bioelectrical impedance analysis, with a range of interest from 5 kHz up to over 200 kHz [87].

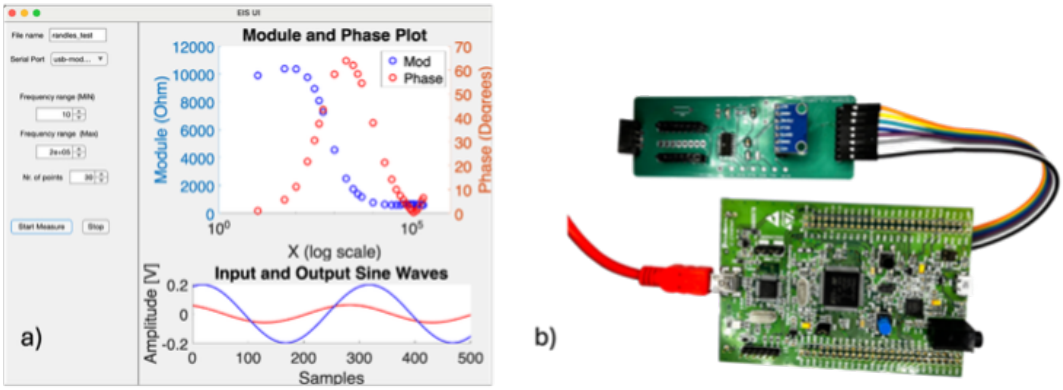

Figure 3.26: a) Developed GUI; b) Developed electronic interface connected to MCU board.

Analog front-end

The proposed system, shown in Fig. 3.27, is based on the use of a small current stimulus as excitation signal: this approach avoids applying excessively high currents that could damage the sample under analysis. The excitation signal is generated by the Analog Devices AD9833 integrated circuit, which is a low-power programmable waveform generator. Its internal frequency registers are 28 bits wide: with a 25 MHz clock rate, a resolution of 0.1 Hz can be achieved. The communication protocol is a 3-wire serial interface, which operates at clock rates up to 40 MHz and is compatible with DSP and standard microcontrollers. The IC operates at 3.3 V. Since the signal generated by the AD9833 ranges from 38 mV to of 650 mV, a signal attenuation stage has been implemented using a buffered resistive voltage divider consisting of two multiplexers. The AD9833 IC acts as a Voltage-Controlled Current Source (VCCS), providing a variable current output proportional to the set resistance. The set resistance also aids in reducing the error introduced by the delay of the VCCS in the generated signal. In fact, the voltage across the reference resistor exhibits the same phase as the current. Therefore, serves as a reference for measuring the phase and magnitude of the unknown impedance, mitigating the effect of the delay introduced by the VCCS and nonlinearities. Because the AD9833 generates a fully positive signal, the next stage consists of a variable offset generator which allows centering

the signal on a specific offset baseline. The signal attenuation and offset generation are achieved through the use of a bank of resistors controlled by a digital switch. Once the sinusoidal current signal is generated through the VCCS and shifted with the desired offset, it is then conditioned through a low pass filtering stage.

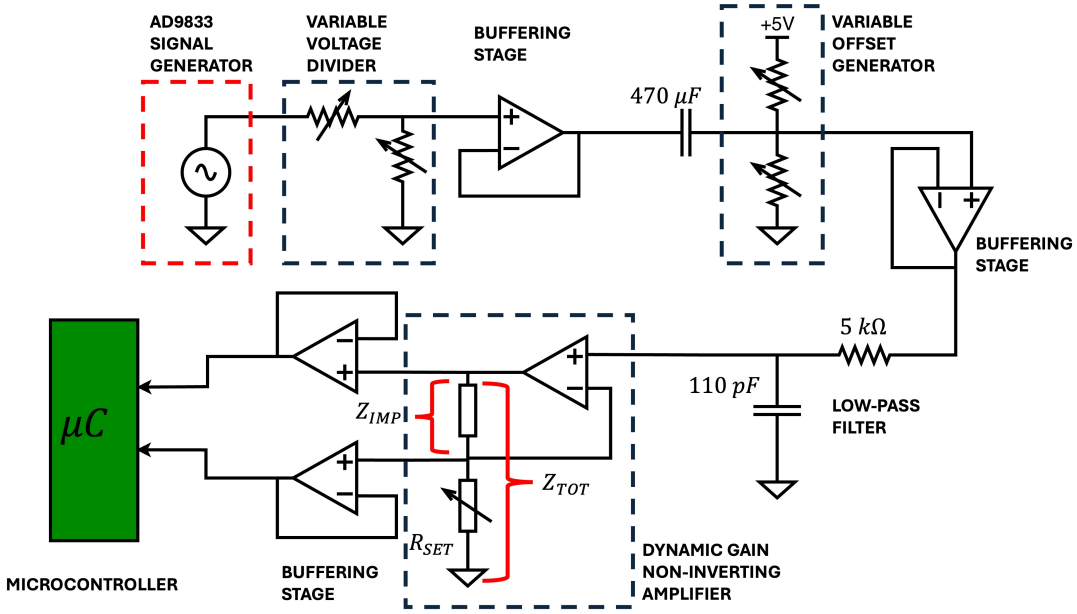

Figure 3.27: Schematic circuit design proposed for the analog front-end circuit consisting of: signal generator; conditioning and filtering of the signal; application of the signal to the unknown impedance.

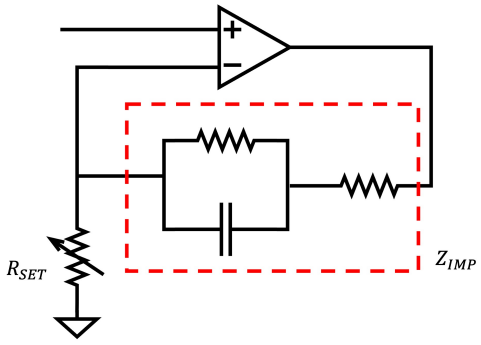

Figure 3.28: Schematic of the dynamic gain non-inverting amplifier.

The implemented filter is a first order buffered RC Low-Pass Filter with a cutoff frequency of 300 kHz. The impedance control and current application stage to the unknown impedance is realized using a wide bandwidth operational amplifier OP484 (Analog Devices) in a non-inverting amplifier configuration. It consists of the unknown impedance in the feedback path Zimp and a bank of resistors managed by a multiplexer for tuning the applied current for the impedance inspection. Using a non-inverting configuration, as shown in Fig. 3.28, the bandwidth gain can be expressed as equation (1).

$$A = 1 + \frac{Z_{imp}}{R_{set}} \tag{3.29}$$

Since Z_{imp} is an unknown impedance, it is crucial to evaluate the optimal operating point of the amplifiers to avoid bandwidth attenuation or phase variations due to dynamic-gain amplifier behavior. After the non-inverting amplifier stage with variable gain, there is a signal buffering stage before uC ADC channels. This buffering stage is implemented using two voltage followers for impedances matching between the ADC and the previous stage.

MCU setup and algorithm

The microcontroller used belongs to the STM32F407xx family and is based on the high-performance Arm Cortex-M4 32-bit RISC core operating at a frequency of up to 168 MHz. The microcontroller has been programmed to optimize the use of the ADC for sampling to minimize resource usage in terms of memory and achieve dynamic sampling based on the input frequency. Specifically, two channels of the internal ADC, ADC1 and ADC2, were used in DUAL REGULAR SIMULTANEOUS MODE, where the two converters are synchronized in terms of sampling time and conversion time. The ADC is configured to achieve a resolution of 12 bits, enabling the following CCM (Continuous Conversion Mode) and DMA Continuous Requests. Internally, the ADC has a minimum prescaler that needs to be set, which is divided by two. Considering the highest sampling rate, the calculation for Fast conversion mode:

$$\frac{\text{PCLK2}}{\text{15 ADCCLK cycles}} = 2.4 \text{ MSps (Mega Samples per second)} \tag{3.30}$$

Table 3.4: ADC Settings of STM32F407 Microcontroller

AHB Prescaler	**APB2 Prescaler**	**PCLK**	**Sampling Rate**
512	16	8.78 kHz	585 sps
64	16	70.31 kHz	4.7 ksps
16	8	562.6 kHz	37.5 ksps
8	4	2.25 MHz	150 ksps
4	2	9 MHz	600 ksps
2	2	36 MHz	1.2 Msps
1	2	72 MHz	2.4 Msps

Sampling under these conditions would result in a fixed acquisition frequency, leading to over-sampling issues. Therefore, an algorithm has been developed that allows real-time adjustment of the acquisition frequency based on the signal being acquired. By changing the acquisition frequency, and consequently the internal clock frequency, the communica-

tion parameters are also adjusted accordingly as reported in Table 3.4. However, thanks to this optimization of the sampling and data transmission process, the communication speed remains constant, with only the acquisition frequency being changed. From the block diagram of the acquisition process, it can be observed that the process is repetitive as reported in Fig. 3.29.

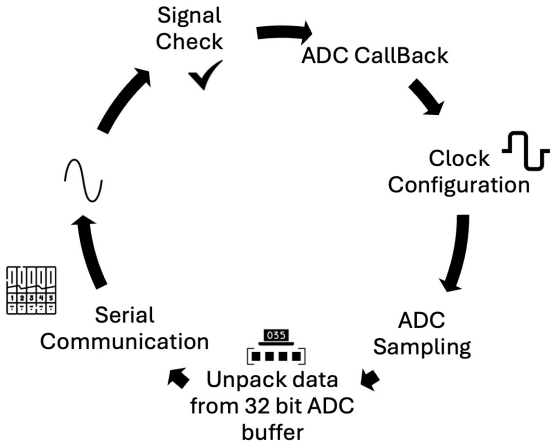

Figure 3.29: Schematic diagram of the steps of the implemented algorithm.

This process consists of several steps:

1. Selection of the stimulation sinusoid frequency.
2. Checking the signal to correctly set R_{set}.
3. Simultaneous reading from the two ADCs.
4. Configuration of the clock for the next acquisition.
5. Saving data from the ADC registers via DMA transfer to volatile variables.
6. Unpacking the burst of values from the DMA.
7. Reconfiguration of the clock for data transmission via the serial port.

This process is then repeated based on the number of set frequency scans. The main advantage of this control flow is the ability to sample low-frequency signals using the internal clock prescalers of the microcontroller, avoiding the need to buffer large amounts of samples. At lower sampling frequencies, even signals with lower frequencies will require only a few periods.

Signal Processing & Parameter Calculation

The real-time data analysis of the received data from the microcontroller was performed using MATLAB (MathWorks, USA). The analysis focused on both the total impedance of the set resistor and the impedance of the sample to be analyzed without the presence of R_{set}. This was achieved by sampling both the signal at R_{set} and the signal corresponding to the total impedance simultaneously.

$$Z_{\text{tot}} = Z_{\text{imp}} + R_{\text{set}} \tag{3.31}$$

Having both the input and output signals, after calculating the magnitude and phase of the signal through Fourier transform of the total impedance, we used the Fast Fourier Transform (FFT) to speed up the operation effectively. The FFT transforms an N-point time-domain signal into an N-point frequency-domain signal, and the input time-domain signals are referred to as the real and imaginary parts, corresponding to the outputs in the frequency domain.

$$|Z_{\text{tot}}| = \frac{|V_{\text{tot}}|}{\left|\frac{V_{\text{in}}}{R_{\text{set}}}\right|} \tag{3.32}$$

$$\angle Z_{\text{tot}} = \tan^{-1}\left(\frac{Z_{\text{tot-im}}}{Z_{\text{tot-re}}}\right) \tag{3.33}$$

The transfer function of the total impedance was calculated as:

$$\frac{V_{\text{out}}}{V_{\text{in}}} = \frac{Z_{\text{imp}} + R_{\text{set}}}{R_{\text{set}}} \tag{3.34}$$

and consequently, the transfer function of only Z_{imp} can be written as:

$$Z_{\text{imp}} = \left(\frac{V_{\text{out}}}{V_{\text{in}}} - 1\right) R_{\text{set}} \tag{3.35}$$

To evaluate the effectiveness of the circuit, calibrations were performed by reproducing representative impedances pertaining to biomedical and biological applications. The impedance values were obtained from the literature and adapted for commercially available components, including the Cole-Cole model for biceps [57], circuits for breast cancer cells [56], and forearm [88].

Measurements were taken for each unknown impedance, with a frequency spectrum ranging from 10 Hz to 200 kHz and an input sinusoid amplitude tuned in current based on the impedance of interest, from 30 μA to a maximum of 638 μA. The measurements were then compared with the theoretical calculation of the transfer function corresponding to the measured impedance.

3.3.2 Results and Discussions

The measured impedances are reported in Fig. 3.30, comparing the experimental results with the calculated results through the transfer functions of each individual impedance.

Figs 3.31(a), 3.31(b), and 3.31(c) show excellent performance in terms of modulus and phase for both the unknown impedance Z_{imp} and the total impedance including R_{set}. Most errors occur at higher frequencies, where the sampling of the sinusoidal signals is less dense.

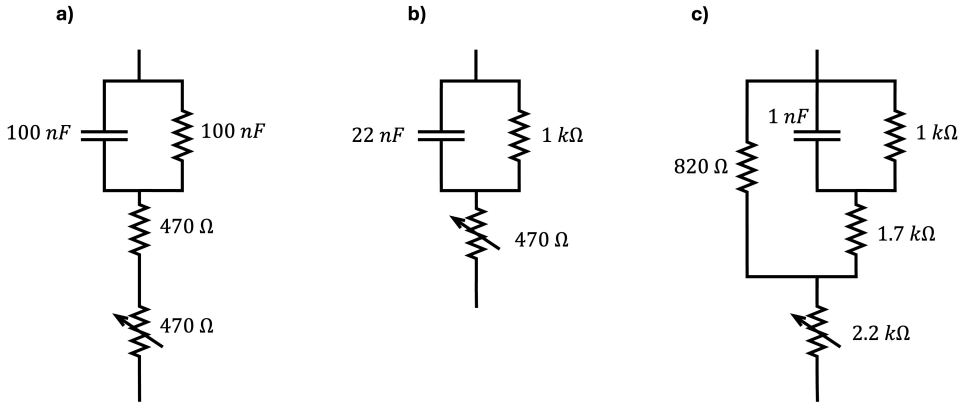

Figure 3.30: Electrical model of tested impedances: a) Biceps [57]; b) Breast cancer cells [56]; c) Forearm [88]

Regarding measurement time, the developed algorithm reduces oversampling and requires less memory to save data in real-time. Performance was evaluated by calculating the relative error for magnitude and the error in degrees for phase. For the frequency range of interest, the proposed EIS system achieved, in the worst case, a maximum mean magnitude error of 3.48% and a maximum mean phase error of 1.71° for the impedance under measurement Z_{imp}. The primary source of error at higher frequencies can be attributed to parasitic capacitance. For the total impedance, including the set resistor, the worst-case maximum mean magnitude error was 0.73% and maximum mean phase error was 0.31° for Z_{tot}. The power consumption of the device was monitored during measurement using a USB current meter and resulted in a power increase of 155 mW.

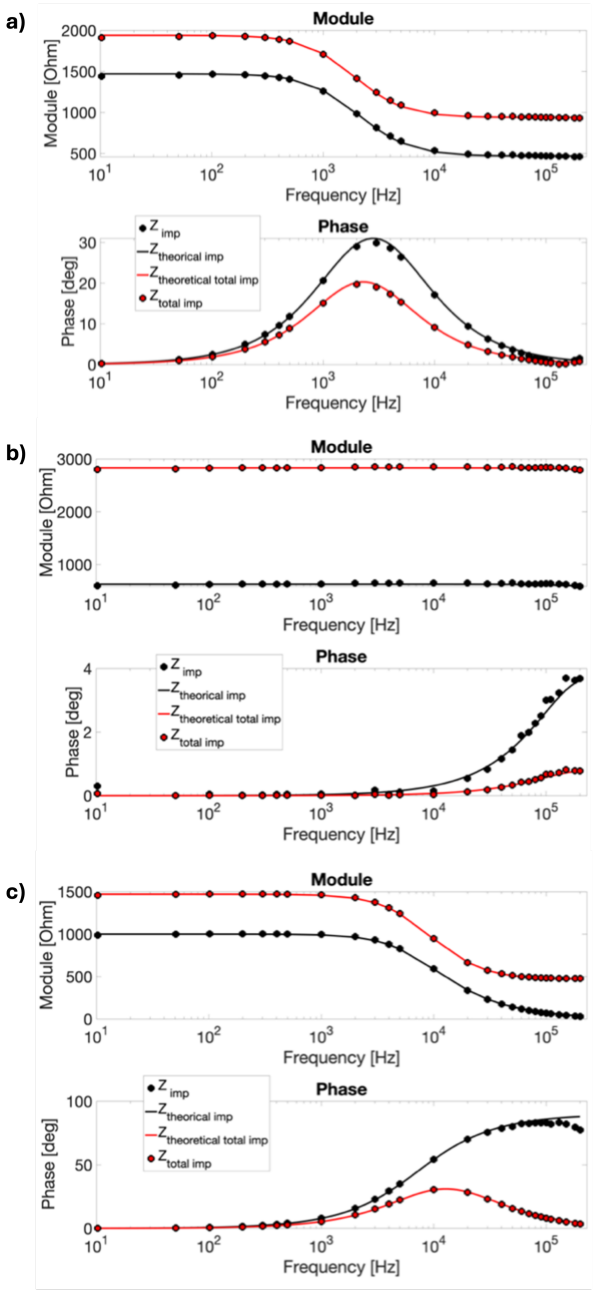

Figure 3.31: Comparison between simulated (solid lines) and experimental (dotted lines) frequency spectra of the equivalent electrical circuits: (a) biceps muscle [57], (b) breast cancer cells [56], and (c) forearm [88]. In all cases, the black curves represent Z_{imp}, while the red curves represent Z_{tot}.

Table 3.5: Comparison of devices for impedance analysis and EIS

Device	**Cost**	**Frequency Range [Hz]**	**Impedance Range [Ω]**	**Meas. Time**	**Error Mag. [%]**	**Circuit Topology**	**CPU**
This work	30 $	10–200 kHz	100 Ω–800 kΩ	625 µs–650 ms	<1	Non-inv. amplifier	MCU
Agilent 4294A	24k $	40–110 MHz	3 mΩ–500 MΩ	200 ms	0.08	*	*
ZXP ZX70A	3k $	20–500 kHz	0.01 mΩ–99.99 MΩ	4 s / 400 pts	0.1	*	*
Sensit Smart	1k $	16 mHz–200 kHz	*	*	*	*	*
[89]	100 $	0.01–100 kHz	10 Ω–10 GΩ	30 s / 1 kHz–100 kHz	<5	Log. amp	MCU
[90]	25 $	0.01–50 kHz	1 Ω–50 kΩ	*	<5	*	MCU
[91]	<80 $	2–1.5 kHz	200 Ω–1 MΩ	*	<15	Pot. 3-electrode	MCU
[67]	100 $	1–100 kHz	100 Ω–1 MΩ	*	<8	Gain and phase detector	MCU
[92]	45 $	100–500 kHz	10 Ω–100 kΩ	800 ms / 33 pts	<2.5	Auto. bridge	FPGA
[93]	95 $	10–1000 kHz	100 Ω–200 kΩ	460 ms / 28 pts	0.3	Auto. bridge	FPGA
[94]	*	0.1–10 kHz	1 kΩ–1 GΩ	*	4	Auto. bridge	DSP
[95]	*	1 kHz–10 MHz	100 Ω–10 MΩ	3.5 ms / single pt	<1	Auto. bridge	FPGA
[96]	400 $	10–1000 kHz	1 Ω–10 kΩ	72 ms @1 kHz / single pt	<2	4-term diff. amp	FPGA
[74]	90 $	10–125 kHz	2 Ω–2 MΩ	*	<10	IC AD8302	MCU

* Not reported

3.4 Summary and Future Perspectives

This chapter provided an overview of bioimpedance spectroscopy (bio-Z), covering measurement principles, circuit architectures, and interface design considerations for accurate tissue characterization. Key topics included the electrical properties of biological tissues, electrode configurations, and the influence of electrode-tissue interface impedance on measurement accuracy. Current-mode bio-Z interfaces were analyzed, highlighting current generators, voltage readout stages, and ADCs, with discussion of trade-offs between power consumption, linearity, and measurement precision.

Two main demodulation strategies were examined: I/Q and polar. I/Q demodulation offers high accuracy, robustness to noise, and flexible digital post-processing but comes at the cost of increased power and circuit complexity. Polar demodulation provides a simpler, energy-efficient, and compact solution suitable for wearable or implantable systems, though careful calibration is required to mitigate offsets, noise, and harmonic distortion. ADC selection, whether SAR or $\Delta\Sigma$, also affects interface gain, SNR, and latency.

Several notable circuit implementations were reviewed to illustrate these concepts. One approach employed polar demodulation with dedicated reference paths, achieving operation up to 1 MHz with amplitude and phase errors below 11% and 0.51°, minimizing sensitivity to delays and comparator errors. Another utilized the AD8302 IC to create a linear measurement circuit up to 10 MHz, incorporating reference paths and gain control to compensate for phase and attenuation variations while supporting both 2- and 4-electrode configurations. A third implementation focused on a portable, low-cost device operating from 10 Hz to 200 kHz, using a dynamic-gain amplifier and optimized microcontroller sampling to achieve fast and accurate measurements while preserving linearity and minimizing thermal effects on biological samples. These works collectively demonstrate that innovative circuit designs can enhance measurement accuracy, bandwidth, and portability in bio-Z systems.

Looking ahead, advancements in low-power mixed-signal design, miniaturization, and integration are expected to further improve portable and wearable bioimpedance devices. Future systems will likely combine optimized current generators, low-noise voltage readouts, and adaptive demodulation to balance accuracy, energy efficiency, and compactness, enabling continuous, long-term monitoring of physiological parameters. Developments in hybrid analog-digital processing, on-chip calibration, and intelligent signal reconstruction will further enhance robustness against electrode variability, motion artifacts, and tissue heterogeneity, expanding the potential applications of bio-Z spectroscopy in healthcare, rehabilitation, sports, and biosensing research.

Chapter 4

Toward Integrated Electrical Stimulation for Reverse Iontophoresis

The use of electrical stimulation in medicine dates back to ancient Egypt, where electric catfish were employed to relieve joint pain [97]. In the eighteenth century, Luigi Galvani observed that a frog's leg twitched when exposed to an electrical spark, laying the foundation for the study of electrophysiology [98]. During the nineteenth century, Michael Faraday's research furthered the understanding and control of electrical currents, leading to early devices designed for pain relief and muscle stimulation [99]. With advancements in electronic technology, electrical stimulation devices have become increasingly sophisticated, supporting the treatment of various medical conditions and the enhancement of muscle and motor function. Although not a new technique, electrical stimulation continues to evolve and remains a valuable tool in medical and therapeutic interventions. This chapter presents the design and implementation of a versatile, configurable electrical stimulation system engineered to provide accurate and safe current pulses, suitable for a wide range of research and clinical applications.

4.1 Stimulation methods

The design of stimulation circuits is inherently tailored to the specific application, with several critical factors influencing the overall architecture. These typically include the electrode type and configuration, the chosen stimulation mode, as well as waveform shape and pulse parameters. Since each application presents distinct functional requirements and design constraints, a thorough understanding of these aspects is essential for achieving optimal performance.

4.1.1 Electrode Configurations and Modeling

In electrical stimulation, electrical pulses are delivered to the body through transcutaneous electrodes. The two most common electrode arrangements are the *monopolar* and *bipolar* configurations, as illustrated in Fig. 4.1. Their main differences arise from the geometry, size, and placement of the electrodes.

In a monopolar configuration, stimulation is applied using a *working electrode* (WE) referenced to a larger *counter electrode* (CE). Typically, the smaller WE is positioned directly over the muscle's motor point, while the CE is placed over the antagonist muscle. Because the CE spreads the ionic current across a larger surface, the current density beneath it is relatively low, resulting in localized excitation near the WE. This arrangement is advantageous for targeting specific muscles with spatially focused stimulation.

In contrast, the bipolar configuration employs two electrodes of equal size, both acting as working electrodes. Here, the current density is more evenly distributed between the two electrodes, allowing current to flow longitudinally through the muscle. This arrangement generally produces stronger and more balanced muscle contractions. Accordingly, bipolar stimulation is frequently used in therapeutic applications, such as motor rehabilitation and chronic or acute pain management [100].

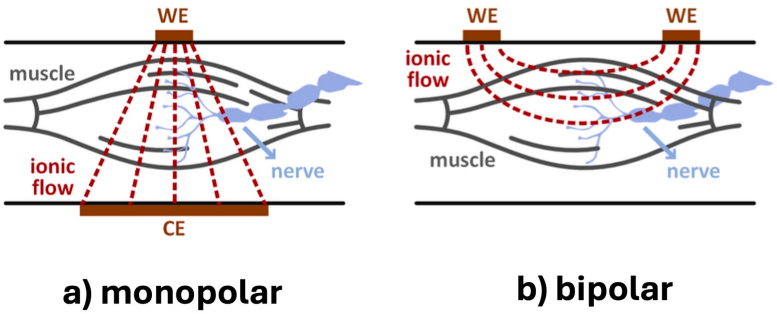

Figure 4.1: Illustration of monopolar and bipolar electrode configurations used in electrical stimulation.

4.1.2 Electrode-Skin Impedance Model

The electrode–skin interface (ESI) critically influences the effectiveness of stimulation and the design requirements of the electrical stimulation system. A commonly adopted approach is a lumped-element model of the interface, shown in Fig. 4.2. This model represents:

- the bulk resistance of the electrode electrolyte, R_b,
- the impedance of the stratum corneum, Z_{SC}, and
- the combined resistance of the dermis, subcutaneous fat, and deeper tissues, R_{sub} [101].

The stratum corneum impedance, Z_{SC}, includes both the lipid–corneocyte matrix and ionic pathways through skin appendages. It can be modeled as a parallel combination of a variable conductance, G_p, and a capacitance, C_p. The conductance G_p varies with the stimulation current $S(t)$ and can be expressed as [102]:

$$G_p(S) = a_p S(t) + b_p \tag{4.1}$$

where b_p represents the baseline conductance in the absence of stimulation, and a_p quantifies the increase in conductance relative to the applied current. Understanding ESI behavior is essential for predicting the current distribution and designing safe and effective stimulation protocols.

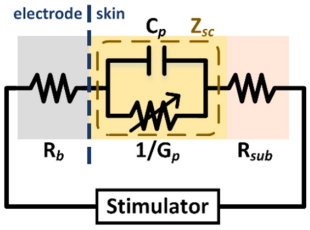

Parameter	25 cm^2	50 cm^2
$R_S{}^*$	$670 \pm 99\ \Omega$	$498 \pm 83\ \Omega$
C_P	$106 \pm 25\ nF$	$194 \pm 52\ nF$
a_P	$14 \pm 3.5\ mS/A$	
b_P	$56 \pm 33\ \mu S$	

[*] $R_S = R_b + R_{sub}$

Figure 4.2: Lumped-element model of the electrode–skin interface, summarizing the typical values for resistive and capacitive components under current stimulation.

4.1.3 Charge Delivery Methods

The performance and comfort of electrical stimulation depend heavily on the total electrical charge delivered to the target tissue. Two main approaches are used to control this charge delivery: constant-current stimulation (CCS) and constant-voltage stimulation (CVS). In both cases, the stimulator acts either as a current source or a voltage source, with a switching mechanism that directs the required signal to the electrode. Figure 4.4 illustrates the circuit configurations and resulting waveforms for both modes.

Under CCS, the voltage across the electrode-skin interface (ESI) in response to a current pulse $i(t)$ can be expressed by:

$$v(t) = i(t)R_s + i(t)R_p\left(1 - e^{-t/(R_pC_p)}\right) \tag{4.2}$$

where R_s is the series resistance, and R_p and C_p are the parallel resistance and capacitance of the interface, respectively.

In the CVS configuration, if a pulse of voltage $v(t)$ is applied, the resulting current $i(t)$ behaves as:

$$i(t) = \frac{v(t)}{R_s + R_p} - \left(\frac{v(t)}{R_s + R_p} - \frac{v(t)}{R_s}\right) e^{-t/((R_s \| R_p)C_p)} \tag{4.3}$$

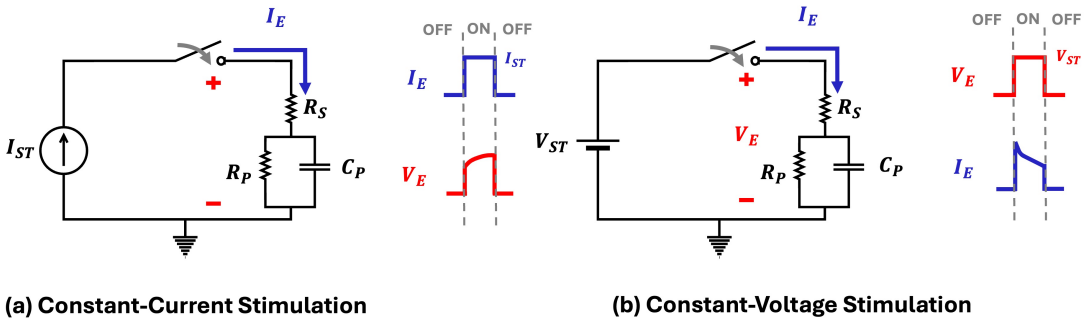

Figure 4.3: Block diagram of CCS and CVS systems with the corresponding voltage and current profiles generated by a pulsed input signal.

where $R_s \parallel R_p$ denotes the parallel combination of R_s and R_p.

The time-varying behaviour of the ESI under CVS makes it more difficult to precisely regulate the charge delivery. Because of this, CCS is often preferred in clinical stimulators since it simplifies the delivery of a balanced charge, which is essential for safety. However, in CCS operation, the voltage drop across the interface must be taken into account, requiring sufficiently high compliance voltage in the supply.

If the stimulation pulse lasts for a maximum duration T_{ST}, the minimum supply voltage $V_{DD,\text{min}}$ required to deliver a constant current I_{ST} can be approximated as:

$$V_{DD,\text{min}} = I_{ST}R_s + \frac{I_{ST}T_{ST}}{C_p} + V_H \tag{4.4}$$

where V_H represents the voltage headroom of the current driver. In practice, the compliance voltage often needs to reach several tens of volts.

4.1.4 Charge Injection Waveforms

Charge-balanced current pulses, i.e, achieving zero net charges, is a common strategy to minimize risks such as skin irritation, burns, and irreversible electrode polarization that may cause electrode degradation [103]. Charge balance can be achieved either through *biphasic pulses* (Fig. 4.4a)) or *monophasic pulses* (Fig. 4.4b)) followed by passive discharge via a capacitor, as illustrated in Fig. 4.4c).

Pulse parameters vary according to the specific application. The *stimulation current amplitude* (I_{ST}) and the *phase duration* (T_{pd}) determine the charge delivered during the stimulation phase, expressed as:

$$Q_{\text{ST}} = I_{\text{ST}} \times T_{\text{pd}} \tag{4.5}$$

Typically, I_{ST} ranges from a few milliamperes up to several tens of milliamperes, while T_{pd} lies between 100 µs and 400 µs. These parameters directly influence the evoked muscle

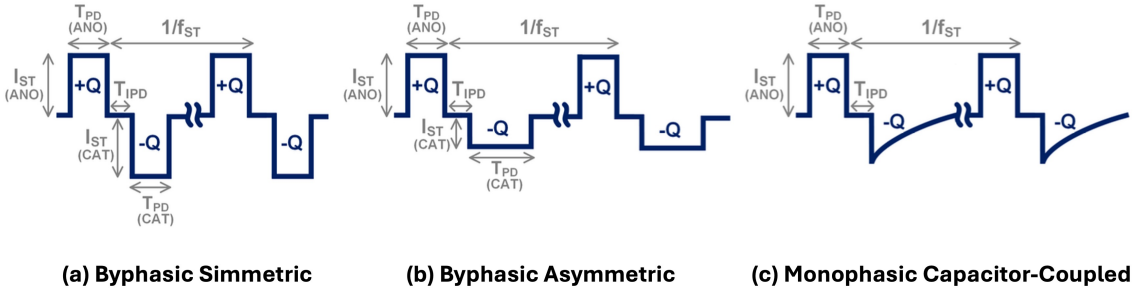

Figure 4.4: Commonly used charged-balanced stimulation waveforms.

force and are critical for ensuring safe stimulation.

The *safety boundary* for electrical stimulation can be expressed as [104]:

$$\log(Q_{\mathrm{DST}}) = k - \log(Q_{\mathrm{ST}}) \tag{4.6}$$

where Q_{DST} represents the charge density, obtained by dividing Q_{ST} by the electrode surface area, and k is a constant typically ranging from 1.5 to 1.8.

The *stimulation frequency* (f_{ST}) is generally set between 20 and 50 Hz. Frequencies below 16 Hz are often insufficient to induce sustained contractions, while higher frequencies can lead to rapid muscle fatigue [105]. The *interphase delay* (T_{ipd}), representing the silent interval between the two phases, usually ranges from 80 µs to 100 µs, helping to reduce the stimulation threshold and improve overall efficiency [106].

Therefore, *electrical stimulation* systems must offer flexible programmability of multiple waveform parameters to support diverse therapeutic and experimental applications.

4.2 Biomedical Applications of Electrical Stimulation: Iontophoresis and Reverse Iontophoresis

Iontophoresis (IP) is an advanced technique for transdermal delivery that exploits the application of a low-intensity electrical potential difference (typically $\leqslant 0.5\,\mathrm{mA/cm^2}$). This stimulus enhances the migration of ions across biological membranes, particularly the skin, allowing the administration of both ionic and non-ionic drugs through the electrochemical gradient generated by the applied field [107]. The total flux of a solute (J) across the skin can be expressed as the sum of the contributions from electrophoresis (J_{EP}), electroosmosis (J_{EO}), and passive diffusion (J_p):

$$J = J_{\mathrm{EP}} + J_{\mathrm{EO}} + J_p \tag{4.7}$$

4.2.1 Electrophoresis

Electrophoresis describes the movement of ions induced by an applied electric field. In this process, electronic current is converted into ionic fluxes through electrode reactions, ensuring overall electroneutrality. Each ionic species contributes to charge transport according to its transport number, with the sum of all transport numbers equal to unity. Based on Faraday's law, the electrophoretic flux of a given ion i can be expressed as:

$$J_{\mathrm{EP}} = \frac{t_i\, I}{F\, Z_i} \tag{4.8}$$

where t_i is the transport number of ion i, Z_i its valence, F is Faraday's constant, and I is the applied current.

4.2.2 Electroosmotic Flow

Electroosmotic flow (EOF) represents the primary transport mechanism for uncharged and high-molecular-weight species. At physiological pH, the skin carries a net negative charge, making it selectively permeable to cations [108]. This selectivity induces a convective solvent flow from the anode to the cathode, which in turn transports neutral molecules.

The EOF velocity (v_{EO}) is proportional to the applied electric field and can be described by the Smoluchowski equation:

$$v_{\mathrm{EO}} = -\frac{\varepsilon\, \zeta}{\eta}\, E \tag{4.9}$$

where ε is the dielectric permittivity of the medium, ζ is the zeta potential associated with the fixed surface charge, η is the viscosity of the solvent, and E is the electric field.

Under conditions of uniform conductivity, the electric field can be expressed as:

$$E = \rho\, I \tag{4.10}$$

where ρ is the electrical resistivity of the medium and I is the applied current density.

The electroosmotic contribution to the solute flux for a neutral species j at molar concentration c_j is therefore:

$$J_{\mathrm{EO}} = v_{\mathrm{EO}} \cdot c_j \tag{4.11}$$

The relative contributions of electrophoresis, electroosmosis, and passive diffusion depend on the structure and physicochemical properties of the transported species. For small ions, such as Na^+ or Cl^-, electrophoresis is typically the dominant transport mechanism, whereas neutral solutes are primarily transported by electroosmotic flow and passive diffusion.

4.2.3 Reverse Iontophoresis

Reverse iontophoresis (RI) is a diagnostic variant of iontophoresis that applies an electric field to extract interstitial fluid (ISF) and its solutes through the skin for monitoring purposes [109]. It enables non-invasive detection of biomarkers such as glucose, lactate, urea, and selected drugs. The mechanisms underlying RI mirror those of conventional iontophoresis, with solute transport governed by electromigration and electroosmosis.

According to Faraday's law, the molar flux of an ion i is related to the partial current it carries:

$$I_i = Z_i F J_i \tag{4.12}$$

where I_i is the current carried by ion i, Z_i its valence, F Faraday's constant, and J_i its molar flux.

The total current is given by the sum of all ionic contributions:

$$I = \sum I_i \tag{4.13}$$

Introducing the transport number $t_i = \frac{I_i}{I}$, the molar flux can be expressed as:

$$J_i = \frac{t_i\, I}{Z_i F} \tag{4.14}$$

Assuming constant current over a time interval T, the total molar amount of ion i extracted is:

$$M_i = \frac{t_i\, I\, T}{Z_i F} \tag{4.15}$$

and the total extracted amount is:

$$M = \sum M_i \tag{4.16}$$

Due to the net negative charge of the skin at physiological pH, cation extraction is favored, while electroosmotic flow significantly contributes to the transport of neutral species. The efficiency of RI depends on several factors, including skin permeability, electrode material, hydrogel conductivity, current intensity, and waveform characteristics. Ag/AgCl electrodes are commonly employed due to their biocompatibility and electrochemical stability.

4.3 System architecture

The previous sections have outlined the general design requirements and associated challenges of electrical stimulation applications. This section further examines incremental efforts toward integrated solutions for RI systems, specifically tailored for portable and wearable implementations. As depicted in Fig. 4.5, the proposed architecture comprises a configurable stimulator [**Paper II**], with a current-monitoring module for ensuring safe stimulation, and a HV voltage generator. The following subsections will elaborate the system.

4.3.1 Configurable Electrical Stimulator

The electrical stimulator circuit is the core building block in for the stimulation system, serving as the output stage that interfaces with the skin. This system enable the stimulation signal to a level sufficient to deliver current controlled pulses to the skin. The devices incorporate microcontroller units (MCU) for precise control and programmability, allowing for complex stimulation patterns and user-friendly interfaces.

4.3.2 Circuit Implementation

The developed device is composed of four main functional blocks, as shown in Fig. 4.5:

- **High Voltage Power Supply:** This block is needed to supply high voltages if stimulating high-impedance loads.
- **Voltage-controlled current sink:** This circuital block is used to inject the desired amount of current into the stimulated tissue, regardless of its impedance (within a certain range). A current sink topology was chosen over a current source topology in order to allow the use of low voltages as control signals, produced directly by a DAC without the need of further conditioning (e.g., amplification stages).

- **Current mirror:** The current mirror block is needed to apply to the stimulated tissue the current produced by the current sink.
- **H-bridge:** The H-bridge block is used to apply biphasic stimuli to the tissue without the need of a dual power supply.

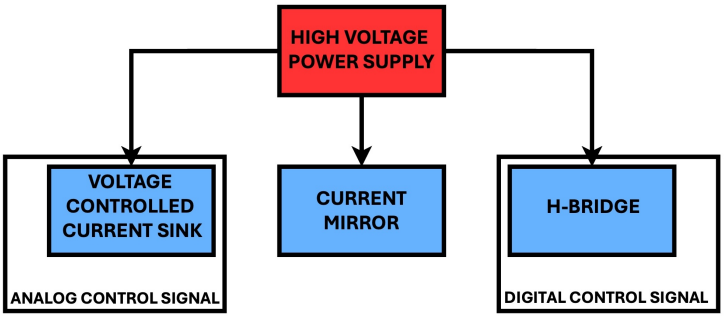

Figure 4.5: Block diagram of the developed electronic interface.

The high voltage power supply is based on the R05-100B (RECOM Power GmbH, Austria), a current mode DC/DC switching converter operating from a 4.5 V to 6 V input value. The output voltage is equal to 120 V with an input voltage of 5 V and the maximum output current is equal to 25 mA. The voltage-controlled current sink block is implemented as shown in Fig. 4.6. The desired current is set by providing a voltage Vin, on the non-inverting input pin of the op-amp U1 (an ADA4505, Analog Devices), through the internal DAC of a µC (SAM3X8E ARM Cortex-M3, Atmel, San Jose, California USA).

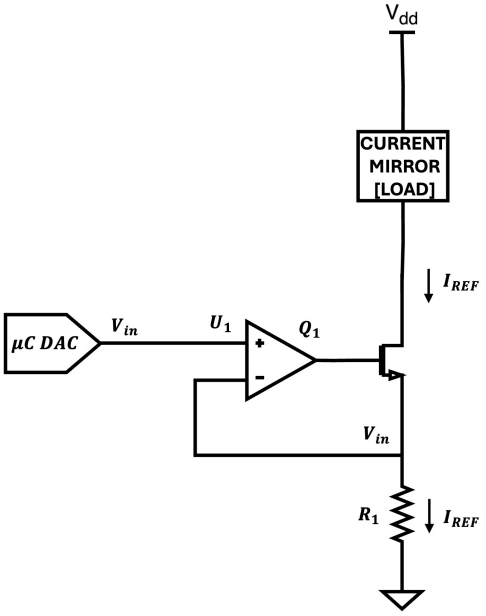

Figure 4.6: Schematic of the voltage controlled current sink circuit.

The current I_{REF} flowing through the load is given by the equation:

$$I_{\mathrm{REF}} = \frac{V_{\mathrm{in}}}{R_1} \tag{4.17}$$

In fact, as a current flows through the load, a voltage is obtained across R_1. The op-amp uses the sensed voltage as feedback and drives its output until the sensed voltage is equal to the DAC output V_{in}. In this case, transistor Q1 (commercial device FDN86246, Onsemi, Scottsdale, AZ, USA) operates in the linear region as a voltage-controlled resistance.

The DAC used supports 12-bit resolution with a 3.3 V power supply. If R_1 is equal to 100 Ω, the sink current theoretically ranges from 0 to 33 mA with a minimum step of 8 μA (from Equation 4.17). A voltage V_{cc} equal to 120 V is provided by the high-voltage power supply stage. The current mirror block is implemented as shown in Fig. 4.7.

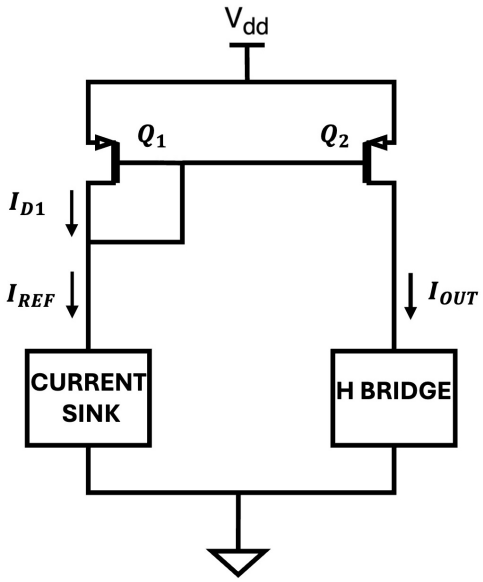

Figure 4.7: Schematic of the current mirror circuit.

The P-MOS transistor Q1 (ZVP1320FTA, Diodes) works in saturation mode because the drain is shorted to its gate. In this region, the thickness of the channel at the drain decreases until it nullifies, and it is said that the channel is in pinch-off, for ΔL tending to zero. The channel length decreases by an amount ΔL. As V_{DS} increases, ΔL increases, so in the saturation region, the slope of the curve also depends on V_{DS} through the channel modulation factor λ. It is possible to approximate λ as a parameter inversely proportional to the channel length as:

$$l = \sqrt{\frac{\varepsilon}{qL^2 N_A}} \approx \frac{10^7}{L\sqrt{N_A}} \approx 0.1 \ \mathrm{V}^{-1} \tag{4.18}$$

for typical L values in the simulation range.

In this case, the drain current I_{D1} is equal to I_{REF}, given by:

$$I_{D1} = I_{\mathrm{REF}} = \frac{1}{2}\left(\mu_p C_{\mathrm{ox}} \frac{W}{L}\right)_{Q1} (V_{\mathrm{GS}} - V_{\mathrm{TH}})^2 (1 + lV_{\mathrm{DS}}) \tag{4.19}$$

If also Q2 (ZVP1320FTA, Diodes) is operating in saturation, its current is equal to:

$$I_{D2} = I_{\mathrm{OUT}} = \frac{1}{2}\left(\mu_p C_{\mathrm{ox}} \frac{W}{L}\right)_{Q2} (V_{\mathrm{GS}} - V_{\mathrm{TH}})^2 (1 + lV_{\mathrm{DS}}) \tag{4.20}$$

so the relation between I_{OUT} and I_{REF} can be expressed as:

$$\frac{I_{\mathrm{OUT}}}{I_{\mathrm{REF}}} = \frac{I_{D2}}{I_{D1}} = \frac{\left(\frac{1}{2}\mu_p C_{\mathrm{ox}} \frac{W}{L}\right)_{Q2} (V_{\mathrm{GS2}} - V_{\mathrm{TH}})^2 (1 + lV_{\mathrm{DS}})_{Q2}}{\left(\frac{1}{2}\mu_p C_{\mathrm{ox}} \frac{W}{L}\right)_{Q1} (V_{\mathrm{GS1}} - V_{\mathrm{TH}})^2 (1 + lV_{\mathrm{DS}})_{Q1}} \approx \frac{(W/L)_{Q2}}{(W/L)_{Q1}} \tag{4.21}$$

being $V_{GS1} = V_{GS2}$.

Using two MOSFETs with the same aspect ratio W/L, I_{OUT} is almost equal to I_{REF} (from Equation (4.21)). In the cascode configuration, transistors also operate in saturation. The cascode mirror ensures improved output resistance and better accuracy because transistors Q3 and Q4 stabilize the drain-source voltages of the mirroring transistors (Q1 and Q2) by buffering them from variations in the output voltage. This ensures a more accurate current mirroring operation.

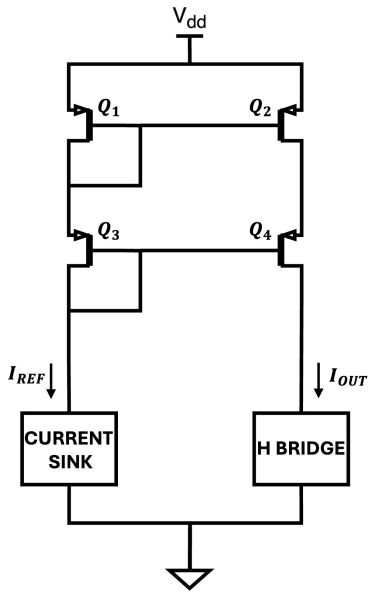

Figure 4.8: Schematic of the cascode current mirror circuit.

The H-bridge block is realized as shown in Figure 4.9. The H-bridge consists of six controlled switches represented by the MOSFETs Q1, Q2, Q3, Q4, Q5, and Q6 (N-MOS: FDN86246, Onsemi, Scottsdale, AZ, USA). The function of these MOSFETs is to control the flow of current I_{REF} through the load, represented by human tissue.

When MOSFETs Q1 and Q3 are ON (and Q2 and Q4 are OFF), a positive voltage

is applied across the load, so I_{REF} will flow from left to right, according to Figure 4.9, through the tissue. When MOSFETs Q2 and Q4 are ON (and Q1 and Q3 are OFF), the applied voltage is reversed and I_{REF} will flow through the left branch of the tissue.

Q1 and Q3 are simultaneously controlled by the N-MOS Q5, while Q2 and Q4 are simultaneously controlled by the N-MOS Q6. Control signals applied to Q5 and Q6 are square waves with a specific duty cycle, frequency, and relative phase shift, generated by a microcontroller (SAM3X8E ARM Cortex-M3, Atmel Corporation, San Jose, CA, USA) with 3.3 V logic levels.

The shunt resistances R_7 and R_8 are used to measure the biphasic current flowing through the tissue. Voltages V_{OUT1} and V_{OUT2} are applied to two INA amplifiers (INA819, Texas Instruments, Dallas, TX, USA), whose gain has been set to 30 dB, to be amplified and acquired by the microcontroller.

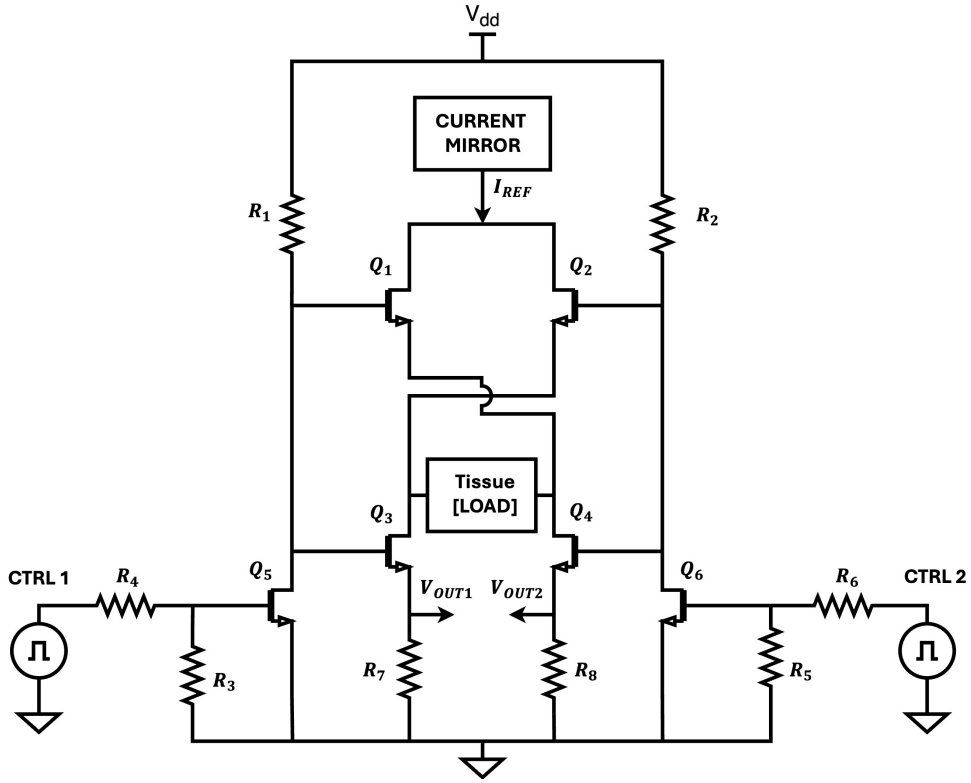

Figure 4.9: Schematic of the H-bridge circuit.

The desired current I_{REF} is set by applying a specific V_{in} to the voltage-controlled current sink block, through the internal DAC of the microcontroller. The produced I_{REF} is mirrored by the current mirror stage to the H-bridge. Controlling the H-bridge with specific square wave signals allows injection of I_{REF} in both monophasic and biphasic modes.

A PCB was designed using the EDA software Autodesk Eagle (Version 9.6.2, Autodesk Inc., San Francisco, CA, USA) and fabricated to test the performance of the developed electronic interface. During the test procedures, control signals were generated by the

microcontroller while output signals were visualized using an oscilloscope (HDO6054-MS, Teledyne LeCroy, New York, NY, USA).

The performance evaluation of the developed interface was performed using a known load impedance Z; the test load consisted of a 1 kΩ resistor. To evaluate system flexibility, the load was stimulated with both monophasic and biphasic current pulse bursts, with symmetrical and asymmetrical shapes.

The tested stimulation patterns were as follows:

- A burst of 10 monophasic current pulses with a frequency of 1 kHz and amplitude of 1 mA (each H-bridge current path tested) with duty cycles of 25%, 50%, and 75%.
- A burst of 10 biphasic symmetrical current pulses with a frequency of 1 kHz and amplitude of 1 mA.
- A burst of 10 biphasic asymmetrical current pulses with a frequency of 1 kHz, amplitude of 1 mA, and relative duty cycles with ratios of 1:3 and 3:1.

Moreover, to verify that the injected current matched the desired I_{REF}, the test load was stimulated with bursts of 10 monophasic current pulses with amplitudes ranging from 0.1 to 10 mA (0.1, 0.5, 1, 2, 3, 4, 5, 6, 7, 8, 9, 10 mA), at a frequency of 1 kHz and duty cycle of 50%. The amplitude range was chosen according to typical values reported in the literature for reverse iontophoresis applications [110], between 0.1 and 4 mA.

Additionally, to test the system in a simulated environment, electrical stimulation was used to enhance a mimicked physiological diffusion process. A custom structure, such as a reverse Franz diffusion cell, was built, as shown in Figure 4.10.

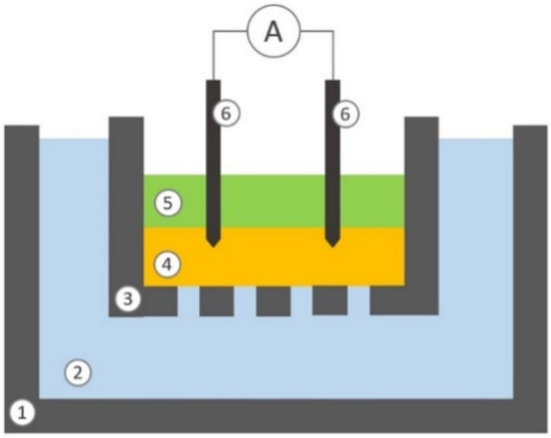

Figure 4.10: Schematic representation of the section view of the experimental setup: lower chamber (1), liquid phase contained into the lower chamber (2), upper chamber (3), hydrogel septum (4), liquid phase contained into the upper chamber (5), two electrodes (6).

The lower donor chamber (10 mL), made of polystyrene, is filled with TrisHCl buffer at pH 7.4 containing 140 mM NaCl, 4 mM KCl, and 20 mM L-ascorbic acid (Merck KGaA,

Darmstadt, Germany). The upper receptor chamber (1 mL), made of polylactide (PLA), is filled with TrisHCl buffer at pH 7.4, containing only NaCl and KCl; the bottom of the upper chamber is perforated to allow passive diffusion.

The two chambers are separated by a layer of hydrogel, made of 0.8% (w/v) agarose dissolved in TrisHCl buffer at pH 7.4 containing 140 mM NaCl and 4 mM KCl, with a thickness of 3 mm. The lower chamber simulates peripheral vessels, while the hydrogel in the upper cell simulates the dermis. The buffer composition is thus defined to reflect a simplified model of blood and interstitial fluid (ISF) systems.

Two stainless steel needles are used as electrodes, with the tips inserted 1 mm into the hydrogel upper layer. Current stimulations of 500 and 1000 µA are applied for 30 min to the dermal simulated environment, independently. To compare the electro-stimulated diffusion against the spontaneous process, passive diffusion is allowed to occur for the same amount of time (30 min) with no stimulation applied.

At the end of the experiment, the concentration of ascorbic acid in the liquid phase of the upper chamber is measured using a specific spectrophotometric assay [111].

The stimulation parameters were selected based on the most recent literature. The works considered are summarized in Table 4.1.

4.3.3 Experimental Results

Monophasic Test

Fig. 4.11 shows the stimulation pattern obtained in monophasic mode with duty cycles of 25%, 50%, and 75%, respectively. A current square wave with a frequency of 1 kHz, the corresponding duty cycle, and an amplitude of 1 mA was recorded.

Biphasic Test

Fig. 4.12 a) shows the stimulation pattern obtained in biphasic mode with symmetrical current pulses. A current square wave with both positive and negative amplitudes, ranging from 0.1 to 10 mA and a frequency of 1 kHz, was recorded. Fig. 4.12 b) shows the stimulation pattern obtained in biphasic mode with asymmetrical current pulses. A current square wave with asymmetrical timing (with a ratio of 3:1), amplitudes with a modulus ranging from 0.1 to 10 mA and a frequency of 1 kHz was recorded. Fig. 4.12 c) shows the stimulation pattern obtained in biphasic mode with asymmetrical current pulses. A current square wave with asymmetrical timing (with a ratio of 1:3), amplitudes with a modulus ranging from 0.1 to 10 mA and a frequency of 1 kHz was recorded.

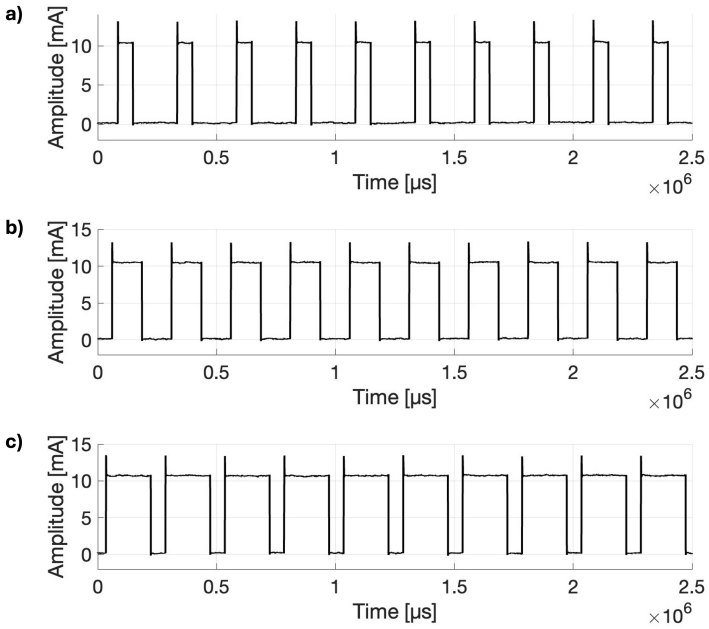

Figure 4.11: Monophasic stimulation pattern with three different duty cycles and an amplitude of 1 mA: duty cycle of 25% (A), duty cycle of 50% (B), duty cycle of 75% (C).

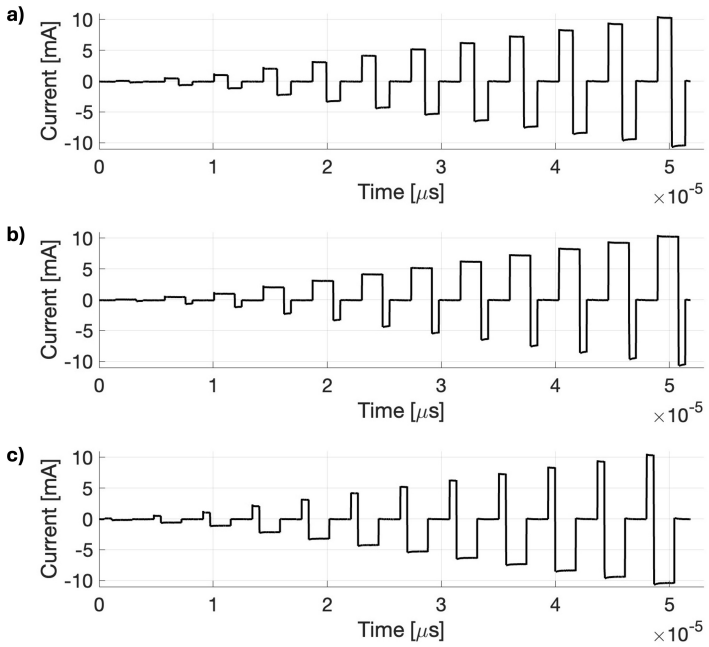

Figure 4.12: The plot shows one period for each tested stimulation pattern with increasing current amplitude (0.1, 0.5, 1, 2, 3, 4, 5, 6, 7, 8, 9, 10 mA): symmetrical pattern (A), asymmetrical pattern with a ratio of 3:1 (B), asymmetrical pattern with a ratio of 1:3 (C).

Injected Currents

Fig. 4.13 shows the stimulation pattern obtained in monophasic mode with a duty cycle of 50%. A current square wave with a frequency of 1 kHz, a duty cycle of 50%, and an amplitude ranging from 0.1 to 10 mA was recorded.

Fig. 4.14 shows the percentage relative error between the desired currents and the

measured injected currents.

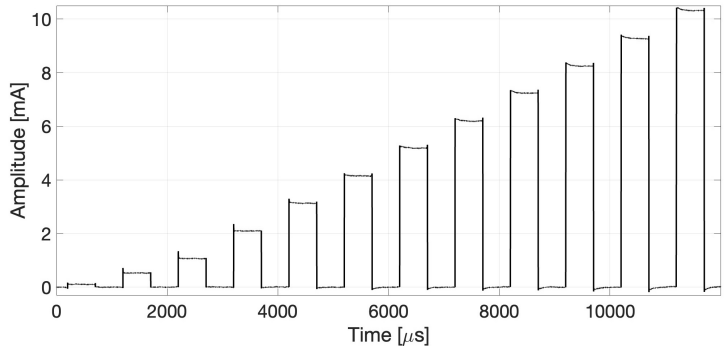

Figure 4.13: The plot shows one period for each tested stimulation pattern with increasing current amplitude (0.1, 0.5, 1, 2, 3, 4, 5, 6, 7, 8, 9, 10 mA).

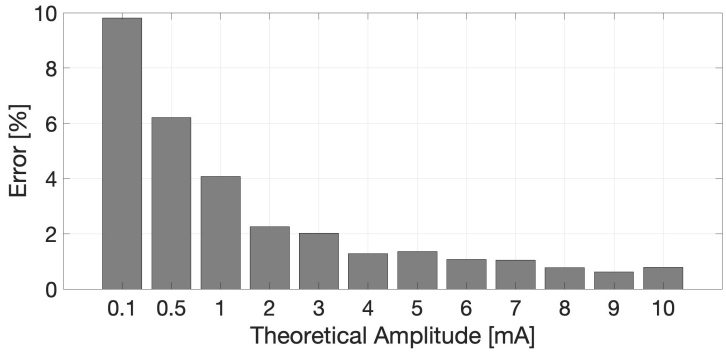

Figure 4.14: Percentage error between measured and theorical values.

Reverse Iontophoresis Scenario

Fig. 4.15 shows the concentrations of ascorbic acid measured in the upper chamber at the end of the experiment: the concentrations obtained with the stimulation protocol are significantly higher (from 5 to 8 times) than that obtained with the spontaneous process, and someway proportional to the intensity of the applied currents.

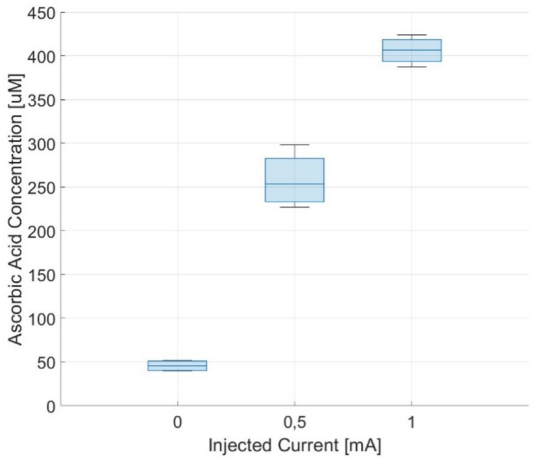

Figure 4.15: Measured concentrations of Ascorbic Acid in the receptor chamber after 30 minutes.

Table 4.1: Comparison chart of electronic interfaces for electrical stimulation found in literature.

Reference	Frequency Range	Voltage Compliance	Circuit Highlights	Safety Features
This work	Up to 50 kHz	±120 V	• VCCS • Current Mirror • H-Bridge • Single Supply	• Load grounded when idle • Continuous current monitoring
[112]	200 Hz	±200 V	• TIMER 555 • Op-amp • Transformer • Single Supply	• Continuous feedback
[113]	20–200 Hz	±160 V	• Op-amp • Darlington BJT • Transformer • Dual Supply	• Continuous feedback
[114]	Up to 50 kHz	±100 V	• VCCS • H-Bridge • Single Supply	• Continuous feedback
[115]	Up to 50 kHz	±120 V	• High Voltage Op-amp • Step-up Transformer • Dual Supply	• Load grounded when idle • Continuous current monitoring
[116]	Up to 100 Hz	±250 V	• High Voltage Op-amp • Dual Supply	• Load grounded when idle
[117]	Up to 1 kHz	±60 V	• High Voltage Op-amp • Dual Supply	• Continuous feedback

4.4 Enhancing electroosmotic flow to improve physiological diffusion of Glucose in derma layers

4.4.1 Introduction

Type 1 diabetes is a metabolic disorder characterized by elevated blood glucose levels, which can lead to serious complications such as heart disease, kidney disease, retinopathy, and neuropathy [118, 119]. The global prevalence of diabetes has risen dramatically, with over 415 million people affected worldwide. This alarming increase highlights the urgent need for effective management strategies and innovative treatment solutions [120].
The traditional capillary blood glucose meters measure the concentration of glucose from capillary blood samples obtained by the patient. This procedure, in addition to being painful and inconvenient, results in sampling a limited number of glucose values throughout the day, leaving the patient without proper monitoring during the day and especially at night, which can be quite critical in some cases.
Wearable devices for continuous self-monitoring of glucose can play a crucial role in the management of the disease. While traditional glucose meters use capillary blood, most commercial Continous Glucose Monitoring (CGM) devices measure glucose from interstitial fluid (ISF) localized in the subcutaneous adipose tissue including Freestyle Libre, Dexcom G7 (subcutaneous needle) and Eversense from Senseonics (subcutaneous sensor), which can be accessed using a minimally invasive approach. Many compounds, such as glucose, are transported from the blood into the cells via ISF [121, 122]. The glucose concentration in ISF strongly correlates with the blood glucose concentration, but the sampling of ISF non-invasively is challenging due to the barrier function of the skin. Thus, all approaches based on ISF that have reached commercial success are based on needles that penetrate the skin and reach the ISF in the dermis [123, 124]. For instance, persons with type-1 diabetes who use CGM devices are less prone to hypoglycemia (low blood sugar) and hyperglycemia (high blood sugar) [125, 126], stay longer within the target glucose range [127, 128], and have better glycated hemoglobin (HbA1c) levels.
Other approaches for non-invasive CGM under active research include sampling of the interstitial fluid with reverse ionotophoresis [129, 130, 110, 131, 132], magnetic fields [133, 134], ultrasound [135, 136], and detection of glucose through optical methods [137, 138] or radio waves [134]. Recent advancements in technology have removed the need for calibrating CGMs with fingerprick glucose measurements. However, the accuracy of all commercially available CGMs remains lowest in the hypoglycemic range, where the demand for sensitivity and specificity is critical for effectively functioning as an alarm for hypoglycemia. Both invasive and non-invasive methods for CGM face the common challenge of lag time between the concentration of glucose in ISF and in blood. The glucose concentration in the ISF, which depends on concentration differences that change

over time due to physical activities and insulin doses [139, 140], reaches about 70% of the glucose level in the blood. According to the literature [140], there is a delay of approximately 15-20 minutes in this process and is influenced by factors such as local blood flow, tissue perfusion and ISF permeability [141]. The mismatch between glucose readings from CGMs and glucose concentration in blood is of concern, particularly in the hypoglicemic range, where CGMs time lag causes CGMs glucose readings to deviate from actual glucose levels by more than 2.2 mM (40 mg/dL) in response to rapid rates of decline in glucose concentration. In the case of CGM sensors, the delay depends on various contributions, including physiological and technological factors. The physiological time delay in glucose sensing primarily arises from the time it takes for glucose to diffuse through capillary walls and the interstitial space before reaching the sensor [141]. Notably, there is significant variability in these time delays among individuals and across different CGM systems. In addition to physiological delays, technological time delays can occur and are due to calculations before the results are displayed. Another contribution of delay is related to the filtering techniques used to mitigate data noise, with reported technological delays ranging from 3 to 12 minutes [142, 143]. These delays are also attributed to glucose diffusion through protective membranes and the sensor's reaction speed, like to the enzymatic activity in the case of electrochemical glucose sensor currently used in the CGM systems, which generally accounts for an additional few minutes. Reports indicate a wide range of overall time delays, from 5 to 40 minutes, which may stem from differences in CGM systems or experimental conditions. However, much of the literature fails to address interindividual and intraindividual differences in these delays due to insufficient data. Additionally, the effects of glycemic ranges and patient-specific factors—such as physical activity—on time delays remain largely unexplored [141]. Reducing both physiological and technological time delays is essential for enhancing the accuracy and reliability of CGM systems, as these delays contribute considerably to discrepancies between CGM data and actual blood glucose values, ultimately affecting patient outcomes and timely interventions in diabetes management.

Stout et al. [144] reported a technique for the reduction of physiological lag time with modulated pressure application to enhance local blood flow. However, the current investigation is constrained by methodological limitations, including a restricted dataset and the imperative for comprehensive empirical validation to elucidate the method's reproducibility, sustained efficacy, and consistent performance across variable physiological parameters and glycemic trajectories. Another technique for enhanced blood perfusion is the use of electrical stimulation [145, 146], which further supports the idea that improving local circulation can help to reduce the lag in glucose measurements. The mechanisms underlying the enhancement of blood perfusion through electrical stimulation are supported by multiple theories. Chen et al. [147] suggest that electrical stimulation can trigger vasodilation exciting peripheral nerves and inducing blood perfusion. Instead,

Tracy et al. [148], theorized that electrical stimulation promotes blood flow as a result of the metabolic demand in the contracting muscles. Current modulation remains an hot topic in controlled drug delivery [149, 150, 151, 152] and large and small molecule extraction through reverse iontophoresis. Specifically, Terutsuki et al. [153] highlight how current modulation can offer significant advantages in drug delivery by enabling precise and controlled release mechanisms. Also combining ionophoresis with chemical enhancers, provide an helpful tool to improve skin permeability and electro-osmotic flow [154, 155, 156, 157]. In the field of extraction through reverse iontophoresis, the use of microneedles (MNs) is increasingly prevalent [158, 159, 160, 161] reducing the invasiveness of sensors for continuous glucose monitoring and improving transdermic glucose extraction. Despite reducing invasiveness, the time lag limitation remains equivalent or potentially more pronounced compared to commercially available CGM systems.

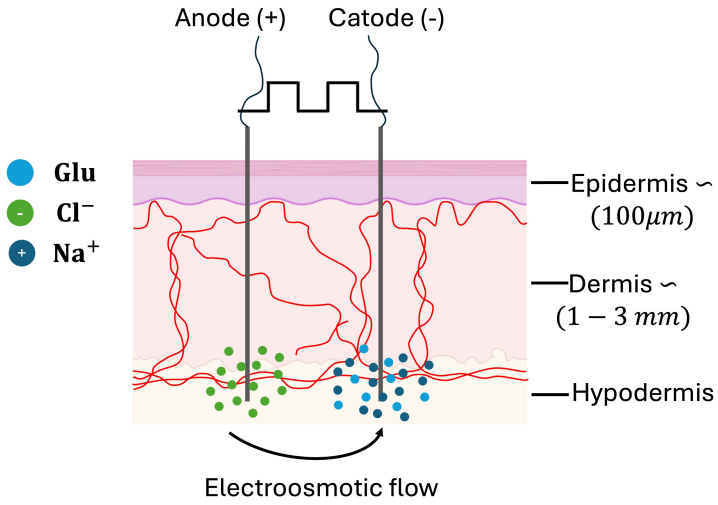

Figure 4.16: Schematic representation of glucose diffusion enhanced by intradermal electro-osmotic flow.

Considering these premises, this work [**Paper IX**] presents a microfluidic device that simulate a condition of physiological concentrations difference between the capillary blood and the ISF through a microfluidic channel, a semipermeable membrane, and a reservoir. The device was used to evaluate how the application of electric currents delivered through two electrodes influences the physiological behaviour of glucose diffusion between the two compartments. This concept hold potential to enhance the dermal electro-osmotic flow and thus improve the delay between the glucose concentration in capillaries and in the ISF due the physiological diffusion as shown in Fig. 4.16, especially pronounced in case of rapid fluctuations in glucose concentration. This technological concept seamlessly integrates with CGMs, offering potential to enhance patient outcomes.

4.4.2 Material and Methods

Computational model

The computational model was developed to investigate glucose diffusion variation between the two compartments. The model aimed to characterize the experimental conditions, geometry and parameters governing molecular transport. This model provided a starting point for modeling diffusion between the compartments, effectively translating the real dynamics of diffusion from capillary blood to interstitial fluid within a microfluidic device over a timeframe of 20 minutes.

The modeling and simulation of the developed device were conducted using COMSOL Multiphysics 6.0 software. The free and porous fluid flow, as well as the transport of diluted species and the laminar flow, was modeled to represent the behavior of the microfluidic setup. The model assumes incompressible flow conditions, with Reynolds numbers ranging from 1.67 to 8.34, confirming deeply laminar flow regime. We developed a 3D model of the geometry consisting of the 200 μm channel (1 cm length) and the reservoir, with a diameter of 6 mm. The porous polycarbonate (PC) membrane, positioned between the channel and the reservoir, was modeled with a thickness of 20 μm, as reported in the datasheet. Fluid flow from the channel through the porous membrane into the reservoir was modeled using Darcy's law, with an hydraulic permeability $k = 1.45 \times 10^{-14}\,\mathrm{m}^2$. The transport of diluted species was described by time-dependent convection-diffusion equations, with a diffusion coefficient of glucose through the membrane obtained through a parametric study based on experimental results and glucose diffusion in water of $6.7 \times 10^{-10}\,\mathrm{m}^2/\mathrm{s}$. The diffusion coefficient of the membrane was calculated through computational model considering experimental results at timepoint 20 minutes.

The concentration values within the reservoir were assessed through the volume integral relative to the reservoir, evaluating the glucose concentration in the reservoir at different time points. The laminar flow was set in the microfluidic channel to reproduce the flow conditions defined in the real setup, with the flow established from 20 μL/min to 100 μL/min using a glucose solution at a concentration of 4 mM.

Device fabrication

(i) the lower microfluidic channel was fabricated in polydimethylsiloxane (PDMS, Sylgard 184, Dow Corning), prepared by mixing the base and curing agent in a 10:1 ratio and cast by soft lithography using an SU-8 mold. The channel had a width of 200 um and was used to simulate the capillary; (ii) the upper microfluidic channel was fabricated identical to the first. A reservoir with a diameter of 6 mm was created along the microfluidic channel by punching a hole through the PDMS using a controlled-diameter punch. This upper channel was used to simulate the ISF; (iii) a commercially available polycarbonate (PC)

membrane from Whatman Cyclopore (Maidstone, UK) with a pore size of 5 um was used as an endothelial mimic layer and located at the interface between the lower microfluidic channel and the reservoir in the upper microfluidic channel. The developed and applied technique involves an optimization of the procedure reported in [162], including the use of 2% 3-aminopropyl triethoxysilane (APTES) solution, 28 % DI water and 70 % ethanol.

The bonding step was performed using an optimized version of the protocol described in [162], specifically adapted to avoid any alteration of the membrane's transport properties. As shown in Fig. 4.17 a), the membrane and the lower PDMS slab containing the microfluidic channel were first activated by oxygen plasma (200 mT, 40 sccm of O_2, 30 W, 1 min). Subsequently, as illustrated in Fig. 4.17 b), a thin layer of the APTES solution (2% APTES, 28% DI water, 70% ethanol) was applied exclusively to the non-exchange perimeter regions of the lower PDMS slab, providing localized surface functionalization to ensure a strong, leak-free bond. Importantly, the membrane surface itself was not exposed to APTES to preserve its native exchange characteristics. As shown in Fig. 4.17 c), the membrane was then placed onto the lower PDMS slab with its plasma-treated face contacting the APTES-coated perimeter zones. Finally, both the lower PDMS slab (carrying the microchannel and bonded membrane) and the upper PDMS slab containing the reservoir were plasma-treated and assembled to form the complete three-layer PDMS–membrane–PDMS structure, as depicted in Fig. 4.17 d).

Finally, the assembly was chemically bond together by a post bake at 90 °C for one hour. During the bake a weight of 200 g was applied to ensure a tight contact between the components. This process resulted in a water tight bond ensuring no leakage from the microfluidic channels.

The integration of Pt wire electrodes (diameter = 0.125 mm) was achieved via cuts made on the sides of the reservoir, and the wires were inserted to have approximately 0.9 cm of electrode in contact with the fluid in the reservoir Fig. 4.17 e). Once the electrodes were inserted and positioned at a distance of 2 mm, the cuts in the PDMS were sealed with a PDMS mortar.

Electro-diffusion device and experimental setup

Several portable and programmable devices for reverse iontophoresis have been described in the literature, mainly focusing on non-invasive monitoring and transdermal drug delivery [163, 164, 165].

The portable electronics used for electro-diffusion is a custom-made apparatus developed by the authors [166]. The system is based on a 32-bit MCU (SAM3X8E), designed for the delivery of dc current, biphasic and monophasic square wave current. The electronic interface incorporates a high-precision voltage-controlled current source coupled with a current mirror and an H-Bridge, providing a wide voltage compliance range of ±120 V to enable robust and accurate signal control. The current output range is dynamically

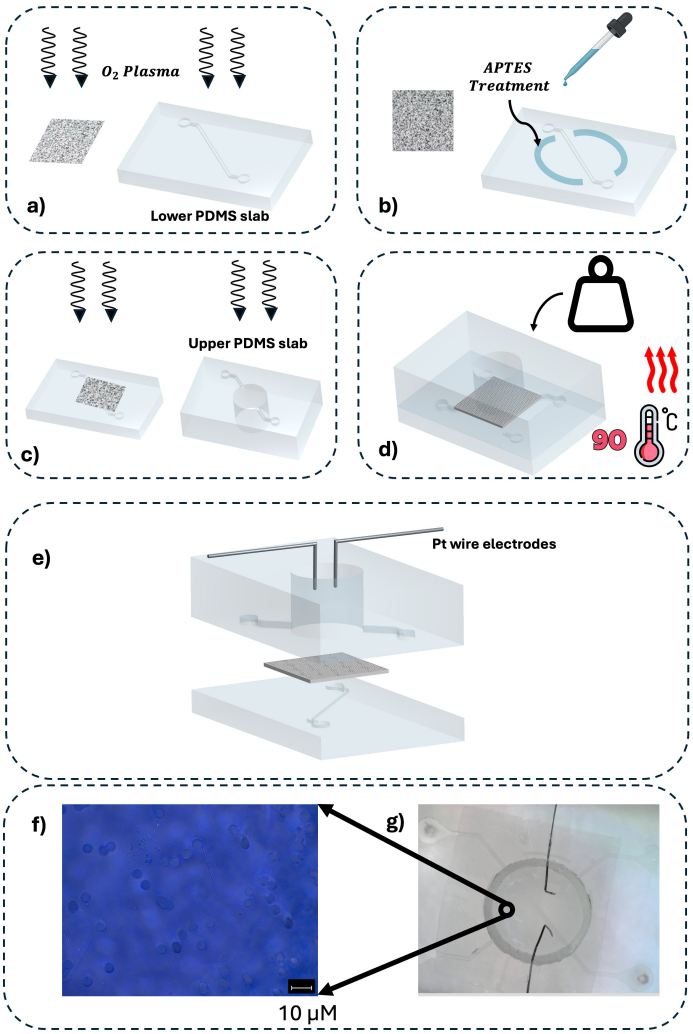

Figure 4.17: Fabrication workflow of the microfluidic device with the integration of the Pt-wire electrodes. (a) Activation of the surface with O_2 plasma treatment, respectively of the lower PDMS slab and of a face of the PC membrane; (b) APTES treatment of the lower PDMS slab in order to cross-link the PC membrane and the microfluidic channel; (c) Activation of the surface with O_2 plasma treatment, respectively of the upper PDMS slab and the lower PDMS slab; (d) Post-process thermal treatment at 90 °C for 1 h to strongly bond the sandwich chip; (e) 3D schematic illustration of the developed microfluidic chip with the integration of the Pt-wire electrodes; (f) Representative SEM images of the PC membrane; (g) Top-view image of the microfluidic developed device.

tunable through a series of selectable resistances that modulate the current gain. The system's capability to modulate frequency and duty cycle, coupled with microsecond-level timing resolution, allows for precise and flexible electrical stimulation protocols with accuracy in current and voltage parameter manipulation. Additionally, the device is designed to provide continuous monitoring of the injected current and for a safety feature to ground the load when no stimulation is being applied. Unlike voltage-controlled stimulation devices, the precise delivery of current helps to avoid undesirable effects, such as Joule heating and electrolysis, and allows for effective current control over the load. In this specific application, the device was used to deliver controlled current through two

platinum electrodes, employing direct current and square waveforms to investigate the effect of the latter on the enhancement of electro-osmotic flow. The applied current of 5 µA correspond to a current density of 140 µA/cm^2, adhering to the applicable safety current standards for patients (0.5 mA/cm^2) [167].
Considering a 0.9 cm length of the electrode in contact with the solution in the reservoir, and applying a current of 5 µA both continuously and through square wave pulses at a frequency of 500 Hz, the resulting current density is:

$$J = \frac{I}{A} = 140\,\frac{\mu A}{cm^2} \tag{4.22}$$

where:

- $I = 5\,\mu A$ is the current,
- $d = 0.125\,mm$ is the diameter,
- $l = 0.9\,cm$ is the Pt wire length,
- $A = 2\pi\left(\frac{d}{2}\right)\left(\frac{d}{2} + l\right)$ is the sum of the lateral surface and the base.

At 500 Hz, the impedance of the medium is relatively low, and with an applied current of 5 μA , the resulting voltage drop across the load is reduced. Therefore, the compliance voltage can be lowered while still allowing precise current delivery, ensuring safe operation and minimizing the risk of excessive electrode polarization or electrochemical effects.

In the case of current stimulation, the device was connected to the exposed contacts of the microfluidic device and controlled via an interface for current delivery. Concurrently, the voltage values across the load were recorded during the stimulation in order to evaluate the achieved polarization, highlighting the lower impedance encountered at high frequency and furthermore the lower voltage applied delivering the same current. The microfluidic device performance was evaluated by quantifying the transfer of glucose into the reservoir over a range of flow rates ranging from 20 µL/min to 100 µL/min and were compared to the predicted results from computational modeling. The inspected flow rates were set using a syringe pump with a 5 mL syringe containing a concentrated solution of 4 mM glucose dissolved in PBS, while the acceptor volume was filled with 80 µL of PBS. Testing different flow rates allowed us to investigate the glucose concentration in the reservoir after 20 minutes and to establish an experimental setup that replicates the diffusion of a glucose gradient of 1 mM (approximately 18 mg/dL). Once the optimal flow rate was established through systematic testing, the experiment proceeded to incorporate current stimulation to further evaluate the system's performance. This methodology allowed for a controlled simulation of physiological glucose variations between the microfluidic channel and the reservoir.

Glucose measurements

Quantitative analysis of glucose concentration was performed using the D-Glucose GOPOD FORMAT enzymatic assay kit from Megazyme Ltd. (Wicklow, Ireland). At predetermined time points, 50 µL samples were extracted from the reservoir and diluted 1:1 with PBS to achieve the 100 µL minimum volume required by the assay protocol. Following the manufacturer's instructions, the samples underwent thermal incubation at 40-50 °C for 20 minutes. Absorbance measurements were then conducted at 510 nm using a Shimadzu UV-Vis spectrophotometer to determine the final glucose concentrations.

4.5 Results & Discussions

The assembly of the device described in this paper uses a novel way of bonding the PC membranes to the two layers of PDMS. Most commonly, the used techniques include: (i) spin-coating of 1:1 ratio of toluene to PDMS onto glass followed by dipping the PDMS slabs to create a mortar for uniting the interfaces [168]; and (ii) functionalization of the membrane through a process based on APTES, [162]. However, these techniques suffer from several issues: (i) clogging of the channels due to the PDMS mortar; (ii) modification of the membrane properties through APTES treatment, which alters the diffusion characteristics of the PC membrane, leading to a reduction and instability in diffusion.
The bonding method described in the paper did not suffer from channel clogging, as no mortar-like materials were employed during the bonding procedure that could potentially obstruct the microfluidic channels.
Furthermore, membrane properties remained unaltered, since the APTES treatment was selectively applied only to surfaces not involved in fluid exchange between the reservoir and the channel.
Our bonding procedure successfully achieves strong interfacial adhesion between the three layers while crucially preserving the membrane's diffusion properties - a significant improvement over the previously reported techniques which compromised membrane functionality.

The diffusion rate was tested under three flow rate conditions: 20 μL/min, 50 μL/min, and 100 μL/min. The optimal flow rate of 50 µL/min was identified considering greater reproducibility compared to tests conducted at a flow rate of 100 μL/min, which were more significantly influenced by the higher pressure applied within the channels and on the membrane, as shown in Fig. 4.18. Furthermore, this experimental conditions allowed us to reach a glucose concentration of 1 mM in the reservoir within 20 minutes, corresponding to a change of 18 mg/dL in blood glucose levels.

The computational model has allowed for the estimation of the diffusivity coefficient

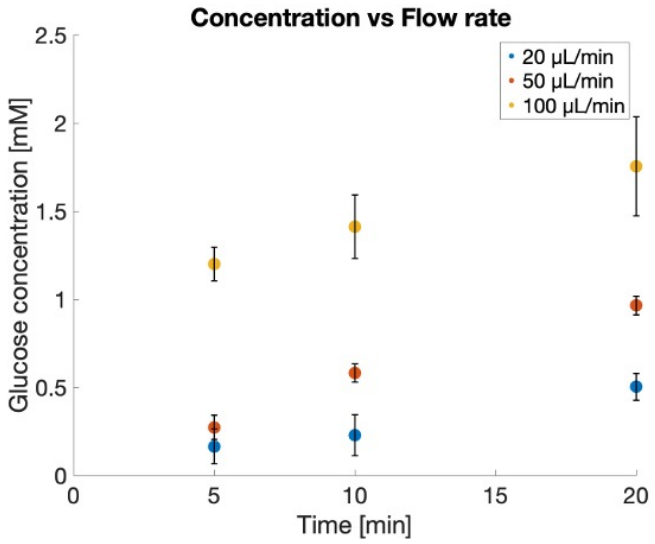

Figure 4.18: The time-course glucose concentration in the receiver chamber at different time-points for various flow rates: (i) in blue 20 μL/min; (ii) in red 50 μL/min; (iii) in yellow 100 μL/min. (N=3 independent experiments; mean ± SD)

Table 4.2: Comparative analysis of experimental measurements and computational results at 20 minutes

Flow Rate [μL/min]	**Simulated Diffusion** $[mM]$	**Experimental Diffusion** $[mM]$
20	0.43	0.50 ± 0.18
50	0.81	0.96 ± 0.05
100	1.44	1.75 ± 0.28

of glucose through the PC membrane, which is $6.0 \times 10^{-6}\,\mathrm{m}^2/\mathrm{s}$. The glucose diffusion obtained from the model within the reservoir has been evaluated at the 20-minute time point, as reported in the Table 4.2.

Subsequently, the diffusion test was repeated under current stimulation. Two stimulation patterns were applied: (i) square wave current (Fig. 4.19 in red) and (ii) DC current (Fig. 4.19 in blue) for 5 minutes. The corresponding voltage signals are shown in Fig. 4.19.

The application of an electric field enhances permeability and attracts ions in the solution toward the electrodes, which in turn facilitates the movement of neutral species, such as glucose, at physiological pH. The use of controlled square wave currents allows for lower voltage values between the electrodes due to the reduced impedance encountered at 500 Hz, as well as minimizing the Joule heating effect.

Fig. 4.20 shows the measured glucose concentration after 5 minutes under current stimulation. The diffusion achieved through DC stimulation and square wave stimulation increased of 2.8 and 3.9 times in average, respectively, compared to diffusion without stimulation.

This corresponds to a passive concentration at 5 minutes of 0.27 ± 0.07 mM, which in-

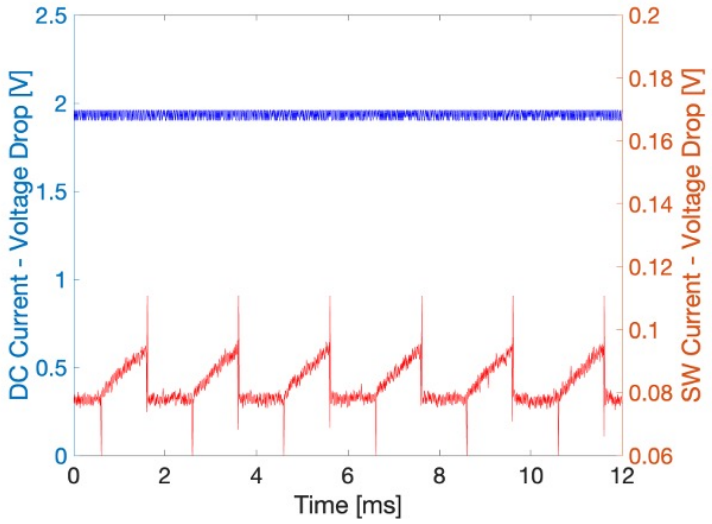

Figure 4.19: The voltage drop across the two electrodes during current-controlled electrical stimulation: in blue, the voltage at the electrodes during the application of direct current; in red, the voltage across the two electrodes during the application of the square wave current at 500 Hz, 50% duty cycle, and 5 μA amplitude.

creases to 0.75 $\pm$ 0.16 mM and 1.06 $\pm$ 0.18 mM after stimulation for DC and square wave currents, respectively. Passive diffusion required about 20 minutes to reach similar concentration as the electrically assisted diffusion after 5 minutes, which corresponds to a reduction of the diffusion lag time by 75%. Additionally, using square wave stimulation significantly reduces the polarization load, resulting in less than 100 mV stimulation voltage compared to 2 V in DC stimulation.

Based on the obtained results, it appears that pulsed current produces effects on glucose diffusion comparable to those of DC current, consistent with findings reported in literature about Na+ transport [169]. At lower frequencies (100 Hz), medium impedance is higher, leading to larger voltage drops and increased electrode polarization, which reduces net transport. At higher frequencies ($>$ 1 kHz), although the impedance of the medium decreases, capacitive effects dominate, causing a larger fraction of the current to be transferred along the electrode-solution interface rather than through the bulk. This reduces the effective electric field driving electro-osmotic flow and consequently lowers molecular transport efficiency. Frequencies in the intermediate range, such as the 500 Hz used in this study, therefore provide an optimal balance, maximizing electro-osmotic transport while minimizing electrode polarization and capacitive losses. To evaluate the stability of the electrodes under prolonged stimulation, we performed degradation tests at multiple time points (0, 3, 6, 12, and 24 h) under continuous monophasic stimulation at 5 μA. The tests were designed as a stress assessment to monitor any changes in electrode impedance over time. As shown in Fig. 4.21, the results indicate a minor increase in impedance, remaining below 400 Ω even after 24 h of continuous stimulation. These findings highlight the limited impact of sustained low-intensity current on electrode per-

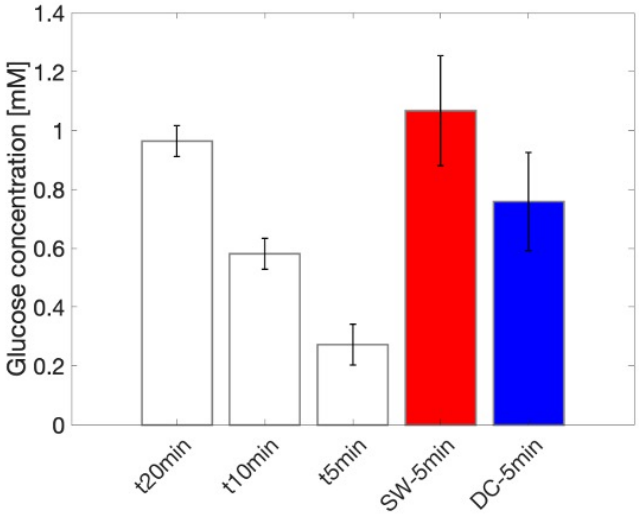

Figure 4.20: Electro-osmotic flow enhancement in diffusion dynamics: comparative analysis of diffusion mechanisms under varying applied current to enhance electro-osmotic flow. (i) In white the passive diffusion at 50 μL/min at 5,10,20 minutes (baseline reference) is reported; (ii) In red the diffusion with enhanced eletro-osmotic flow using square wave current after 5 minutes is reported; (iii) In blue the diffusion with enhanced eletro-osmotic flow using dc current after 5 minutes is reported.

formance, confirming the robustness of the system for extended operation. Furthermore, analysis of the phase module and associated errors across time points showed minimal variation, supporting the electrodes' stability during prolonged use.

These preliminary results lead to considerations about the possibility of leveraging electric stimulation to accelerate physiological diffusion in situations with sudden rate changes. These changes are triggered by insulin-related phenomena, stress and physical activity, where sensor response becomes critically important for patients, especially for making compensatory clinical decisions. The delay phenomena, caused by physiological diffusion lag and technological delay, can be minimized to reduce the time gap between capillary concentration and ISF concentration. Moreover, the technological delay persists in the measurement delay contribution due both to the response times of the enzymatic sensor and to the computational times. This delay contribution can be reduced by introducing a non-enzymatic glucose sensor to construct a fully robust system [170, 171, 172, 173, 174].

Although the proposed microfluidic platform provides a controlled and reproducible environment to investigate magnitude gradient of glucose transport, it represents a simplified model of the complex architecture of the dermal interstitial space diffusion. In particular, static reservoirs and the polycarbonate membrane do not fully reproduce the heterogeneous extracellular matrix present in vivo, which includes collagen networks, binding proteins, and cellular components that influence diffusion and fluid dynamics. These structural and biochemical features are not captured in the current model, constituting

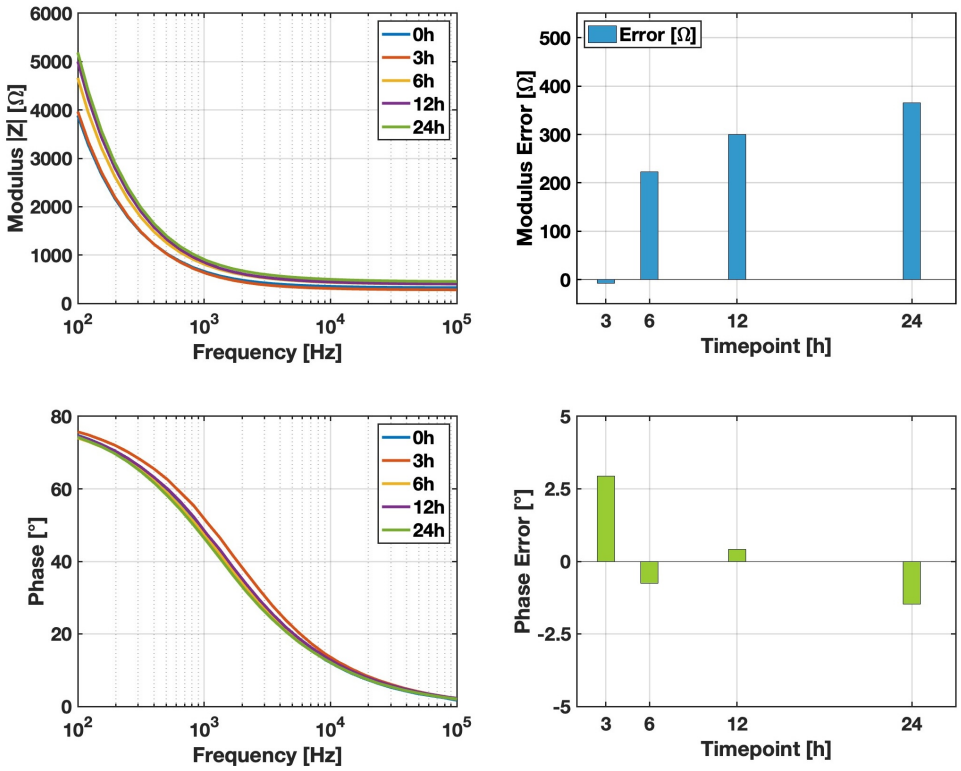

Figure 4.21: Impedance stability of electrodes under continuous stimulation. Measurements of modulus and phase were performed at 0, 3, 6, 12, and 24 h of continuous monophasic stimulation at 5 μA. The reported errors represent the differences (Δ) relative to the values of modulus and phase at the 0 h timepoint.

an intrinsic limitation.

However, it is important to note that the primary objective of this study was not to fully replicate the in vivo dermal environment, but rather to validate the concept that low-intensity electrical stimulation can enhance glucose transport across a defined barrier. These simplified system allows precise control over experimental variables and the isolation of electro-osmotic effects without confounding factors from cellular metabolism or matrix complexity.

Moreover, the diffusion delays measured in our system under passive conditions are within the range reported in continuous glucose monitoring studies (15–20 minutes), supporting the translational relevance of the model. For future work, more physiologically representative platforms could include collagen-based hydrogels with cellular components, which would better mimic the mechanical, tortuous, and reactive nature of the interstitial space. Despite these simplifications, the present in-vitro model effectively demonstrates the potential of pulsed electrical currents to accelerate glucose transport, providing a foundation for future bioengineered systems.

4.6 Summary and Future Perspectives

This chapter reviewed the principles, techniques, and system design considerations for electrical stimulation, with a focus on iontophoresis (IP) and reverse iontophoresis (RI) applications. Key topics included electrode configurations, electrode–skin interface modeling, charge delivery methods, waveform design, and safety considerations. Both monopolar and bipolar electrode arrangements were discussed, along with lumped-element models capturing the resistive and capacitive properties of the skin and underlying tissues.

Charge delivery strategies, including constant-current stimulation (CCS) and constant-voltage stimulation (CVS), were analyzed. CCS was highlighted as the preferred approach for clinical applications due to its ability to maintain consistent current despite impedance variations, ensuring precise and safe delivery of electrical charge. Charge-balanced waveforms, including biphasic and monophasic pulses with passive discharge, were emphasized to minimize tissue irritation, electrode degradation, and safety risks. Stimulation parameters such as amplitude, phase duration, frequency, and interphase delay were discussed with reference to their influence on muscle contraction and physiological safety limits. The chapter presented a versatile high-voltage current stimulator suitable for RI applications, supporting programmable monophasic and biphasic pulses with amplitudes from 0.1 to 10 mA and real-time current monitoring, achieving maximum errors of about 10% at low intensities. Using this same stimulator, the physiological lag between capillary blood and interstitial fluid in glucose transport was significantly reduced. Specifically, a low current density of 140 $\mu A/cm^2$ decreased diffusion time by 75%, from 20 minutes to 5 minutes, while square-wave stimulation demonstrated comparable performance to DC stimulation with reduced Joule heating and lower electrode potentials. These results highlight the importance of programmable waveform control and low-intensity stimulation for both safety and enhanced transport efficiency. Overall, these studies demonstrate that careful control of stimulation parameters, waveform design, and electrode interface management can significantly improve the efficacy, safety, and responsiveness of both therapeutic and diagnostic electrical stimulation systems. Future directions include integrating compact, low-power stimulators with advanced feedback and monitoring systems for wearable or implantable applications. Hybrid solutions combining electrical stimulation with microfluidics, microneedles, or biosensing platforms are expected to enhance transport efficiency and sensor responsiveness. Adaptive and programmable waveform control may further improve safety, energy efficiency, and personalized operation. Such advancements will enable real-time, minimally invasive monitoring of molecular or ionic transport, broadening the clinical and research applications of electrical stimulation, from glucose sensing to drug delivery and neuromuscular rehabilitation.

Chapter 5

Conclusions and future work

The growing interest in personalized and continuous healthcare monitoring has driven the development of portable and wearable biomedical systems that combine precision, miniaturization, and low power consumption. This thesis contributed to this field by designing and implementing three distinct hardware platforms addressing different but complementary biomedical functions: a portable and low-cost potentiostat for electrochemical sensing, optimized circuits and portable devices for bio-impedance spectroscopy, and a programmable electrical stimulator. Each subsystem was conceived, designed, and validated independently, providing new insights and design methodologies for next-generation medical and research instrumentation.

The first contribution consisted of the design of a portable potentiostat for electrochemical biosensing. The proposed system was optimized for wearable and point-of-care applications, achieving low noise, high precision, and reduced power consumption. The analog front-end and current generation circuits were designed to maintain signal integrity across a wide range of analyte concentrations and electrochemical conditions. Experimental validation confirmed the potentiostat's reliability for amperometric and voltammetric measurements, demonstrating its potential for integration with flexible and miniaturized chemical sensors for continuous health monitoring.

The second part of this work focused on developing bio-impedance spectroscopy interfaces optimized for high accuracy, fast measurement, and wide frequency coverage. The implemented architectures introduced techniques such as frequency-division phase detection, dynamic gain control, and adaptive digital sampling to enhance precision and robustness while reducing sampling rate and memory requirements through optimized clock control. Experimental results demonstrated accurate magnitude and phase estimation up to the megahertz range, confirming competitive performance with state-of-the-art systems and establishing a solid basis for future portable and wearable impedance sensing applications.

The third contribution involved the design of a programmable electrical stimulator intended for medical applications. The stimulator was implemented with a current-

controlled output stage, programmable waveform generation, and integrated safety features, allowing precise delivery of biphasic and monophasic stimulation pulses. Measurement results demonstrated high output accuracy, low distortion, and robust operation across various load conditions. This platform can support research on eletrical stimulation, reverse iontophoresis and drug delivery applications.

Although the three systems developed in this thesis were conceived as independent platforms, together they establish a coherent technological framework for future multimodal bioelectronic devices. Their complementary functionalities—electrochemical sensing, impedance analysis, and electrical stimulation—can be leveraged in future research to create integrated, closed-loop systems capable of simultaneous physiological monitoring and feedback-based stimulation.

Future developments will focus on extending and consolidating these results along several directions:

- **System-level integration:** Design unified hardware and software architectures combining the potentiostat, impedance measurement interface, and stimulator within a single synchronized platform, enabling parameter customization for specific applications.
- **Embedded intelligence:** Implement real-time signal processing, feature extraction, and adaptive control algorithms to automate sensing and stimulation tasks while optimizing power and performance.
- **ASIC integration:** Investigate the monolithic integration of the potentiostat, impedance measurement interface, and stimulator within a single ASIC to minimize form factor, reduce parasitics, and improve energy efficiency, while enabling application-specific co-design of analog and digital subsystems.
- **Experimental validation:** Extend validation to complex measurement scenarios and multi-modal operation to assess cross-interactions, synchronization accuracy, and long-term stability.

In summary, this thesis presented the design and validation of three independent yet complementary biomedical hardware platforms, each addressing a key aspect of portable healthcare instrumentation. While developed separately, these systems collectively provide a solid foundation for future integration into compact, intelligent, and adaptable bioelectronic platforms for advanced physiological monitoring and closed-loop control.

Bibliography

[1] Jayoung Kim, Alan S Campbell, Berta Esteban-Fernández de Ávila, and Joseph Wang. "Wearable biosensors for healthcare monitoring". In: *Nature biotechnology* 37.4 (2019), pp. 389–406.

[2] Jayoung Kim, Juliane R Sempionatto, Somayeh Imani, Martin C Hartel, Abbas Barfidokht, Guangda Tang, Alan S Campbell, Patrick P Mercier, and Joseph Wang. "Simultaneous monitoring of sweat and interstitial fluid using a single wearable biosensor platform". In: *Advanced Science* 5.10 (2018), p. 1800880.

[3] Xichen Yuan, Oumaima Ouaskioud, Xu Yin, Chen Li, Pengyi Ma, Yang Yang, Peng-Fei Yang, Li Xie, and Li Ren. "Epidermal wearable biosensors for the continuous monitoring of biomarkers of chronic disease in interstitial fluid". In: *Micromachines* 14.7 (2023), p. 1452.

[4] Y. Cheng, X. Gong, J. Yang, G. Zheng, Y. Zheng, Y. Li, Y. Xu, G. Nie, X. Xie, L. Jiang, et al. "A touch-actuated glucose sensor fully integrated with microneedle array and reverse iontophoresis for diabetes monitoring". In: *Biosensors and Bioelectronics* 203 (2022), p. 114026.

[5] Haowei Duan, Shuhua Peng, Shuai He, Shi-Yang Tang, Keisuke Goda, Chun H Wang, and Ming Li. "Wearable electrochemical biosensors for advanced healthcare monitoring". In: *Advanced Science* 12.2 (2025), p. 2411433.

[6] Saeed Takaloo and Mahdi Moghimi Zand. "Wearable electrochemical flexible biosensors: With the focus on affinity biosensors". In: *Sensing and Bio-Sensing Research* 32 (2021), p. 100403.

[7] Xiaohu Liu, Ying Ye, Yuancai Ge, Jia Qu, Bo Liedberg, Qingwen Zhang, and Yi Wang. "Smart contact lenses for healthcare monitoring and therapy". In: *ACS nano* 18.9 (2024), pp. 6817–6844.

[8] Noé Brasier, Joseph Wang, Wei Gao, Juliane R Sempionatto, Can Dincer, H Ceren Ates, Firat Güder, Selin Olenik, Ivo Schauwecker, Dietmar Schaffarczyk, et al. "Applied body-fluid analysis by wearable devices". In: *Nature* 636.8041 (2024), pp. 57–68.

[9] Hossein Chenani, Mohsen Saeidi, MahsaSadat Adel Rastkhiz, Nafiseh Bolghanabadi, Amir Hossein Aghaii, Mina Orouji, Amir Hatamie, and Abdolreza Simchi. "Challenges and advances of hydrogel-based wearable electrochemical biosensors for real-time monitoring of biofluids: from lab to market. A review". In: *Analytical Chemistry* 96.20 (2024), pp. 8160–8183.

[10] Yichen Chen, Biao Ma, Yinxiu Zuo, Gangsheng Chen, Qing Hao, Chao Zhao, and Hong Liu. "Versatile sweat bioanalysis on demand with hydrogel-programmed wearables". In: *Biosensors and Bioelectronics* 235 (2023), p. 115412.

[11] Tahir Raza, Lijun Qu, Waquar Ahmed Khokhar, Boakye Andrews, Afzal Ali, and Mingwei Tian. "Progress of wearable and flexible electrochemical biosensors with the aid of conductive nanomaterials". In: *Frontiers in Bioengineering and Biotechnology* 9 (2021), p. 761020.

[12] Junlong Ma, Siyi Yang, Zhihao Yang, Ziliang He, and Zhanhong Du. "Functional nanomaterials for advanced bioelectrode interfaces: recent advances in disease detection and metabolic monitoring". In: *Sensors* 25.14 (2025), p. 4412.

[13] Tianming Zhao, Yongming Fu, Chuxiao Sun, Xishan Zhao, Chunxiao Jiao, An Du, Qi Wang, Yupeng Mao, and Baodan Liu. "Wearable biosensors for real-time sweat analysis and body motion capture based on stretchable fiber-based triboelectric nanogenerators". In: *Biosensors and Bioelectronics* 205 (2022), p. 114115.

[14] Richard G Compton and Giles HW Sanders. *Electrode potentials*. PUBDB-2024-04902. Oxford University Press, 1996.

[15] Samuel P Kounaves. "Voltammetric techniques". In: *Handbook of instrumental techniques for analytical chemistry* (1997), pp. 709–726.

[16] A Bott. "Practical problems in voltammetry 3: reference electrodes for voltammetry". In: *Current Separations* 14 (1995), pp. 64–69.

[17] Peter T Kissinger and William R Heineman. "Cyclic voltammetry". In: *Journal of chemical education* 60.9 (1983), p. 702.

[18] Bhaskar R Sathe, Beena K Balan, and Vijayamohanan K Pillai. "Enhanced electrocatalytic performance of interconnected Rh nano-chains towards formic acid oxidation". In: *Energy & Environmental Science* 4.3 (2011), pp. 1029–1036.

[19] Noémie Elgrishi, Kelley J Rountree, Brian D McCarthy, Eric S Rountree, Thomas T Eisenhart, and Jillian L Dempsey. "A practical beginner's guide to cyclic voltammetry". In: *Journal of chemical education* 95.2 (2018), pp. 197–206.

[20] Allen J Bard, Larry R Faulkner, and Henry S White. *Electrochemical methods: fundamentals and applications*. John Wiley & Sons, 2022.

[21] Wm Cameron Chumlea and Shumei S Guo. "Bioelectrical impedance: a history, research issues, and recent consensus". In: *Emerging technologies for nutrition research Potential for assessing military performance capability* (1997), pp. 169–192.

[22] Leigh C Ward. "Electrical bioimpedance: from the past to the future". In: *Journal of electrical bioimpedance* 12.1 (2021), p. 1.

[23] Arthur P DeMarzo. "Clinical use of impedance cardiography for hemodynamic assessment of early cardiovascular disease and management of hypertension". In: *High Blood Pressure & Cardiovascular Prevention* 27.3 (2020), pp. 203–213.

[24] Adriano R Tonelli, Hassan Alnuaimat, Ning Li, Robin Carrie, and Kamal K Mubarak. "Value of impedance cardiography in patients studied for pulmonary hypertension". In: *Lung* 189.5 (2011), pp. 369–375.

[25] Alicia Everitt, Brandon Root, Daniel Calnan, Preston Manwaring, David Bauer, and Ryan Halter. "A bioimpedance-based monitor for real-time detection and identification of secondary brain injury". In: *Scientific Reports* 11.1 (2021), p. 15454.

[26] Christopher Hawthorne, Martin Shaw, Ian Piper, Laura Moss, and John Kinsella. "Transcranial bioimpedance measurement as a non-invasive estimate of intracranial pressure". In: *Intracranial Pressure & Neuromonitoring XVI*. Springer, 2018, pp. 89–92.

[27] Leigh C Ward. "Bioelectrical impedance analysis for body composition assessment: reflections on accuracy, clinical utility, and standardisation". In: *European journal of clinical nutrition* 73.2 (2019), pp. 194–199.

[28] Andy Adler and Alistair Boyle. "Electrical impedance tomography: Tissue properties to image measures". In: *IEEE Transactions on Biomedical Engineering* 64.11 (2017), pp. 2494–2504.

[29] Yu Wu, Farnaz Fahimi Hanzaee, Dai Jiang, Richard H Bayford, and Andreas Demosthenous. "Electrical impedance tomography for biomedical applications: Circuits and systems review". In: *IEEE Open Journal of Circuits and Systems* 2 (2021), pp. 380–397.

[30] Giacinto Luigi Cerone, Alessandra Giangrande, Taian Vieira, Domenico Pisaturo, Mihai Ionescu, Marco Gazzoni, and Alberto Botter. "Design of a programmable and modular neuromuscular electrical stimulator integrated into a wireless body sensor network". In: *IEEE Access* 9 (2021), pp. 163284–163296.

[31] Ali Imam Sunny, Mohammed Rahman, Maria Koutsoupidou, Helena Cano-Garcia, Maya Thanou, Waqas Rafique, Oliver Lipscombe, Panagiotis Kassanos, Iasonas Triantis, Efthymios Kallos, et al. "Feasibility experiments to detect skin hydration using a bio-impedance sensor". In: *2019 41st Annual International Conference*

of the IEEE Engineering in Medicine and Biology Society (EMBC). IEEE. 2019, pp. 6032–6035.

[32] Xian Huang, Huanyu Cheng, Kaile Chen, Yilin Zhang, Yihui Zhang, Yuhao Liu, Chenqi Zhu, Shao-chi Ouyang, Gil-Woo Kong, Cunjiang Yu, et al. "Epidermal impedance sensing sheets for precision hydration assessment and spatial mapping". In: *IEEE transactions on biomedical engineering* 60.10 (2013), pp. 2848–2857.

[33] Gargi S Sarode, Sachin C Sarode, Meena Kulkarni, Swarada Karmarkar, and Shankargouda Patil. "Role of bioimpedance in cancer detection: A brief review". In: *International Journal of Dental Science and Research* 3.1 (2016), pp. 15–21.

[34] RJ Strand-Amundsen, C Tronstad, H Kalvøy, Y Gundersen, CD Krohn, AO Aasen, L Holhjem, HM Reims, Ø G Martinsen, JO Høgetveit, et al. "In vivo characterization of ischemic small intestine using bioimpedance measurements". In: *Physiological Measurement* 37.2 (2016), p. 257.

[35] Fritz Mellert, Kai Winkler, Christian Schneider, Taras Dudykevych, Armin Welz, Markus Osypka, Eberhard Gersing, and Claus J Preusse. "Detection of (reversible) myocardial ischemic injury by means of electrical bioimpedance". In: *IEEE Transactions on Biomedical Engineering* 58.6 (2010), pp. 1511–1518.

[36] Hang Wang, Yong He, Qingguo Yan, Fusheng You, Feng Fu, Xiuzhen Dong, Xuetao Shi, and Min Yang. "Correlation between the dielectric properties and biological activities of human ex vivo hepatic tissue". In: *Physics in Medicine & Biology* 60.6 (2015), p. 2603.

[37] Atte Kekonen, Mikael Bergelin, Jan-Erik Eriksson, Annikki Vaalasti, Heimo Yläanen, and Jari Viik. "Bioimpedance measurement based evaluation of wound healing". In: *Physiological Measurement* 38.7 (2017), p. 1373.

[38] Sinan Hersek, Hakan Töreyin, and Omer T Inan. "A robust system for longitudinal knee joint edema and blood flow assessment based on vector bioimpedance measurements". In: *IEEE Transactions on biomedical circuits and systems* 10.3 (2015), pp. 545–555.

[39] Tim Süselbeck, Hagen Thielecke, Ines Weinschenk, Alexandra Reininger-Mack, Thomas Stieglitz, Jürgen Metz, Martin Borggrefe, Andrea Robitzki, and Karl K Haase. "In vivo intravascular electric impedance spectroscopy using a new catheter with integrated microelectrodes". In: *Basic research in cardiology* 100.1 (2005), pp. 28–34.

[40] Jang-Zern Tsai, James A Will, Scott Hubbard-Van Stelle, Hong Cao, Supan Tungjitkusolmun, Young Bin Choy, Dieter Haemmerich, Vicken R Vorperian, and John G Webster. "In-vivo measurement of swine myocardial resistivity". In: *IEEE Transactions on Biomedical Engineering* 49.5 (2002), pp. 472–483.

[41] Philipp Aebischer, Stefan Meyer, Marco Caversaccio, and Wilhelm Wimmer. "Intraoperative impedance-based estimation of cochlear implant electrode array insertion depth". In: *IEEE transactions on biomedical engineering* 68.2 (2020), pp. 545–555.

[42] Juan Ansó, Thomas W Balmer, Yves Jegge, Håvard Kalvoy, Brett J Bell, Cilgia Dür, Enric M Calvo, Tom M Williamson, Nicolas Gerber, Damien Ferrario, et al. "Electrical impedance to assess facial nerve proximity during robotic cochlear implantation". In: *IEEE transactions on biomedical engineering* 66.1 (2018), pp. 237–245.

[43] Ruben Van den Eeckhoudt, An-Sofie Christiaens, Frederik Ceyssens, Vasileios Vangalis, Kevin J Verstrepen, Nico Boon, Filip Tavernier, Michael Kraft, and Irene Taurino. "Full-electric microfluidic platform to capture, analyze and selectively release single cells". In: *Lab on a Chip* 23.19 (2023), pp. 4276–4286.

[44] Uwe Pliquett. "Bioimpedance: a review for food processing". In: *Food engineering reviews* 2.2 (2010), pp. 74–94.

[45] Sverre Grimnes and Ørjan G Martinsen. "Bioimpedance Measurements". In: *Medical Devices and Human Engineering (The Biomedical Engineering Handbook, Fourth Edition)* (2015).

[46] Orjan G Martinsen and Arto Heiskanen. *Bioimpedance and bioelectricity basics*. Elsevier, 2023.

[47] Sami Gabriel, RW Lau, and Camelia Gabriel. "The dielectric properties of biological tissues: II. Measurements in the frequency range 10 Hz to 20 GHz". In: *Physics in medicine & biology* 41.11 (1996), p. 2251.

[48] Jiawei Xu, Srinjoy Mitra, Chris Van Hoof, Refet Firat Yazicioglu, and Kofi AA Makinwa. "Active electrodes for wearable EEG acquisition: Review and electronics design methodology". In: *IEEE reviews in biomedical engineering* 10 (2017), pp. 187–198.

[49] Yu Mike Chi, Tzyy-Ping Jung, and Gert Cauwenberghs. "Dry-contact and noncontact biopotential electrodes: Methodological review". In: *IEEE reviews in biomedical engineering* 3 (2010), pp. 106–119.

[50] D. Pratticò, F. Laganà, G. Oliva, A. Fiorillo, S. Pullano, S. Calcagno, D. De Carlo, and F. La Foresta. "Integration of LSTM and U-Net Models for Monitoring Electrical Absorption With a System of Sensors and Electronic Circuits". In: *IEEE Transactions on Instrumentation and Measurement* 74 (2025), pp. 1–11.

[51] B. Liu, G. Wang, Y. Li, L. Zeng, H. Li, Y. Gao, Y. Ma, Y. Lian, and C. Heng. "A 13-channel 1.53-mW 11.28-mm^2 electrical impedance tomography SoC based on frequency division multiplexing for lung physiological imaging". In: *IEEE Trans. Biomed. Circuits Syst.* 13 (2019), pp. 938–949.

[52] J. Lee, S. Gweon, K. Lee, S. Um, K. Lee, and H. Yoo. "A 9.6-mW/Ch 10-MHz wide-bandwidth electrical impedance tomography IC with accurate phase compensation for early breast cancer detection". In: *IEEE Journal of Solid-State Circuits* 56 (2020), pp. 887–898.

[53] H. Ko, T. Lee, J. Kim, J. Park, and J. Kim. "Ultralow-power bioimpedance IC with intermediate frequency shifting chopper". In: *IEEE Transactions on Circuits and Systems II: Express Briefs* 63 (2015), pp. 259–263.

[54] H. Ha, M. Konijnenburg, B. Lukita, R. Van Wegberg, J. Xu, R. Hoven, M. Lemmens, R. Thoelen, C. Van Hoof, and N. Van Helleputte. "A bio-impedance readout IC with frequency sweeping from 1k-to-1MHz for electrical impedance tomography". In: *2017 Symposium on VLSI Circuits*. 2017, pp. C174–C175.

[55] H. Huang and S. Palermo. "A TDC-based front-end for rapid impedance spectroscopy". In: *2013 IEEE 56th International Midwest Symposium on Circuits and Systems (MWSCAS)*. 2013, pp. 169–172.

[56] G. Qiao, W. Wang, W. Duan, F. Zheng, A. Sinclair, and C. Chatwin. "Bioimpedance analysis for the characterization of breast cancer cells in suspension". In: *IEEE Transactions on Biomedical Engineering* 59 (2012), pp. 2321–2329.

[57] T. Freeborn and G. Bohannan. "Changes of fractional-order model parameters in biceps tissue from fatiguing exercise". In: *2018 IEEE International Symposium on Circuits and Systems (ISCAS)*. 2018, pp. 1–5.

[58] X. Xu, T. Rioux, and M. Castellani. "The specific heat of the human body is lower than previously believed: The Journal Temperature toolbox". In: *Temperature* 10 (2023), pp. 235–239.

[59] International Commission on Non-Ionizing Radiation Protection (ICNIRP). "Guidelines for limiting exposure to time-varying electric, magnetic, and electromagnetic fields (up to 300 GHz)". In: *Health Physics* 74 (1998), pp. 494–522.

[60] IEEE Standards Association. *IEEE standard for safety levels with respect to human exposure to electric, magnetic, and electromagnetic fields, 0 Hz to 300 GHz*. 2019.

[61] P. Kassanos, L. Constantinou, I. Triantis, and A. Demosthenous. "An integrated analog readout for multi-frequency bioimpedance measurements". In: *IEEE Sensors Journal* 14 (2014), pp. 2792–2800.

[62] P. Kassanos, I. Triantis, and A. Demosthenous. "A CMOS magnitude/phase measurement chip for impedance spectroscopy". In: *IEEE Sensors Journal* 13 (2013), pp. 2229–2236.

[63] S. Cheon, S. Kweon, Y. Kim, J. Koo, S. Ha, and M. Je. "A polar-demodulation-based impedance-measurement IC using frequency-shift technique with low power consumption and wide frequency range". In: *IEEE Transactions on Biomedical Circuits and Systems* 15 (2021), pp. 1210–1220.

[64] S. Kweon, S. Shin, J. Park, J. Suh, and H. Yoo. "A CMOS low-power polar demodulator for electrical bioimpedance spectroscopy using adaptive self-sampling schemes". In: *2016 IEEE Biomedical Circuits and Systems Conference (BioCAS)*. 2016, pp. 284–287.

[65] Y. Wu, D. Jiang, M. Habibollahi, N. Almarri, and A. Demosthenous. "Time stamp–a novel time-to-digital demodulation method for bioimpedance implant applications". In: *IEEE Transactions on Biomedical Circuits and Systems* 14 (2020), pp. 997–1007.

[66] S. Cheon, S. Kweon, Y. Kim, J. Koo, S. Ha, and M. Je. "An impedance readout IC with ratio-based measurement techniques for electrical impedance spectroscopy". In: *Sensors* 22 (2022), p. 1563.

[67] Lorenzo A Buscaglia, João Paulo Carmo, and Osvaldo N Oliveira. "Simple-Z: a low-cost portable impedance analyzer". In: *IEEE Sensors Journal* 23.21 (2023), pp. 26067–26074.

[68] P. Li, S. Xu, D. Xu, and C. Xu. "Structural Health Monitoring of an Aircraft Wing Using a Portable Wireless Electro-Mechanical Impedance Analyzer". In: *IEEE Sensors Journal* (2024).

[69] Z. Hu, A. Kallel, T. Lu, A. Al-Hamry, and O. Kanoun. "An Auto-calibrated Measurement System for One-dimensional Matrices of Impedimetric Sensors". In: *IEEE Sensors Journal* (2024).

[70] K. Ain, R. Wibowo, S. Soelistiono, L. Muniroh, and B. Ariwanto. "Design and development of a low-cost Arduino-based electrical BioImpedance Spectrometer". In: *Journal of Medical Signals & Sensors* 10 (2020), pp. 125–133.

[71] K. Ain, F. Chandra, and R. Rulaningtyas. "Development of multi-frequency electrical impedance device based on AD9850 module". In: *AIP Conference Proceedings*. Vol. 2314. 2020.

[72] K. Ain, F. Chandra, Q. Zaka, B. Fahrani, A. Amelia, A. Enggar, R. Rulaningtyas, L. Muqmiroh, and B. Ariwanto. "Design of Bioimpedance Spectroscopy to Characterize Meat Based on Gain and Phase Detector (AD8302)". In: *2021 International Conference on Instrumentation, Control, and Automation (ICA)*. 2021, pp. 55–59.

[73] D. Santoso, B. Pitaloka, C. Widodo, and U. Juswono. “Low-cost, compact, and rapid bio-impedance spectrometer with real-time Bode and Nyquist plots”. In: *Applied Sciences* 10 (2020), p. 878.

[74] A. Zompanti, R. Cicco, D. Ciarrocchi, M. Santonico, and G. Pennazza. “Design, realization and test of a low-cost electrical impedance spectroscopy analyzer for biological samples”. In: *2023 9th International Workshop on Advances in Sensors and Interfaces (IWASI)*. 2023, pp. 86–90.

[75] Davide Ciarrocchi, Alessandro Zompanti, Marco Santonico, and Giorgio Pennazza. “A Novel Polar-Demodulator-Based Electronic Interface for Bioimpedance Spectroscopy with Enhanced Phase Detection and Reduced Dead Zone”. In: *IEEE Transactions on Instrumentation and Measurement* (2025).

[76] Zoltan Vizvari, Mihaly Klincsik, Peter Odry, Vladimir Tadic, Nina Gyorfi, Attila Toth, and Zoltan Sari. “Continuous Electrode Models and Application of Exact Schemes in Modeling of Electrical Impedance Measurements”. In: *Electronics* 13.1 (2023), p. 66.

[77] Liangtao Yang, Lu Gan, Zhenggang Zhang, Zhilin Zhang, Hui Yang, Yi Zhang, and Jinglong Wu. “Insight into the contact impedance between the electrode and the skin surface for electrophysical recordings”. In: *ACS omega* 7.16 (2022), pp. 13906–13912.

[78] Konrad Chabowski, Tomasz Piasecki, Andrzej Dzierka, and Karol Nitsch. “Simple wide frequency range impedance meter based on AD5933 integrated circuit”. In: *Metrology and Measurement Systems* 22.1 (2015).

[79] Yuxiang Yang, Jue Wang, Gang Yu, Feilong Niu, and Ping He. “Design and preliminary evaluation of a portable device for the measurement of bioimpedance spectroscopy”. In: *Physiological Measurement* 27.12 (2006), p. 1293.

[80] Henry Crandall, A Burt, and Benjamin Sanchez. “Characterization of the analog device inc (ADI) MAX30009 bioimpedance analog front end chip”. In: *2022 44th Annual International Conference of the IEEE Engineering in Medicine & Biology Society (EMBC)*. IEEE. 2022, pp. 2502–2505.

[81] Ngoc-Luan Tran, Ngoc-Quan Ha-Phan, Thien-Luan Phan, Congo Tak Shing Ching, and Minh-Khue Ha. “Design and Implementation of a Cost-Effective, Portable Impedance Analyzer Device with AD5941”. In: *IEEJ Transactions on Electrical and Electronic Engineering* 19.10 (2024), pp. 1730–1736.

[82] Salvador Meléndez Muñoz, Emilio Silvestre Mérida, Santiago J Fernández Scagliusi, Andreea M Oprescu, Antonio Algarín Pérez, and Pablo Pérez García. “Design and Implementation of a Smart AC Current Source for Impedance Spectroscopy Using ARM Microcontrollers”. In: *Electronics* 13.23 (2024), p. 4805.

[83] Antonio Bandur, Delaram Sadatamin, Bryan Piper, Ivana Culjak, Hrvoje Dzapo, and Azadeh Yadollahi. "Designing a Wearable Wireless System for Real-time Bioimpedance Spectroscopy of Body Fluid". In: *2023 IEEE Biomedical Circuits and Systems Conference (BioCAS)*. IEEE. 2023, pp. 1–5.

[84] Alexandros Ch Lazanas and Mamas I Prodromidis. "Electrochemical impedance spectroscopy a tutorial". In: *ACS measurement science au* 3.3 (2023), pp. 162–193.

[85] Ursula G Kyle, Ingvar Bosaeus, Antonio D De Lorenzo, Paul Deurenberg, Marinos Elia, José Manuel Gómez, Berit Lilienthal Heitmann, Luisa Kent-Smith, Jean-Claude Melchior, Matthias Pirlich, et al. "Bioelectrical impedance analysis—part I: review of principles and methods". In: *Clinical nutrition* 23.5 (2004), pp. 1226–1243.

[86] Leigh C Ward, Julia M Dyer, Nuala M Byrne, Kendall K Sharpe, and Andrew P Hills. "Validation of a three-frequency bioimpedance spectroscopic method for body composition analysis". In: *Nutrition* 23.9 (2007), pp. 657–664.

[87] JAD Simpson, DN Lobo, JA Anderson, IA Macdonald, AC Perkins, KR Neal, SP Allison, and BJ Rowlands. "Body water compartment measurements: a comparison of bioelectrical impedance analysis with tritium and sodium bromide dilution techniques". In: *Clinical Nutrition* 20.4 (2001), pp. 339–343.

[88] Tao Dai and Andy Adler. "In vivo blood characterization from bioimpedance spectroscopy of blood pooling". In: *IEEE Transactions on Instrumentation and Measurement* 58.11 (2009), pp. 3831–3838.

[89] Sabrina Grassini, Simone Corbellini, Emma Angelini, Franco Ferraris, and Marco Parvis. "Low-cost impedance spectroscopy system based on a logarithmic amplifier". In: *IEEE Transactions on Instrumentation and Measurement* 64.5 (2014), pp. 1110–1117.

[90] Leila Es Sebar, Leonardo Iannucci, Emma Angelini, Sabrina Grassini, and Marco Parvis. "Electrochemical impedance spectroscopy system based on a teensy board". In: *IEEE Transactions on Instrumentation and Measurement* 70 (2020), pp. 1–9.

[91] Hamed Osouli Tabrizi, Razieh Salahandish, Pezhman Jalali, Mahmood Khalghollah, Fatemeh Haghayegh, Amir Sanati-Nezhad, and Ebrahim Ghafar-Zadeh. "A low-cost handheld reconfigurable impedimetric readout system for diagnostics of viral infections". In: *IEEE Transactions on Instrumentation and Measurement* 72 (2023), pp. 1–8.

[92] Zhupeng Jiang, Jiafeng Yao, Li Wang, Hongtao Wu, Jingshi Huang, Tong Zhao, and Masahiro Takei. "Development of a portable electrochemical impedance spectroscopy system for bio-detection". In: *IEEE Sensors Journal* 19.15 (2019), pp. 5979–5987.

[93] Xuanjie Ye, Tianxiang Jiang, Yuhao Ma, Daniel To, Shuren Wang, and Jie Chen. "A portable, low-cost and high-throughput electrochemical impedance spectroscopy device for point-of-care biomarker detection". In: *Biosensors and Bioelectronics: X* 13 (2023), p. 100301.

[94] Alessio Carullo, Franco Ferraris, Marco Parvis, Alberto Vallan, Emma Angelini, and Paolo Spinelli. "Low-cost electrochemical impedance spectroscopy system for corrosion monitoring of metallic antiquities and works of art". In: *IEEE Transactions on Instrumentation and Measurement* 49.2 (2002), pp. 371–375.

[95] Nan Li, Hui Xu, Wei Wang, Zhou Zhou, Guofeng Qiao, and David DU Li. "A high-speed bioelectrical impedance spectroscopy system based on the digital auto-balancing bridge method". In: *Measurement Science and Technology* 24.6 (2013), p. 065701.

[96] A Ruiz-Vargas, JW Arkwright, and Antoni Ivorra. "A portable bioimpedance measurement system based on Red Pitaya for monitoring and detecting abnormalities in the gastrointestinal tract". In: *2016 IEEE EMBS Conference on Biomedical Engineering and Sciences (IECBES)*. IEEE. 2016, pp. 150–154.

[97] Stanley Finger and Marco Piccolino. *The shocking history of electric fishes: from ancient epochs to the birth of modern neurophysiology*. Oxford University Press, 2011.

[98] Marco Piccolino. "Luigi Galvani's path to animal electricity". In: *Comptes Rendus. Biologies* 329.5-6 (2006), pp. 303–318.

[99] Barbara M Doucet, Amy Lam, and Lisa Griffin. "Neuromuscular electrical stimulation for skeletal muscle function". In: *The Yale journal of biology and medicine* 85.2 (2012), p. 201.

[100] Alberto Botter and Roberto Merletti. "EMG of electrically stimulated muscles". In: *Surface Electromyography: Physiology, Engineering, and Applications* (2016), pp. 311–332.

[101] Brendan B Murphy, Brittany H Scheid, Quincy Hendricks, Nicholas V Apollo, Brian Litt, and Flavia Vitale. "Time evolution of the skin–electrode interface impedance under different skin treatments". In: *Sensors* 21.15 (2021), p. 5210.

[102] Thierry Keller and Andreas Kuhn. "Electrodes for transcutaneous (surface) electrical stimulation". In: *Journal of automatic control* 18.2 (2008), pp. 35–45.

[103] Stuart F Cogan. "Neural stimulation and recording electrodes". In: *Annu. Rev. Biomed. Eng.* 10.1 (2008), pp. 275–309.

[104] Douglas B McCreery, William F Agnew, Ted GH Yuen, and Leo Bullara. "Charge density and charge per phase as cofactors in neural injury induced by electrical stimulation". In: *IEEE transactions on Biomedical Engineering* 37.10 (2002), pp. 996–1001.

[105] Clara Günter, Jean Delbeke, and Max Ortiz-Catalan. "Safety of long-term electrical peripheral nerve stimulation: review of the state of the art". In: *Journal of neuroengineering and rehabilitation* 16.1 (2019), p. 13.

[106] Daniel R Merrill, Marom Bikson, and John GR Jefferys. "Electrical stimulation of excitable tissue: design of efficacious and safe protocols". In: *Journal of neuroscience methods* 141.2 (2005), pp. 171–198.

[107] Anke Sieg and Valentine Wascotte. "Diagnostic and therapeutic applications of iontophoresis". In: *Journal of drug targeting* 17.9 (2009), pp. 690–700.

[108] Michael J Pikal. "The role of electroosmotic flow in transdermal iontophoresis". In: *Advanced drug delivery reviews* 46.1-3 (2001), pp. 281–305.

[109] H. Zheng, Z. Pu, H. Wu, C. Li, X. Zhang, and D. Li. "Reverse iontophoresis with the development of flexible electronics: A review". In: *Biosensors and Bioelectronics* 223 (2023), p. 115036.

[110] Benoît Leboulanger, Richard H Guy, and M Begoña Delgado-Charro. "Reverse iontophoresis for non-invasive transdermal monitoring". In: *Physiological measurement* 25.3 (2004), R35.

[111] S. Teepoo, P. Chumsaeng, S. Jongjinakool, K. Chantu, and W. Nolykad. "A new simple and rapid colorimetric screening test for semi-qualitative analysis of vitamin C in fruit juices based on Prussian blue". In: *Journal of Applied Sciences* 12.6 (2012), pp. 568–574.

[112] K.E. Cheng, Y. Lu, K.Y. Tong, A.B. Rad, D.H. Chow, and D. Sutanto. "Development of a circuit for functional electrical stimulation". In: *IEEE Transactions on Neural Systems and Rehabilitation Engineering* 12.1 (2004), pp. 43–47.

[113] J.B. Velloso and M.N. Souza. "A programmable system of functional electrical stimulation (FES)". In: *Proceedings of the 29th Annual International Conference of the IEEE Engineering in Medicine and Biology Society*. Lyon, France: IEEE, 2007, pp. 2234–2237.

[114] H. Qu, T. Wang, M. Hao, P. Shi, W. Zhang, G. Wang, and N. Lan. "Development of a network FES system for stroke rehabilitation". In: *Proceedings of the 2011 Annual International Conference of the IEEE Engineering in Medicine and Biology Society*. Boston, MA, USA: IEEE, 2011, pp. 3119–3122.

[115] A. Masdar, B.S.K.K. Ibrahim, and M.M.A. Jamil. "Development of wireless-based low-cost current controlled stimulator for patients with spinal cord injuries". In: *Proceedings of the 2012 IEEE-EMBS Conference on Biomedical Engineering and Sciences*. Langkawi, Malaysia: IEEE, 2012, pp. 493–498.

[116] F. Brunetti, A. Garay, J.C. Moreno, and J.L. Pons. "Enhancing functional electrical stimulation for emerging rehabilitation robotics in the framework of HYPER project". In: *Proceedings of the 2011 IEEE International Conference on Rehabilitation Robotics*. Zurich, Switzerland: IEEE, 2011, pp. 1–6.

[117] D. Karpul, G.K. Cohen, G.D. Gargiulo, A. van Schaik, S. McIntyre, and P.P. Breen. "Low-power transcutaneous current stimulator for wearable applications". In: *Biomedical Engineering Online* 16.1 (2017), pp. 1–13.

[118] Jessica L Harding, Meda E Pavkov, Dianna J Magliano, Jonathan E Shaw, and Edward W Gregg. "Global trends in diabetes complications: a review of current evidence". In: *Diabetologia* 62 (2019), pp. 3–16.

[119] Unai Galicia-Garcia, Asier Benito-Vicente, Shifa Jebari, Asier Larrea-Sebal, Haziq Siddiqi, Kepa B Uribe, Helena Ostolaza, and César Martín. "Pathophysiology of type 2 diabetes mellitus". In: *International journal of molecular sciences* 21.17 (2020), p. 6275.

[120] Katherine Ogurtsova, JD da Rocha Fernandes, Y Huang, Ute Linnenkamp, L Guariguata, Nam H Cho, David Cavan, JE Shaw, and LE Makaroff. "IDF Diabetes Atlas: Global estimates for the prevalence of diabetes for 2015 and 2040". In: *Diabetes research and clinical practice* 128 (2017), pp. 40–50.

[121] Joshua Scallan and Virginia Huxley. "Capillary fluid exchange: regulation, functions, and pathology". In: (2009).

[122] Vittorio Sansalone, Joanna Kaiser, Salah Naili, and Thibault Lemaire. "Interstitial fluid flow within bone canaliculi and electro-chemo-mechanical features of the canalicular milieu: a multi-parametric sensitivity analysis". In: *Biomechanics and modeling in mechanobiology* 12 (2013), pp. 533–553.

[123] Eda Cengiz and William V Tamborlane. "A tale of two compartments: interstitial versus blood glucose monitoring". In: *Diabetes technology & therapeutics* 11.S1 (2009), S–11.

[124] Louise Dye, Michael Mansfield, Nicola Lasikiewicz, Lena Mahawish, Rainer Schnell, Duncan Talbot, Hitesh Chauhan, Fiona Croden, and Clare Lawton. "Correspondence of continuous interstitial glucose measurement against arterialised and capillary glucose following an oral glucose tolerance test in healthy volunteers". In: *British journal of nutrition* 103.1 (2010), pp. 134–140.

[125] Marion Fokkert, Peter Van Dijk, Mireille Edens, Eglantine Barents, Jeanine Mollema, Robbert Slingerland, Reinold Gans, and Henk Bilo. "Improved well-being and decreased disease burden after 1-year use of flash glucose monitoring (FLARE-NL4)". In: *BMJ Open Diabetes Research and Care* 7.1 (2019), e000809.

[126] Sara Charleer, Christophe De Block, Liesbeth Van Huffel, Ben Broos, Steffen Fieuws, Frank Nobels, Chantal Mathieu, and Pieter Gillard. "Quality of life and glucose control after 1 year of nationwide reimbursement of intermittently scanned continuous glucose monitoring in adults living with type 1 diabetes (FUTURE): a prospective observational real-world cohort study". In: *Diabetes Care* 43.2 (2020), pp. 389–397.

[127] Jan Šoupal, Lenka Petruželková, George Grunberger, Aneta Hásková, Milan Flekač, Martin Matoulek, Ondřej Mikeš, Tomáš Pelcl, Jan Škrha Jr, Eva Horová, et al. "Glycemic outcomes in adults with T1D are impacted more by continuous glucose monitoring than by insulin delivery method: 3 years of follow-up from the COMISAIR study". In: *Diabetes Care* 43.1 (2020), pp. 37–43.

[128] Jan Šoupal, Lenka Petruželková, Milan Flekač, Tomáš Pelcl, Martin Matoulek, Martina Daňková, Jan Škrha, Štěpán Svačina, and Martin Prázný. "Comparison of different treatment modalities for type 1 diabetes, including sensor-augmented insulin regimens, in 52 weeks of follow-up: a COMISAIR study". In: *Diabetes technology & therapeutics* 18.9 (2016), pp. 532–538.

[129] Girish Rao, Peretz Glikfeld, and Richard H Guy. "Reverse iontophoresis: development of a noninvasive approach for glucose monitoring". In: *Pharmaceutical Research* 10 (1993), pp. 1751–1755.

[130] Zhihua Pu, Xingguo Zhang, Haixia Yu, Jiaan Tu, Hailong Chen, Yuncong Liu, Xiao Su, Ridong Wang, Lei Zhang, and Dachao Li. "A thermal activated and differential self-calibrated flexible epidermal biomicrofluidic device for wearable accurate blood glucose monitoring". In: *Science Advances* 7.5 (2021), eabd0199.

[131] CTS Ching and P Connolly. "Reverse iontophoresis: A non-invasive technique for measuring blood lactate level". In: *Sensors and Actuators B: Chemical* 129.1 (2008), pp. 352–358.

[132] CTS Ching, Y Buisson, and P Connolly. "The effect of pulsed bipolar dc on the simultaneous extraction of glucose and lactate by reverse iontophoresis". In: *Sensors and Actuators B: Chemical* 129.2 (2008), pp. 504–509.

[133] Tuuli A Hakala, Laura K Zschaechner, Risto T Vänskä, Teemu A Nurminen, Melissa Wardale, Jonathan Morina, Zhanna A Boeva, Reeta Saukkonen, Juha-Matti Alakoskela, Kim Pettersson-Fernholm, et al. "Pilot study in human healthy

volunteers on the use of magnetohydrodynamics in needle-free continuous glucose monitoring". In: *Scientific Reports* 12.1 (2022), p. 18318.

[134] Jessica Hanna, Moussa Bteich, Youssef Tawk, Ali H Ramadan, Batoul Dia, Fatima A Asadallah, Aline Eid, Rouwaida Kanj, Joseph Costantine, and Assaad A Eid. "Noninvasive, wearable, and tunable electromagnetic multisensing system for continuous glucose monitoring, mimicking vasculature anatomy". In: *Science Advances* 6.24 (2020), eaba5320.

[135] Samir Mitragotri, Matthew Coleman, Joseph Kost, and Robert Langer. "Transdermal extraction of analytes using low-frequency ultrasound". In: *Pharmaceutical Research* 17 (2000), pp. 466–470.

[136] Samir Mitragotri, Matthew Coleman, Joseph Kost, and Robert Langer. "Analysis of ultrasonically extracted interstitial fluid as a predictor of blood glucose levels". In: *Journal of Applied Physiology* (2000).

[137] Edgar Diessel, Peter Kamphaus, Klaus Grothe, Roland Kurte, Uwe Damm, and H Michael Heise. "Nanoliter serum sample analysis by mid-infrared spectroscopy for minimally invasive blood-glucose monitoring". In: *Applied spectroscopy* 59.4 (2005), pp. 442–451.

[138] Yi-Cheng Hsieh and Jeffrey D Zahn. "Glucose recovery in a microfluidic microdialysis biochip". In: *Sensors and Actuators B: Chemical* 107.2 (2005), pp. 649–656.

[139] Cosimo Scuffi, Fausto Lucarelli, and Francesco Valgimigli. "Minimizing the impact of time lag variability on accuracy evaluation of continuous glucose monitoring systems". In: *Journal of Diabetes Science and Technology* 6.6 (2012), pp. 1383–1391.

[140] Raymond J Davey, Chee Low, Timothy W Jones, and Paul A Fournier. "Contribution of an intrinsic lag of continuous glucose monitoring systems to differences in measured and actual glucose concentrations changing at variable rates in vitro". In: *Journal of Diabetes Science and Technology* 4.6 (2010), pp. 1393–1399.

[141] Günther Schmelzeisen-Redeker, Michael Schoemaker, Harald Kirchsteiger, Guido Freckmann, Lutz Heinemann, and Luigi Del Re. "Time delay of CGM sensors: relevance, causes, and countermeasures". In: *Journal of diabetes science and technology* 9.5 (2015), pp. 1006–1015.

[142] D Barry Keenan, John J Mastrototaro, Gayane Voskanyan, and Garry M Steil. "Delays in minimally invasive continuous glucose monitoring devices: a review of current technology". In: *Journal of diabetes science and technology* 3.5 (2009), pp. 1207–1214.

[143] Kerstin Rebrin, Norman F Sheppard Jr, and Garry M Steil. *Use of subcutaneous interstitial fluid glucose to estimate blood glucose: revisiting delay and sensor offset.* 2010.

[144] Philip J Stout, Joel R Racchini, and Michael E Hilgers. "A novel approach to mitigating the physiological lag between blood and interstitial fluid glucose measurements". In: *Diabetes technology & therapeutics* 6.5 (2004), pp. 635–644.

[145] Edgar JG Peters, David G Armstrong, Robert P Wunderlich, Jan Bosma, Susan Stacpoole-Shea, and Lawrence A Lavery. "The benefit of electrical stimulation to enhance perfusion in persons with diabetes mellitus". In: *The Journal of foot and ankle surgery* 37.5 (1998), pp. 396–400.

[146] Heidi J Indergand and Barbara J Morgan. "Effects of high-frequency transcutaneous electrical nerve stimulation on limb blood flow in healthy humans". In: *Physical therapy* 74.4 (1994), pp. 361–367.

[147] JQ Chen, N Yonehara, YXUW Imai, WJ Xu, and R Inoki. "Effects of morphine on cutaneous blood flow and substance P release evoked by electric stimulation of rat sciatic nerve". In: *Zhongguo yao li xue bao= Acta Pharmacologica Sinica* 12.4 (1991), pp. 355–357.

[148] James E Tracy, Dean P Currier, and A Joseph Threlkeld. "Comparison of selected pulse frequencies from two different electrical stimulators on blood flow in healthy subjects". In: *Physical therapy* 68.10 (1988), pp. 1526–1532.

[149] Nitin Dixit, Vikas Bali, Sanjula Baboota, Alka Ahuja, and Javed Ali. "Iontophoresis-an approach for controlled drug delivery: a review". In: *Current drug delivery* 4.1 (2007), pp. 1–10.

[150] Christopher M Proctor, Andrea Slézia, Attila Kaszas, Antoine Ghestem, Isabel Del Agua, Anna-Maria Pappa, Christophe Bernard, Adam Williamson, and George G Malliaras. "Electrophoretic drug delivery for seizure control". In: *Science advances* 4.8 (2018), eaau1291.

[151] Ilke Uguz, Christopher M Proctor, Vincenzo F Curto, Anna-Maria Pappa, Mary J Donahue, Magali Ferro, Róisín M Owens, Dion Khodagholy, Sahika Inal, and George G Malliaras. "A microfluidic ion pump for in vivo drug delivery". In: *Advanced Materials* 29.27 (2017), p. 1701217.

[152] Bin Yang, Xueen Fang, and Jilie Kong. "Engineered microneedles for interstitial fluid cell-free DNA capture and sensing using iontophoretic dual-extraction wearable patch". In: *Advanced Functional Materials* 30.24 (2020), p. 2000591.

[153] Daigo Terutsuki, Sho Miyazawa, Junya Takagi, Akihiro Yamada, Yunhao Sun, Hiroya Abe, Gaobo Wang, and Matsuhiko Nishizawa. "Spatiotemporally Controllable Chemical Delivery Utilizing Electroosmotic Flow Generated in Combination of Anionic and Cationic Hydrogels". In: *Advanced Functional Materials* 34.2 (2024), p. 2304946.

[154] Andrew Jajack, Michael Brothers, Gerald Kasting, and Jason Heikenfeld. "Enhancing glucose flux into sweat by increasing paracellular permeability of the sweat gland". In: *PLoS One* 13.7 (2018), e0200009.

[155] Amy M MacDonald, Mary AW Sheppard, and Charles A Lucy. "Enhancement of electroosmotic flow using zwitterionic additives". In: *Electrophoresis* 26.23 (2005), pp. 4421–4428.

[156] Lorraine Wearley and Yie W Chien. "Enhancement of the in vitro skin permeability of azidothymidine (AZT) via iontophoresis and chemical enhancer". In: *Pharmaceutical research* 7 (1990), pp. 34–40.

[157] K Bauerova, D Matušová, and Z Kassai. "Chemical enhancers for transdermal drug transport". In: *European journal of drug metabolism and pharmacokinetics* 26 (2001), pp. 85–94.

[158] Shinya Kusama, Kaito Sato, Yuuya Matsui, Natsumi Kimura, Hiroya Abe, Shotaro Yoshida, and Matsuhiko Nishizawa. "Transdermal electroosmotic flow generated by a porous microneedle array patch". In: *Nature communications* 12.1 (2021), p. 658.

[159] Xiangling Li, Xinshuo Huang, Jingshan Mo, Hao Wang, Qiqi Huang, Cheng Yang, Tao Zhang, Hui-Jiuan Chen, Tian Hang, Fanmao Liu, et al. "A fully integrated closed-loop system based on mesoporous microneedles-iontophoresis for diabetes treatment". In: *Advanced Science* 8.16 (2021), p. 2100827.

[160] Yanxiang Cheng, Xia Gong, Jian Yang, Guizhou Zheng, Ying Zheng, Yanjun Li, Yunsheng Xu, Gang Nie, Xi Xie, Meiwan Chen, et al. "A touch-actuated glucose sensor fully integrated with microneedle array and reverse iontophoresis for diabetes monitoring". In: *Biosensors and Bioelectronics* 203 (2022), p. 114026.

[161] Momina Amir, Maria Atalaia Rosa, Lina Debeer, Nadalan Vercooren, Filippo Franceschini, Ruben Van Den Eeckhoudt, Nadezda Kuznetsova, Michael Kraft, and Irene Taurino. "Cleanroom-Compatible Polymeric Nanostructured Microneedle Patch for Advanced Wearable Applications". In: *Biosensors and Bioelectronics* (2025), p. 117806.

[162] Jeffrey Farnese, Pei Zhao, and Carolyn L Ren. "Effect of surface roughness on bond strength between PCTE membranes and PDMS towards microfluidic applications". In: *International Journal of Adhesion and Adhesives* 106 (2021), p. 102800.

[163] Congo Tak-Shing Ching and Wei-Yi Chih. "Design and evaluation of an affordable and programmable mobile device, capable of delivering constant current and high voltage electric pulses of different waveforms for biomedical and clinical applications". In: *Sensors and Actuators B: Chemical* 194 (2014), pp. 361–370.

[164] Congo Tak-Shing Ching, Tai-Ping Sun, Wei-Ti Huang, Su-Hua Huang, Chin-Sung Hsiao, and Kang-Ming Chang. "A circuit design of a low-cost, portable and programmable electroporation device for biomedical applications". In: *Sensors and Actuators B: Chemical* 166 (2012), pp. 292–300.

[165] CTS Ching, I Camilleri, and P Connolly. "A low-cost, programmable device for versatile current delivery in iontophoresis applications". In: *Sensors and Actuators B: Chemical* 106.2 (2005), pp. 534–540.

[166] Alessandro Zompanti, Davide Ciarrocchi, Simone Grasso, Riccardo Olivieri, Giuseppe Ferri, Marco Santonico, and Giorgio Pennazza. "Improving Electrical Stimulation Effectiveness and Versatility for Non-Invasive Transdermal Monitoring Applications via an Innovative Mixed-Signal Electronic Interface". In: *Sensors* 24.23 (2024), p. 7626.

[167] Michinari Kono, Takumi Takahashi, Hiromi Nakamura, Takashi Miyaki, and Jun Rekimoto. "Design guideline for developing safe systems that apply electricity to the human body". In: *ACM Transactions on Computer-Human Interaction (TOCHI)* 25.3 (2018), pp. 1–36.

[168] Bor-han Chueh, Dongeun Huh, Christina R Kyrtsos, Timothée Houssin, Nobuyuki Futai, and Shuichi Takayama. "Leakage-free bonding of porous membranes into layered microfluidic array systems". In: *Analytical chemistry* 79.9 (2007), pp. 3504–3508.

[169] Teresa Bagniefski and Ronald R Burnette. "A comparison of pulsed and continuous current iontophoresis". In: *Journal of controlled release* 11.1-3 (1990), pp. 113–122.

[170] Ming Wei, Yanxia Qiao, Haitao Zhao, Jie Liang, Tingshuai Li, Yonglan Luo, Siyu Lu, Xifeng Shi, Wenbo Lu, and Xuping Sun. "Electrochemical non-enzymatic glucose sensors: recent progress and perspectives". In: *Chemical communications* 56.93 (2020), pp. 14553–14569.

[171] Dae-Woong Hwang, Saram Lee, Minjee Seo, and Taek Dong Chung. "Recent advances in electrochemical non-enzymatic glucose sensors–a review". In: *Analytica chimica acta* 1033 (2018), pp. 1–34.

[172] Misagh Abbasnia Tehrani, Seyyed Hamid Ahmadi, Somayeh Alimohammadi, Pezhman Sasanpour, Neda Batvani, Sayed Habib Kazemi, and Mohammad Ali Kiani. "Continuous glucose monitoring using wearable non-enzymatic sensors in a physiological environment". In: *Biosensors and Bioelectronics: X* 18 (2024), p. 100482.

[173] Filippo Franceschini and Irene Taurino. “Nickel-based catalysts for non-enzymatic electrochemical sensing of glucose: A review”. In: *Physics in Medicine* 14 (2022), p. 100054.

[174] Filippo Franceschini, Maria Recaman Payo, Koen Schouteden, Jon Ustarroz, Jean Pierre Locquet, and Irene Taurino. “MBE Grown Vanadium Oxide Thin Films for Enhanced Non-Enzymatic Glucose Sensing”. In: *Advanced Functional Materials* 33.43 (2023), p. 2304037.